UCLA
UCLA Electronic Theses and Dissertations

Title

Miniature RF Gridded Ion Thruster for Air-Breathing and Alternative Propellants

Permalink

https://escholarship.org/uc/item/1133m9fk

Author

Crandall, Patrick

Publication Date

2024

Peer reviewed|Thesis/dissertation

eScholarship.org Powered by the California Digital Library
University of California

UNIVERSITY OF CALIFORNIA

Los Angeles

Miniature RF Gridded Ion Thruster for Air-Breathing and Alternative Propellants

A dissertation submitted in partial satisfaction

of the requirements for the degree

Doctor of Philosophy in Aerospace Engineering

by

Patrick Crandall

2024

© Copyright by
Patrick Crandall
2024

ABSTRACT OF THE DISSERTATION

Miniature RF Gridded Ion Thruster for Air-Breathing and Alternative Propellants

by

Patrick Crandall
Doctor of Philosophy in Aerospace Engineering
University of California, Los Angeles, 2024
Professor Richard E. Wirz, Chair

Recently, many mission designers are considering very low Earth orbit (VLEO) below 450km for individual spacecraft missions and large spacecraft constellations due to several mission benefits including a reduced debris environment, increased performance for Earth observation sensors, and improved link budgets. Operating in VLEO is difficult due to high atmospheric drag, and onboard propulsion is required to compensate for drag and maintain the orbit. High efficiency electric propulsion (EP) has been used for drag compensation in VLEO, but for long duration missions at low altitudes, propellant requirements using conventional EP become prohibitively large. VLEO spacecraft operational lifetime and payload volume can be increased by utilizing air breathing electric propulsion (ABEP). ABEP collects air from the upper atmosphere through an inlet system and uses the collected air as propellant to produce thrust and compensate for drag, reducing or removing stored propellant constraints and enabling long-lifetime VLEO missions.

This dissertation examines the performance of VLEO spacecraft employing ABEP for drag compensation using system models as well as experimental thruster data from an in-house developed RF gridded ion thruster. Thruster performance and material considerations

are presented for propellants relevant to ABEP as well as other alternative propellants.

A system-level analysis of an ABEP spacecraft is presented linking mission performance, defined as the minimum sustained orbital altitude, to inlet and propulsion performance, overall spacecraft geometry, and orbit beta. Optimal geometries for ABEP spacecraft were found, and ABEP thrust-to-power was found to be a major driver of mission performance. Geomagnetic storms can cause rapid increases in drag increasing risk for VLEO spacecraft. An orbit propagator is used to predict the impact of geomagnetic storms on ABEP spacecraft and examine risk mitigation strategies. Preemptive orbit raising and xenon addition to the thruster were identified as effective strategies to increase ABEP spacecraft survivability during a severe geomagnetic storm.

An RF gridded ion thruster was developed to experimentally collect thruster performance data on air propellant as well as for several other alternative propellants. The thruster was designed to be low cost, robust to failure with easily replaceable parts, and representative of currently available RF gridded ion thrusters. Thruster performance operating on xenon, the standard propellant used for electric propulsion, is compared with krypton, argon, pure nitrogen, air, and an $N_2 + 2H_2$ mixture representative of hydrazine propellant. A steep drop in performance is observed between noble gas and nitrogen based propellants which is attributed to low RF coupling efficiency and dissociation of the molecular propellants. Air-xenon mixtures are found to reduce RF power requirements and increase thrust-to-power with relatively low xenon flow rates.

Highly reactive molecular propellants can interact with thruster materials reducing performance and decreasing thruster lifetime. Titanium, molybdenum, and stainless steel compatibility with air and pure nitrogen plasmas was investigated through surface layer analysis. Molybdenum was found to be highly reactive with oxygen in the air plasma while titanium and stainless steel were found to have low reactivity with pure nitrogen plasmas.

This dissertation links ABEP thruster performance to mission performance through system analysis, evaluates mission risks due to geomagnetic storm events, presents experimental

performance data for an RF gridded ion thruster operating on various propellants including air and air-xenon mixtures, and includes material compatibility studies guiding future ABEP and alternative propellant development efforts.

The dissertation of Patrick Crandall is approved.

Raymond M. Spearrin

Thomas John McGuire

Troy A. Carter

Artur R. Davoyan

Richard E. Wirz, Committee Chair

University of California, Los Angeles

2024

"It's demon hours"

-Shehan Parmar

TABLE OF CONTENTS

1 Introduction and Motivation **1**

1.1 Benefits of VLEO Operation 1

1.2 Challenges to VLEO Operation 2

1.3 Air-Breathing Electric Propulsion 3

1.4 Alternative Propellants 6

1.5 Dissertation Overview 7

2 ABEP Mission Analysis and Propulsion Requirements Definition **9**

2.1 Mission Approach 10

2.1.1 VLEO Environment 10

2.1.2 ABEP Thrust Analysis 12

2.1.3 Drag 16

2.1.4 Drag Model 18

2.1.5 Power Model 21

2.1.6 VLEO Orbit Types 25

2.2 Results 26

2.2.1 Power Limited Altitude 26

2.2.2 Thrust to Drag Ratio 28

2.2.3 Parameter Sweep 29

2.2.4 Comparison Between Conventional EP and ABEP 33

2.2.5 Super Low Perigee Orbit Analysis 41

2.2.6 Discussion 41

2.3 Aerodynamic Forces 45
2.4 Mission Study Conclusions 48

3 Geomagnetic Storm Risk to ABEP Missions 49
3.1 Geomagnetic Storm Risk Analysis Approach 52
3.1.1 Spacecraft Parameter Selection 55
3.2 Survivability Results 56
3.2.1 No Action 56
3.2.2 Preemptive orbit raising 59
3.2.3 Xenon Addition 60
3.3 Geomagnetic Storm Risk Conclusions 62

4 RF Gridded Ion Thruster Overview 64
4.1 ICP Discharge Overview 65
4.1.1 Capacitive Coupling 66
4.1.2 Discharge Startup 67
4.2 Antenna Matching 67
4.2.1 Match Network 68
4.2.2 Antenna Design 70
4.2.3 RF Safety 72
4.3 RF Thruster Overview Summary 72

5 PESPL RF Gridded Ion Thruster 73
5.1 Thruster Description 74
5.1.1 Neutralizer 78

5.2 Methods 79
5.3 Results 82
5.3.1 Noble Gasses: Xenon, Krypton, Argon 83
5.3.2 Nitrogen Based Propellants: Molecular Nitrogen, Air, N2 + 2H2 . . . 85
5.3.3 Thruster Performance Comparison 88
5.3.4 Air-Xenon Mixtures 90
5.3.5 Helium and Hydrogen 95
5.4 PESPL Thruster Testing Conclusions 95

6 Thruster Materials Compatibility 97
6.1 Test Setup 98
6.2 Material Characterization Results 100
6.3 Material Characterization Conclusions 104

7 Conclusion 106
7.1 Summary of Conclusions 106
7.2 Future Work 108
7.2.1 ABEP System Analysis 108
7.2.2 RF Thruster Design Methodology 109
7.2.3 Advanced PESPL Thruster Diagnostics 109
7.2.4 PESPL Thruster Improvements 110
7.2.5 Future Material Compatibility Studies 111

Appendix A Global Model 112
A.1 Non-Dissociative 112

A.2 Nitrogen Model Including Dissociation 114
A.2.1 Xenon-Nitrogen Mixtures 116
A.3 Discussion of Global Models 117

Appendix B EDS Data 118

References 122

LIST OF FIGURES

1.1 Debris evolution beginning with a uniform debris density at all altitudes. Debris from higher altitudes precipitates through lower altitude orbits. Lower altitudes become clear of debris on much shorter timescales than higher altitude orbits. . 3

1.2 Lifetime of an unpropelled spacecraft. The blue curve represents the worst case of high solar activity and high ballistic coefficient. The yellow curve represents the best case of low solar activity and low ballistic coefficient. Figure credit from Crisp et al. 2020 [1]. 4

1.3 The ratio of radial acceleration from the Coulomb force and the applied electrostatic force are plotted over a) axial coordinate and b) radial coordinate with color corresponding to species. 5

1.4 Photos of SITAEL's RAM-EP system showing the honeycomb inlet on the left and Hall-effect thruster on the right [2]. 6

2.1 Atmospheric composition over a range of VLEO altitudes. The primary atmospheric constituents at VLEO altitudes are atomic oxygen and diatomic nitrogen. Produced using the NRLMSISE-00 model. 11

2.2 Historical 10.7 cm radio flux showing the 11 year solar cycle. Marked values for solar minimum, average solar conditions, and solar maximum are marked at 62 SFU, 114 SFU, and 200 SFU. Data taken from [3] 12

2.3 Block diagram of an ABEP thruster and inlet system showing mass flow through the system. 12

2.4 Diagram of the reference VLEO bus geometry used in this analysis. Length overall (L), solar array thickness (t_{SA}), and solar array length (s) are defined through ratios to the bus diameter d. 16

2.5 C_D for perpendicular and parallel incidence. 19

2.6 Drag comparison between a 1×3U and a 1×6U CubeSat 21

2.7 Diagram showing the optimal spacecraft attitude which maximizes collected power while keeping the spacecraft oriented for minimum drag. Spacecraft velocity vector is shown in red, solar array normal is shown in blue, orbit normal is shown in purple, and the sun vector is shown in yellow. β is the angle between the sun vector and the orbital plane. 23

2.8 Power collected over two complete $\beta = 30°$, 200 km altitude orbits showing eclipse periods in grey and power reduction due to solar array cosine losses. Power is normalized to the maximum power collected. These results were verified using the Systems Toolkit software [4] 24

2.9 Normalized mean power collected vs β. High β orbits are in constant sunlight and do not have any eclipse periods. Low β orbits experience significantly reduced average power due to long eclipse periods and high cosine losses. This figure is computed for 200 km altitude, but the results do not vary significantly over the VLEO altitude range. 25

2.10 Power limited minimum altitude for various geometries and T/P. T/P has the largest effect on minimum operating altitude. 27

2.11 T/P vs power limited minimum operating altitude for the 6U reference geometry shown in Figure 2.6 $\big(L/d = 6, s = 2\big)$. Current air-breathing gridded ion thrusters achieve $T/P = 10$ mN/kW, inductive plasma thrusters can achieve $T/P = 20$ mN/kW [5, 6], and current air-breathing HET thrusters can achieve $T/P = 30$ mN/kW [7]. Minimum altitude varies by up to 20 km over the solar cycle for this geometry. 28

2.12 T/D vs altitude for a range of L/d. T/D is mostly constant with altitude with some variation due to small changes in $C_{D_{eff}}$ and u_∞ with altitude. 29

2.13 Minimum operating altitude for a range of spacecraft geometries, T/P, and β for an ABEP with $V_b = 1500$ V, $\eta_m = 0.85$, $\eta_{in} = 0.35$, $\gamma = 1$. Cases with $T/D < 1$ are blacked out. High β orbits offer lower altitude operation since they offer more power to the spacecraft. 30

2.14 T/D for a range of spacecraft geometries, T/P, and β for an ABEP spacecraft with $V_b = 1500$ V, $\eta_m = 0.85$, $\eta_{in} = 0.35$, $\gamma = 1$. Cases with $T/D < 1$ are blacked out. 31

2.15 Minimum operating altitude for a range of spacecraft geometries, T/P, and β for an ABEP with $V_b = 500$ V, $\eta_m = 0.85$, $\eta_{in} = 0.35$, and $\gamma = 1$. Cases with $T/D < 1$ are blacked out. High β orbits offer lower altitude operation since they offer more power to the spacecraft. Note for $V_b = 500$ V lower T/D is achievable than for the high V_b case shown in Figure 2.13 and only low drag geometries are feasible. 32

2.16 T/D for a range of spacecraft geometries, T/P, and β for an ABEP spacecraft with $V_b = 500$ V, $\eta_m = 0.85$, $\eta_{in} = 0.35$, and $\gamma = 1$. Cases with $T/D < 1$ are blacked out. 33

2.17 6U CubeSat (10 cm×10 cm×60 cm, $s = 20$ cm). The ABEP variation has the air inlet on the front as shown. The conventional EP case has a flat front. Both configurations have similar drag. 34

2.18 Block diagram of the subsystem layout in the 6U EP spacecraft. As propellant requirements increase, the propellant tank grows, reducing payload volume. . . . 35

2.19 Payload volume of the 6U CubeSat operating in VLEO with a 2000 s I_{sp} EP propulsion system. The kink seen at 2U payload volume is where the propellant tank switches from expanding as a sphere to stretching as a cylinder. 35

2.20 Wet mass of the 6U CubeSat operating in VLEO with a 2000 s I_{sp} EP propulsion system. The CubeSat has a dry mass of 5.3 kg not including propellant tank mass. 36

2.21 Power available to the payload and other subsystems for a 6U CubeSat operating in VLEO with a $T/P = 30$ mN/kW EP propulsion system [8]. 36

2.22 Block diagram of the 6U ABEP CubeSat Layout. This layout is similar to ABEP CubeSat layouts described by Jackson [9]. 37

2.23 Power remaining for spacecraft subsystems and payload. At lower altitudes more power must be supplied to the propulsion system to compensate for drag. At low β average power collected is significantly reduced due to long eclipse periods and high cosine losses. 38

2.24 Power limited minimum perigee altitude for SuLPO orbits. $T/P = 10$ mN/kW, Apogee = 300 km, and s/d = 2 unless otherwise stated in the figure. These figures assume $\beta = 90°$. 42

2.25 Instantaneous power required for SuLPO orbits with perigee altitudes of 140, 150, and 160 km and apogee at 300 km. The spacecraft bus is 50 cm × 50 cm × 250 cm. SuLPO spacecraft will need advanced high-power propulsion and power processing systems. 42

2.26 Power limited minimum operating altitude for an ABEP spacecraft with $T/P =$ 10 mN/kW with varying solar array efficiency. 44

2.27 Power limited minimum operating altitude for an ABEP spacecraft with $T/P =$ 10 mN/kW with varying accommodation coefficients. An accommodation coefficient of 0 leads to $C_{D_{\parallel}} = 0$ and no skin friction drag. The remaining drag is due to frontal area drag. 45

2.28 Diagram of the reference VLEO bus geometry used for aerodynamic force analysis. Length overall (L), solar array thickness (t_{SA}), and solar array length (s) are defined through ratios to the bus diameter d. 46

2.29 Coefficients of lift, drag, and lift to drag ratio for the spacecraft shown in figure 2.28 as a function of yaw angle for $L/d = 6, s = 2, \sigma = 1$. 47

2.30 Lift to drag ratio for the spacecraft shown in figure 2.28 as a function of yaw angle for varying accommodation coefficients for $L/d = 6, s = 2$. Note $\sigma = 1$ is entirely diffuse reflection and $\sigma = 0$ is entirely specular reflection. 47

3.1 Diagram of the reference VLEO bus geometry used in this analysis [10]. Length overall (L), solar array thickness (t_{SA}), and solar array length (s) are defined through ratios to the bus diameter d. 53

3.2 DST index for the reference storm. The geomagnetic storm begins when DST sharply drops negative. Data from [11]. 54

3.3 Propagated orbits for $\eta_{in} = 0.4$ and $C_b = 90, 136$, and 180 kg/m^2. Higher C_b spacecraft can survive the storm without advanced risk mitigation. 56

3.4 Propagated orbits for $C_b = 136$ kg/m^2 and $\eta_{in} = 0.35, 0.40$, and 0.45 corresponding to initial $T/D = 1.09, 1.25$, and 1.40 respectively. Higher T/D spacecraft can survive the storm without advanced risk mitigation. 57

3.5 Net impulse for four spacecraft parameter sets. During the storm an impulse deficit is created due to increased drag which is then made up for during low drag periods. 58

3.6 C_d for $L/d = 5$ and $s/d = 1$ during the reference storm. 59

3.7 Propagated orbits for $\eta_{in} = 0.45, C_d = 4.8, C_b = 90$ kg/m^2. $t = 0$ is set to be when the IMF B_z crosses zero at 20:00:00 on November 7th 2004. 60

3.8 Propagated orbits for $\eta_{in} = 0.35, C_d = 4.8, C_b = 90$ kg/m^2. $t = 0$ is set to be when the IMF B_z crosses zero at 20:00:00 on November 7th 2004. 62

4.1 Diagram of a cylindrical ICP discharge. AC current flows through four turn antenna shown in the diagram which acts as the primary winding of a transformer. Current is induced in the plasma near the antenna forming a single turn transformer secondary. The ICP discharge is represented as a transformer in a circuit diagram [12]. 65

4.2 Electrical diagram of an L match network [13]. In some match networks the order of the shunt and series capacitors are swapped. 69

4.3 Block diagram and circuit diagram of an RF gridded ion thruster showing coupling to the plasma and loss mechanisms which can have capacitive and inductive components [14, 15]. 71

5.1 CAD model of the thruster showing major components and photo of the thruster in the vacuum chamber showing the match network box and neutralizer cathode. 75

5.2 Photo of the thruster with the Faraday shield removed. 75

5.3 Block Diagram of the thruster showing connections with all power supplies. . . . 77

5.4 Photo of the antenna and fixed capacitor match network with the cover removed. RF power is delivered via a 50 Ohm SMA connector. 78

5.5 Cutaway CAD model of the shielded filament cathode showing major components [16]. 79

5.6 A photo of the full vacuum chamber setup with the power supply rack, and a closeup photo of the gas mixture flow manifold set up for noble gasses. 80

5.7 Composite image of the PESPL RF gridded ion thruster running on noble gas propellants. From top down, the propellants are: xenon, krypton, and argon. . . 83

5.8 Thruster performance running on xenon propellant. 84

5.9 Thruster performance running on krypton propellant. 84

5.10 Thruster performance running on argon propellant. 85

5.11 Composite image of the PESPL RF gridded ion thruster running on nitrogen based propellants. From top down, the propellants are: N_2, air (78% N2 + 21% O2), and N_2 + $2H_2$. 86

5.12 Thruster performance running on molecular nitrogen (N_2) propellant. 87

5.13 Thruster performance running on air (78% N2 + 21% O2) propellant. 87

5.14 Thruster performance running on N2 + 2H2 propellant. 88

5.15 Thruster performance running on an air-xe mixture. Air flow rate is a constant 1.75 sccm. 90

5.16 Thruster performance running on an air-xe mixture. Air flow rate is a constant 1.00 sccm. 91

5.17 T/P for the 1.75 sccm air flow case and the 1.00 sccm air flow case. 91

5.18 Thruster specific impulse for air-xenon mixtures. 92

5.19 System specific impulse for air-xenon mixtures. 93

5.20 Extracted beam composition at 80 mA computed using the global model. 93

5.21 Plasma composition inside the discharge chamber at 80 mA computed using the global model. 94

5.22 Electron temperature in the discharge computed using the global model. 94

6.1 Design model of the thruster head. Note the HV anode used in the materials studies [17]. The grids are made of molybdenum. 99

6.2 Anode samples after plasma exposure. The blue color seen on the air exposed samples is likely from molybdenum oxide. The outer edge was not exposed to plasma. 101

6.3 Detail of the nitrogen exposed titanium sample showing the faint surface layer. This layer is likely titanium nitride (TiN). 102

6.4 Screen and accel grids after all runs. The accel grid shows a blue-white coating which may be molybendnum oxide. This coating is not present on the screen grid. 104

B.1 SEM images of the anode sample edge showing the interface between the exposed and unexposed portions of the sample. Labeled spots are where EDS data was taken. 119

B.2 EDS spectra for all surveyed points on the titanium anode. 120

B.3 EDS spectra for all surveyed points for the stainless steel anode. 121

LIST OF TABLES

2.1 Percent drag contribution of each spacecraft surface for a $L/d = 6$ spacecraft. As altitude increases, skin friction drag becomes a larger percentage of the total drag due to an increase in C_D at higher altitudes for parallel incidence surfaces. 22

2.2 Conventional EP (240 km, 3 year mission life) and ABEP Allocated Mass Budgets 39

2.3 Conventional EP (240km, 3 year mission life) and ABEP Allocated Volume Budgets 40

3.1 Performance of the RIT-10 gridded ion thruster operating on an air mixture with added xenon. Data extracted from [6]. RIT-10 I_{sp} operating on 100% xenon extracted from [18]. 61

5.1 Thruster performance at 70 mA beam current. $V_b = 1000$ V. Total power usage for 70 mA beam current can be computed as $P_{RF} + 70$ W. Thruster performance is only computed for the thruster head and neglects cathode and power supply losses. Neutral ingestion is accounted for via a Clausing factor. 89

6.1 Table showing all test combinations for the study. 99

6.2 Atomic percent composition of each sample from XPS analysis. 102

ACKNOWLEDGMENTS

I would first like to thank my advisor, Prof. Richard Wirz, for inviting me into the PESPL family, guiding me throughout the PhD journey, and encouraging me to explore difficult challenges and push myself. Your mentorship over the years has shaped me into a creative and successful researcher. I would also like to thank my graduating committee: Profs. Artur Davoyan, Troy Carter, Mitchell Spearrin, and Dr. Tom McGuire. I appreciate you all taking the time to participate on my committee and keeping up with my research.

Thank you to Dr. Slava Spektor and Dr. Matt Feldman for letting me join the Viridian team for a summer and for your continued guidance and support afterwards. Looking forward to seeing big things from Viridian in the future. I also would like to thank Dr. Colin Adams for inviting me as an undergraduate to his research group at VT and introducing me to plasmas and EP.

I would also like to thank the current and previous members of the PESPL for their advice, camaraderie, and bad jokes. In particular, I would like to thank Dr. Stephen Samples for answering all of my first-year questions. I forgive you for your PCB errors. Also, thank you to Dr. Adam Collins for his help finding tools that are right in front of my face and for always having a solution to any research problem. Stephen Samples, Peter Wright, Nolan Uchizono, Adam Collins, Nicolas Rongione, Ani Thuppul, Shehan Parmar, Angelica Ottiaviano, Gary Wan, Henry Huh, McKenna Davis Breddan, Mary Konopliv, Graeme Sabiston, Rich Obenchain, and Blake Haist; you are some of the most intelligent, hardworking, and friendly people I have worked with. I am truly amongst great company. Thank you to the PESPL extended universe; Phil Travis, Tom Look, Dan Eckhardt, Jess Gonzalez, for your friendship and support throughout my PhD. I would like to thank Charli Espinoza for being there for the end of my PhD and for coaching Team Josh to a 5 game win streak.

I would also like to thank my family who have been my biggest supporters through the

entire journey. I would not have been able to achieve what I have without your support.

VITA

2020 - 2024	Graduate Research Student, Plasma, Energy & Space Propulsion Laboratory, UCLA
2022	M.S. (Aerospace Engineering), UCLA
2022	R&D Intern, Viridian Space Corporation
2020	B.S. (Aerospace Engineering), Virginia Tech
2020	B.A. (Physics), Virginia Tech
2019	Engineering Intern, Ibeos
2018 - 2020	Undergraduate Research Assistant, Virginia Tech Center for Space Science and Engineering (Space@VT)

PUBLICATIONS

Air-Breathing and Alternative Propellant Performance for a 3 cm RF Gridded Ion Thruster P. Crandall, and R. E. Wirz, Journal of Electric Propulsion, in preparation

Air-breathing electric propulsion: mission characterization and design analysis. P. Crandall and R. E. Wirz. Journal of Electric Propulsion 1(1):12, (2022)

Geomagnetic Storm Risks to Air-Breathing Electric Propulsion Missions. P. Crandall, V.

Piccone, T. Asanuma, and R. E. Wirz. 2024 IEEE Aerospace Conference, IEEE XPlore (2024)

RF Gridded Ion Thruster Design for Laboratory Experiments. P. Crandall and R. E. Wirz. AIAA SciTech Conference (2023)

CHAPTER 1

Introduction and Motivation

Spacecraft are essential to the modern world impacting almost every aspect of society from communications to defense to scientific research. This reliance on spacecraft is only expected to increase in the future as new systems such as satellite internet providers, distributed surveillance satellite networks, and other smaller ventures come online. The vast majority of spacecraft reside in orbits near to the Earth known as Low Earth Orbit (LEO). LEO is popular with mission designers due to its close proximity to Earth simplifying launch and improving communications and Earth observation (EO) performance. Being the most popular orbit also means that LEO is crowded with debris, operational and defunct spacecraft, spent rocket bodies, and other hazards which must be avoided. With large satellite constellations planned to come online in the coming years, it is expected that debris and collision avoidance will become far more difficult. Lewis et al. have shown that even with post mission disposal, debris populations and collision events are expected to increase dramatically as more spacecraft operate in LEO [19].

1.1 Benefits of VLEO Operation

Recently, many mission designers are considering Very Low Earth Orbit (VLEO) below 450km for individual spacecraft missions and large spacecraft constellations due to several mission benefits including ease of orbital access, reduced debris environment, reduced radiation environment, improved communication link budgets, and increased resolution for Earth observation sensors [1]. VLEO is low enough that the Earth's atmosphere is significant

causing both debris and unpropelled spacecraft to quickly deorbit due to atmospheric drag.

Debris pose an increased threat to operators in the event of a space conflict where massive amounts of debris are expected to be generated. The 2007 Chinese anti-satellite missile (ASAT) test released over 32,000 debris fragments, and the 2021 Russian ASAT test generated over 1,500 debris fragments demonstrating that a contested space environment will dramatically increase debris threats to DoD orbital assets [20, 21]. Spacecraft of all types are fielded by the Department of Defense (DoD) to fulfill a wide range of defense objectives including secure communications, reconnaissance, weather prediction, missile detection, and global positioning. Adversaries can target civilian or military spacecraft to generate debris fields that can directly destroy other spacecraft, operationally limit DoD spacecraft by requiring excessive collision avoidance maneuvers, or deny certain orbits from use due to debris threats. VLEO orbits naturally clear debris on a much faster timescale than higher altitude orbits as shown in Figure 1.1. Rapid debris removal makes VLEO especially suitable for replacement networks that must come online quickly after loss of a spacecraft in a higher altitude orbit. VLEO spacecraft avoid debris threats which can deny access to higher altitude orbits by operating at low altitude where atmospheric drag quickly clears debris.

1.2 Challenges to VLEO Operation

While VLEO offers enticing benefits to both civilian and defense operators, there are major challenges to operating in VLEO due to the high atmospheric density present at low altitude. Unpropelled spacecraft quickly deorbit from VLEO due to atmospheric drag as shown in figure 1.2. Spacecraft operating in VLEO require onboard propulsion to compensate for drag and maintain the orbit. High efficiency electric propulsion (EP) has been used for drag compensation in VLEO, two notable examples being ESA's GOCE and JAXA's SLATS missions which both employed high I_{sp} gridded ion thrusters [22, 23, 24]. For long duration missions at low altitudes, propellant requirements using conventional EP technology become

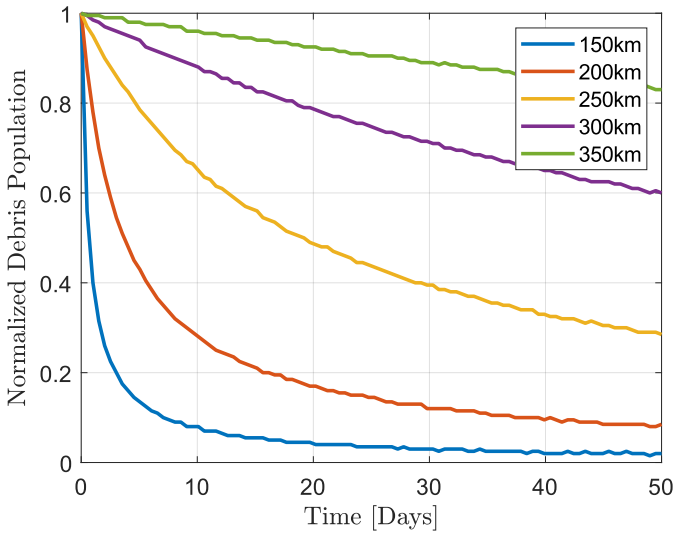

Figure 1.1: Debris evolution beginning with a uniform debris density at all altitudes. Debris from higher altitudes precipitates through lower altitude orbits. Lower altitudes become clear of debris on much shorter timescales than higher altitude orbits.

prohibitively large. The European Space Agency (ESA) has identified 250 km altitude as the limit below which drag compensation using EP with stored onboard propellant becomes unfeasible [25]. Air-breathing electric propulsion (ABEP) aims to remove these propellant constraints by collecting air from the local atmosphere to use as propellant.

1.3 Air-Breathing Electric Propulsion

ABEP operation with a passive inlet can be described in a similar manner to a conventional ramjet shown in Figure 1.3. An air inlet collects and compresses air using the high freestream velocity. In the ramjet case, chemical energy is added to the air heating it, and then the air is accelerated through a nozzle producing thrust. In the ABEP case electrical energy is added to the air ionizing it, and then the ions are accelerated via electrostatic or electromagnetic forces producing thrust. Additional gas can be mixed with the air supplied by the inlet to increase thruster performance [26].

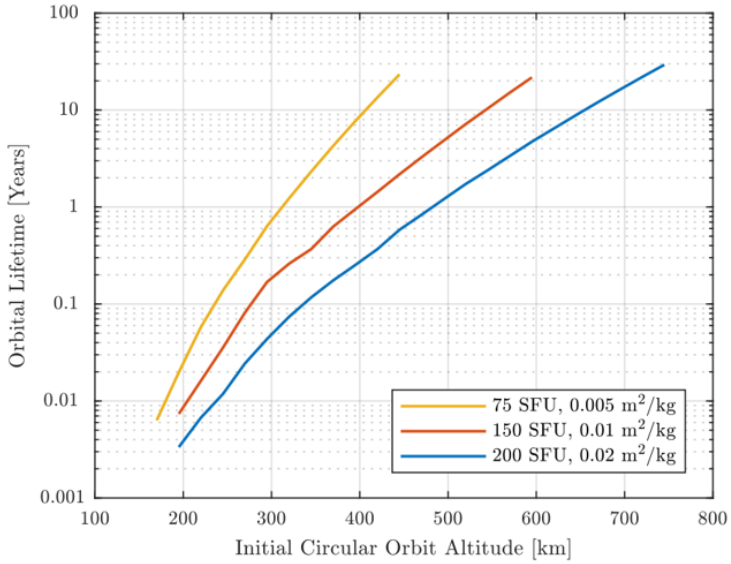

Figure 1.2: Lifetime of an unpropelled spacecraft. The blue curve represents the worst case of high solar activity and high ballistic coefficient. The yellow curve represents the best case of low solar activity and low ballistic coefficient. Figure credit from Crisp et al. 2020 [1].

ABEP spacecraft can be characterized by three main systems: inlet, thruster, and spacecraft bus. The inlet collects and compresses air from the local atmosphere and feeds it to the thruster. As the atmosphere in VLEO is rarefied and not a continuum, efficient collection and compression is challenging. Both passive and active inlets utilizing powered pumps have been presented in the literature. A large body of literature exists regarding passive ABEP inlet design with the most promising designs utilizing a honeycomb structure on the inlet to retain captured air particles shown in Figure 1.4 [2, 27, 28]. The honeycomb structure has high transparency to the high velocity incoming flow, and low transparency to thermalized particles with no bulk velocity. Thus the flow can enter through the honeycomb easily, but it is difficult to leave. Active designs appear less frequently in literature due to their increased complexity, but generally they utilize the same honeycomb inlet as the passive inlet, but with a turbopump backing increasing compression and collection efficiency [26, 29, 28]. An example ABEP inlet-thruster system built by SITAEL for ground testing is shown as figure

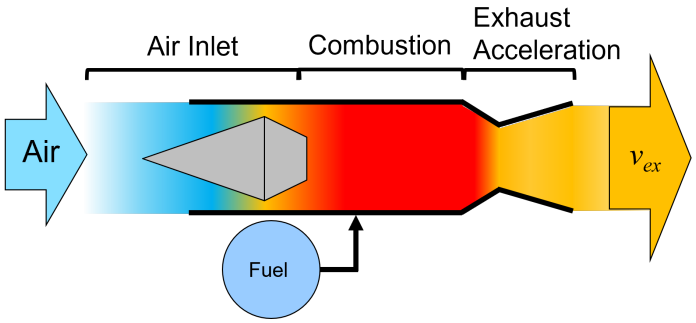

(a) Basic diagram of a ramjet engine.

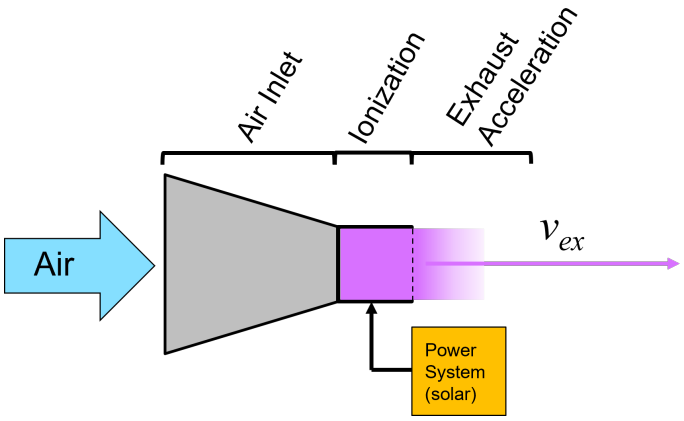

(b) Basic diagram of an ABEP spacecraft.

Figure 1.3: The ratio of radial acceleration from the Coulomb force and the applied electrostatic force are plotted over a) axial coordinate and b) radial coordinate with color corresponding to species.

1.4.

Gridded ion thrusters and Hall-effect thrusters have received the most interest as ABEP thrusters, but MPD thrusters and other more advanced concepts have been proposed as well [30, 31, 7, 2]. ABEP thrusters have far lower efficiency than comparable thrusters operating on conventional propellants due to low mass, molecular nature, and high ionization energy of air compared with common EP propellants such as xenon [7, 6]. Low thruster efficiency results in high power requirements for ABEP spacecraft and thus many mission profiles are

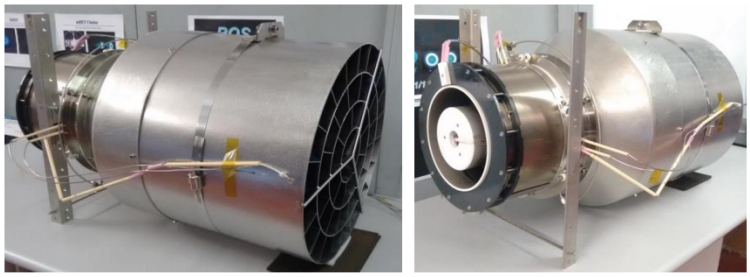

Figure 1.4: Photos of SITAEL's RAM-EP system showing the honeycomb inlet on the left and Hall-effect thruster on the right [2].

power limited [10, 32]. Spacecraft bus design primarily impacts drag and power available to the thruster. Bus designs with large solar arrays collect more power but experience more drag resulting in an optimum wetted area for best mission performance. Literature published by the author and others investigates the impact of bus geometry on ABEP performance [10, 32, 28].

Currently, ABEP has not been demonstrated in space. ABEP research has been focused on conceptual studies, standalone thruster testing, and limited full system testing [28]. Limited experimental data on gridded ion thrusters for ABEP applications exists in the literature with most data coming from a test campaign performed on a RIT-10 RF gridded ion thruster [6, 33, 34]. Additional experimental data for gridded ion thrusters operating on air can inform scaling between thruster sizes and power, and help identify potential pathways to increase thruster performance. Data from the RIT-10 thruster investigates a 10% air-xenon mixture, but additional mixture ratios can provide more information on performance evolution as xenon is added.

1.4 Alternative Propellants

Xenon has been the standard EP propellant for several decades providing high performance, good storability, and excellent material compatibility. Several drawbacks to xenon including

high cost and low global production capacity have motivated a search for xenon alternatives [35]. Krypton and argon are common noble gas alternative propellants, but several molecular propellants have been investigated as well such as water [36]. Multimode propellant architectures operating on a common propellant may benefit from EP thrusters running on hydrazine (N_2H_4) [37].

Operating a thruster on air, a mixture of N_2 and O_2, is challenging due to the high power requirements and reactive nature of the ionized species. Thus a thruster which is able to operate on air is likely to also be able to run on several other propellants of interest to the alternative propellant community as well.

1.5 Dissertation Overview

This research will focus on system analysis of ABEP spacecraft, assessing ABEP mission risk due to geomagnetic storm events, experimental performance measurements from a gridded ion thruster operating on air and other alternative propellants, and the subsequent reactive plasma-material interactions.

Chapter 2 outlines a system analysis of an ABEP spacecraft. Minimum operating altitude is determined for an ABEP spacecraft based on satellite bus geometry, orbit β, and thruster performance. ABEP spacecraft performance is compared with a conventional xenon EP spacecraft, and it is found that for altitudes below 250 km, ABEP offers lower mass than xenon fueled spacecraft. VLEO spacecraft face risk from geomagnetic storms which cause rapid increases in atmospheric drag. Risk from geomagnetic storms on ABEP spacecraft and risk mitigation strategies are investigated in Chapter 3. An orbit propagator is used with the drag model described in Chapter 2 to evaluate the effectiveness of preemptive orbit raising and xenon addition to the propulsion system for mitigating geomagnetic storm risk.

A lab model RF gridded ion thruster is developed to demonstrate operation on air and other alternative propellants. Design principles for RF gridded ion thrusters is outlined

in Chapter 4 with the goal of reducing the barrier of entry for future researchers to build RF sources for propulsion. Experimental thruster performance is presented in Chapter 5. Thruster performance on xenon, krypton, argon, pure nitrogen, air, and a $N_2 + 2H_2$ mixture is presented. Performance with nitrogen based propellants is significantly reduced relative to noble gasses due to propellant dissociation. Air-xenon mixtures are investigated in section 5.3.4 showing significant performance gains from xenon addition. Plasma-material chemical interactions with thruster electrodes are investigated for pure nitrogen and air discharges in Chapter 6. Molybdenum is shown to have poor resistance to oxygen plasma while titanium and stainless steel showed high resistance to pure nitrogen plasma.

Chapter 7 presents a summary of findings as well as pathways for future work extending the findings of thsi dissertation.

CHAPTER 2

ABEP Mission Analysis and Propulsion Requirements Definition

While broad motivations for pursuing ABEP for VLEO missions was provided in previous sections, a robust description of ABEP capabilities is needed to guide further work into ABEP. Of particular interest is a comparison between the mission performance of ABEP vs conventional EP, identifying mission profiles that favor ABEP, and determining ABEP spacecraft and mission design drivers.

Several ABEP thruster and inlet systems have been investigated in the literature, providing a range of feasible performance metrics for these systems [38, 6, 39, 7, 2, 40]. Performance metrics such as inlet and thruster efficiency can be connected to overall spacecraft performance via system analysis. An initial system level analysis was performed by ESA which investigated the altitude range where ABEP would become favorable over conventional EP and found that above 250km altitude, conventional EP provides adequate performance and ABEP is not needed [25]. In 2010, Jackson estimated the operating altitudes of standard CubeSat bus geometries by finding the power limited and thrust limited orbital altitudes [9]. Singh presented a VLEO air collection feasibility study in 2014 providing performance equations for multiple ABEP architectures including stored propellant concepts [41]. In 2019 SITAEL presented a system optimization for their ABEP concept [42]. This work yielded three feasible spacecraft geometries for different operational altitudes. Tisaev et al. presents more general analysis of ABEP performance demonstrating the impact of thrust to power, I_{sp}, inlet efficiency, and other performance metrics on operational altitudes [32]. The authors

also determine a maximum operating altitude by setting a minimum gas density for thruster operation. Additionally, a thruster controller was developed to maintain orbital altitude and avoid divergent altitude envelopes. Many of the previous ABEP studies have been focused on a specific concept and are not generally applicable. While the analysis presented by Tisaev et al. is general to arbitrary spacecraft, it is limited to dawn-dusk Sun-synchronous orbits. The presented mission analysis extends the work done by Tisaev et al. to arbitrary orbits which may not always be in sunlight and elliptical orbits which extend to lower altitudes at perigee. Additionally, this work relates spacecraft geometry scaling relations to operational performance independent of the overall size of the spacecraft thus making this analysis general to CubeSats as well as conventionally sized spacecraft. Spacecraft heating is ignored for this analysis as previous authors have shown that heating only becomes an issue at altitudes lower than those investigated in this paper [43, 32]. Additionally, Earth oblateness perturbations are ignored in this study for simplicity and drag is assumed to be the only orbital perturbation.

2.1 Mission Approach

To maintain a persistent orbit and avoid semi major axis decay, the propulsion system must provide thrust to counteract the non-conservative force of drag on the spacecraft. Therefore, to examine ABEP performance for drag compensation we compare solar-powered ABEP thrust against spacecraft drag as described in the following subsections. For this analysis, we do not explicitly account for second order effects such as J2 perturbations.

2.1.1 VLEO Environment

Drag is the most significant consideration for VLEO orbits due to the significant interactions between the spacecraft and Earth's upper atmosphere. Atmospheric conditions in VLEO can be found using one of the many Earth atmosphere models. Popular atmospheric models are

the 1976 U.S. Standard Atmosphere, Jacchia 1977, NRLMSISE-00, and GOST, all with their own strengths and weaknesses [44, 45, 46, 47, 48]. The NRLMSISE-00 model was chosen for this analysis as it provides accurate information on atmospheric composition, which is useful for ABEP analysis [49].

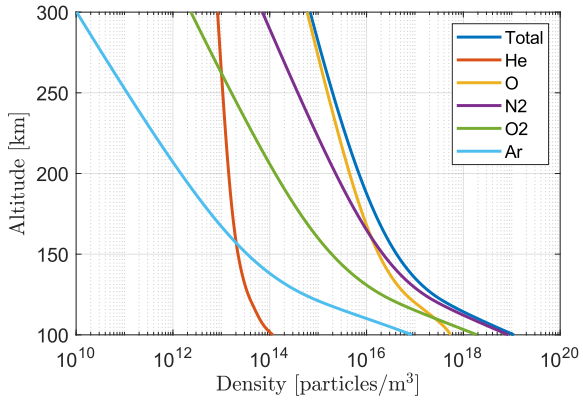

Figure 2.1: Atmospheric composition over a range of VLEO altitudes. The primary atmospheric constituents at VLEO altitudes are atomic oxygen and diatomic nitrogen. Produced using the NRLMSISE-00 model.

Atmospheric density at VLEO altitudes is largely dependent on solar activity, but also varies significantly with latitude, longitude, and geomagnetic activity. Variations in density are milder at VLEO altitudes than at higher altitudes with density changing by roughly a factor of 2 between solar minimum and solar maximum and varying by up to 25% from the mean density in latitude and longitude [50].

With these considerations, this analysis uses an average value for density across all latitude and longitudes and is constrained to median geomagnetic activity (Ap = 8). Where stated, three solar activity conditions will be investigated: solar minimum (10.7 cm flux = 62 SFU), mean solar activity (10.7 cm flux = 114 SFU), and solar maximum (10.7 cm flux = 200 SFU). 10.7 cm solar radio flux has historically reached up to 250 SFU, but 200 SFU offers a realistic mean for sustained solar activity across multiple solar cycles as shown in

Figure 2.2.

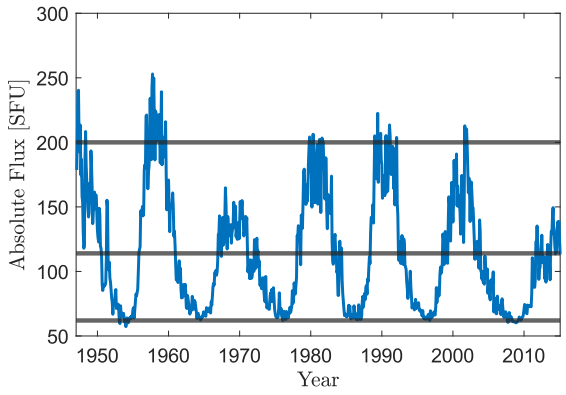

Figure 2.2: Historical 10.7 cm radio flux showing the 11 year solar cycle. Marked values for solar minimum, average solar conditions, and solar maximum are marked at 62 SFU, 114 SFU, and 200 SFU. Data taken from [3]

2.1.2 ABEP Thrust Analysis

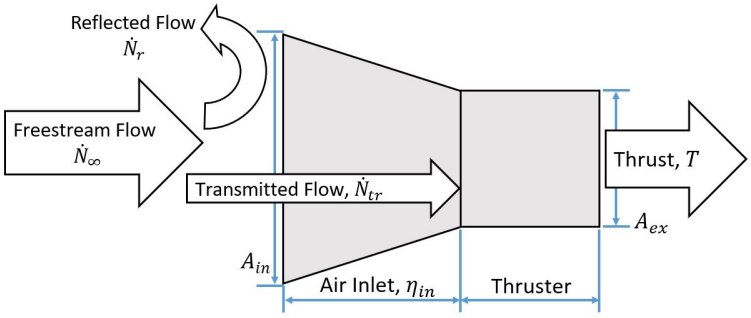

Figure 2.3: Block diagram of an ABEP thruster and inlet system showing mass flow through the system.

ABEP thruster systems consist of an inlet which collects air from the atmosphere and an EP thruster which ionizes and accelerates the propellant collected by the inlet as shown in Figure 2.3. Air is made up of multiple species, so thrust is given as a summation of the

individual thrust contribution from each species:

$$T = \eta_m \gamma \sum_s \dot{m}_s c_s \tag{2.1}$$

where c_s is the exhaust velocity of each species, $\dot{m}_s$ is the exhaust mass flow rate of each species, η_m takes into account neutral particles lost due to diffusion out of the thruster which contribute negligible thrust, and γ is a loss factor which takes into account thrust reduction caused by beam divergence and the presence of doubly charged ions. This mass flow rate can be expressed as the product of particle flow rate, $\dot{N}_s$, and the individual particle mass, M, such that $\dot{m}_s = \dot{N}_s M_s$. Generally, molecular species are not conserved due to dissociation and recombination in the thruster. $\dot{N}_s$ is dependent on thruster geometry and plasma conditions inside the thruster, and accurately computing $\dot{N}_s$ requires a reacting plasma code which is outside the scope of this work. This analysis will assume frozen flow throughout the thruster such that $\dot{N}_{collected_s} = \dot{N}_{exhaust_s}$ The particle flow rate effectively captured by the inlet can be expressed as,

$$\dot{N}_s = \eta_{in} n_{a_s} u_\infty A_{in} \tag{2.2}$$

The inlet efficiency η_{in} is defined as the ratio of incident mass flux that is transmitted through the inlet to the propulsion system [51]:

$$\eta_{in} = \frac{\dot{N}_{tr}}{\dot{N}_\infty} \tag{2.3}$$

The incident mass flux not transmitted through the inlet, $\dot{N}_{reflected}$ is reflected back out of the front of the inlet. Inlet efficiency, η_{in}, is the key performance parameter for the inlet of an ABEP device and sensitivity of this parameter to ABEP performance mission capabilities will be assessed in the forthcoming analysis. While active inlets have been shown to achieve high η_{in} and high compression ratio, passive inlets are more widely covered in the literature; thus, this analysis will be limited to passive inlets [29, 52]. Passive inlets

generally rely on two capture methods: diffuse capture with collimators and an accumulator chamber and specular capture with a conical or parabolic inlet [53, 54, 9]. Atomic oxygen adsorption on surfaces leads to surface roughening and more diffuse scattering over time [55]. Specular collection methods rely on materials which can resist surface roughening and maintain persistent specular reflection. Such materials are currently under investigation [56], but none currently exist, so this work will be limited to diffuse collimator-accumulator designs [51, 7]. Previous investigations have shown that for passive collimator-accumulator type inlets η_{in} varies with inlet geometry and is inversely proporational to compression ratio of the inlet [57, 40]. Collimator-accumulator type inlets have been proposed in literature with η_{in} ranging from 20% to $> 45\%$ [54, 53]. Higher inlet efficiencies can be achieved at the cost of gas compression but this is generally considered undesirable [40, 57]. For this work $\eta_{in} = 0.35$ is assumed to be a reasonable estimate for applicable to a wide range of systems [52, 51, 58].

A_{in} in equation 2.2 can be replaced with $(A_{in} - A_{ex}\Theta)$ to capture the effect of particles passing completely through the inlet and thruster system and exiting out the back of the spacecraft without colliding with the spacecraft or another particle. Θ is the line-of-sight open area fraction at the exhaust plane. ABEP designs with no direct line-of-sight from the inlet through the thruster, such as the JAXA design described in [38], have $\Theta = 0$. Equation 2.2 assumes collisionless flow throughout the system. The increased air density inside the inlet and thruster system may cause collisions further reducing the number of particles which pass through the spacecraft without interacting. While the ambient flow is considered free-molecular with little inter-particle collisions, the inlet can compresses the flow to the point where inter-particle collisions become important. A multiplicative factor ζ may be applied to $A_{ex}\Theta$ to account for the gain in $\dot{m}$ due to increased particle collisions, where ζ ranges between 0 and 1 for full collisional and full collisionless flow respectively. Equation 2.2 then becomes $\dot{N}_s = \eta_{in} n_{a_s} u_\infty (A_{in} - A_{ex}\Theta\zeta)$. For common ABEP designs inlet area is much larger than thruster exhaust area, Θ is generally small for HETs and gridded ion thrusters, and

ζ is small for high compression inlets, so $A_{in} >> A_{ex}\Theta\zeta$ and $A_{ex}\Theta\zeta$ is a small correction. Under these assumptions, including $A_{ex}\Theta\zeta$ has little impact on final ABEP performance, so for this study it is assumed that $A_{ex}\Theta\zeta \approx 0$. ABEP concepts utilizing weakly compressing inlets, large exhaust areas, or high Θ should include the expansion $A_{in} \rightarrow A_{in} + A_{ex}\Theta\zeta$.

The exhaust velocity c_s for singly ionized species under electrostatic acceleration is given by:

$$c_s = \sqrt{\frac{2V_b q}{M_s}} \tag{2.4}$$

Equation 2.4 is valid for thrusters relying on electrostatic acceleration of ionized propellant such as Hall-effect thrusters and gridded ion thrusters. Combining equations 2.1, 2.2, and 2.4 yields the thrust of an ABEP device assuming frozen flow:

$$T = \sqrt{2qV_b}\eta_m\eta_{in}\gamma u_\infty \left(A_{in} - A_{ex}\Theta\right) \sum_s \sqrt{M_s} n_{a_s} \tag{2.5}$$

Given a maximum mass utilization efficiency, the maximum thrust for an ABEP system can be found with equation 2.5. Maximum thrust for a given altitude is limited by thruster performance parameters, inlet size, and inlet efficiency.

Additional seed gas propellant such as xenon can be mixed with the collected air to produce additional thrust or reduce the thrust to power $\left(T/P\right)$ of the device. These air augmented thrusters can be described by an additional term in the thrust equation:

$$T = \sqrt{2qV_b}\eta_m\gamma \left[\eta_{in} u_\infty \left(A_{in} - A_{ex}\Theta\right) \sum_s \sqrt{M_s} n_{a_s} + \frac{\dot{m}_{Seed}}{\sqrt{M_{Seed}}}\right] \tag{2.6}$$

In this case thrust is not limited by operating altitude and thrust can be increased by using onboard propellant. Equation 2.6 provides a first order description of the thrust produced by an ABEP device. System analysis with mixing air and onboard propellant is

outside the scope of this study, so this paper will focus on the fully air-breathing case where $\dot{m}_{fuel} = 0$ described by equation 2.5.

2.1.3 Drag

VLEO orbits are hallmarked by drag being the dominant perturbing force on a spacecraft, therefore, understanding and properly modeling drag forces is one of the most influential elements of spacecraft performance modeling in VLEO. Drag is dependent on geometry, attitude, and surface properties. In order to create a standard drag model, a reference spacecraft bus geometry is defined as shown in Figure 2.4.

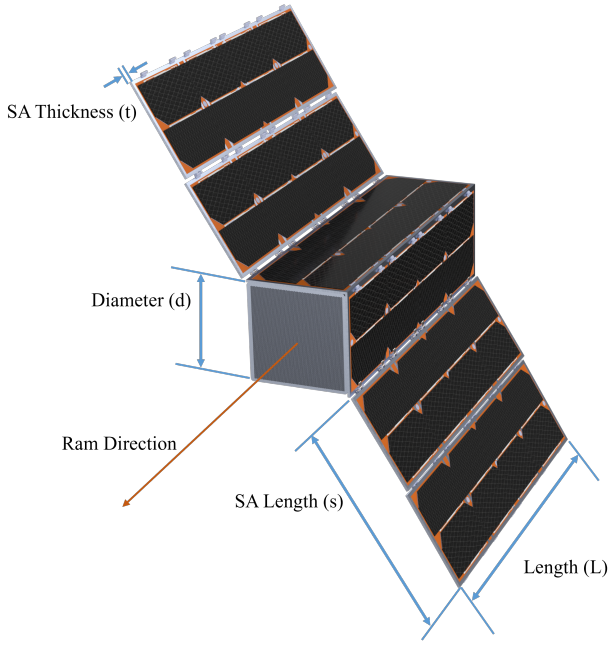

Figure 2.4: Diagram of the reference VLEO bus geometry used in this analysis. Length overall (L), solar array thickness (t_{SA}), and solar array length (s) are defined through ratios to the bus diameter d.

The geometry is defined by the bus diameter d, the ratio of length to diameter L/d, and the ratio of the solar array length to diameter s/d, or effectively how many folding solar array panels the geometry employs. The thickness of the solar arrays is defined by the ratio t_{SA}/s

which can be extrapolated from COTS solar array panels. This study will use $t_{SA}/s = 0.0083$ which was determined from CubeSat solar arrays [59]. Defining the geometry in terms of the diameter allows the spacecraft size to be scaled entirely by it's diameter, and it will be shown in later sections that overall performance is independent of size and only dependent on L/d and s/d.

2.1.3.1 Flow Regimes and Particle-Wall Interactions

Knudsen number (Kn) is defined as the ratio of the mean free path to a length scale. Kn is used to determine the type of flow model that is applicable to the problem [60]. Low Kn flows (Kn < 0.01) are considered continuum flows and the gas-dynamics are dominated by particle-particle collisions. High Kn flows (Kn > 10) are considered free-molecular where particle-wall collisions are more frequent than particle-particle collisions, and the gas-dynamics are dominated by particle-wall interactions. Statistical mechanics and direct simulation Monte Carlo (DSMC) methods are frequently applied to free-molecular flows [61]. Intermediate Kn values ($0.1 <$ Kn < 10) are considered transitional flows where particle-particle and particle-wall collisions are equally important.

Kn remains in the free-molecular flow regime for spacecraft as large as 1 m in diameter for altitudes above 150 km [56]. In free-molecular flows, after impacting a wall, the incident particle is reflected specularly, diffusely, or a combination of the two [62]. Specular reflection is akin to light reflecting off a mirror where the angle of incidence and the angle of reflectance are the same. Specular reflection usually occurs at clean, smooth surfaces. Rough surfaces lead to diffuse reflections where the angle of reflectance is determined by a Lambert cosine distribution. The degree to which a particle is specularly or diffusely reflected is determined by the accommodation coefficient σ, with $\sigma = 1$ corresponding to completely diffuse reflection and $\sigma = 0$ corresponding to completely specular reflection [62]. Thus, σ strongly influences the drag coefficient of the spacecraft.

2.1.4 Drag Model

The atmosphere at VLEO altitudes is rarified with large mean free path lengths leading to high Kn and free-molecular flow conditions. There are a number of analytical free-molecular flow drag models in literature [62, 63, 64]. The Storch drag model was chosen for this analysis, and the full equation for the flat plate drag coefficient is given as [62]:

$$\begin{aligned} C_D = 2\sigma_n \frac{V_w}{u_\infty} \sin^2\alpha + \frac{2}{\sqrt{\pi}S}\left[(2-\sigma_n)\sin^2\alpha + \sigma_t \cos^2\alpha\right] \exp\left(-S^2\sin^2\alpha\right) \\ +2\left[(2-\sigma_n)\left(\sin^2\alpha + \frac{1}{2S^2}\right) + \sigma_t\cos^2\alpha\right]\sin\alpha\,\mathrm{erf}(S\sin\alpha) \end{aligned} \tag{2.7}$$

It has been shown in the literature that spacecraft accommodation coefficients are very near 1 at VLEO altitudes due to adsorption of atomic oxygen to the surface increasing its roughness [65, 55, 66]. Applying the $\sigma_n = \sigma_t = 1$ assumption to equation 2.7:

$$C_D = 2\frac{V_w}{u_\infty}\sin^2\alpha + \frac{2}{\sqrt{\pi}S}\exp\left(-S^2\sin^2\alpha\right) + \frac{1}{S^2}\sin\alpha\,\mathrm{erf}(S\sin\alpha) \tag{2.8}$$

The reference geometry is comprised of multiple flat plate surfaces oriented either normal or parallel to the flow direction. We can then constrain equation 2.8 to only the normal incidence, $\alpha = 90\,\mathrm{deg}$:

$$C_{D_\perp} = 2\frac{V_w}{u_\infty} + \frac{2}{\sqrt{\pi}S}\exp\left(-S^2\right) + 2\left(1+\frac{1}{S^2}\right)\mathrm{erf}(S) \tag{2.9}$$

and parallel, $\alpha = 0\,\mathrm{deg}$, incidence angles:

$$C_{D_\parallel} = \frac{2}{\sqrt{\pi}S} \tag{2.10}$$

Where the speed ratio S is defined as $S \equiv \frac{u}{V_a}$, with V_a being the average thermal speed of the air molecules [62]. Figure 2.5 shows variation in C_D with altitude for the normal and

parallel incidence angles. $C_{D_\perp}$ does not change much over the altitude range, but $C_{D_\parallel}$ varies significantly with altitude increasing by more than 25% from 150 to 250 km altitude.

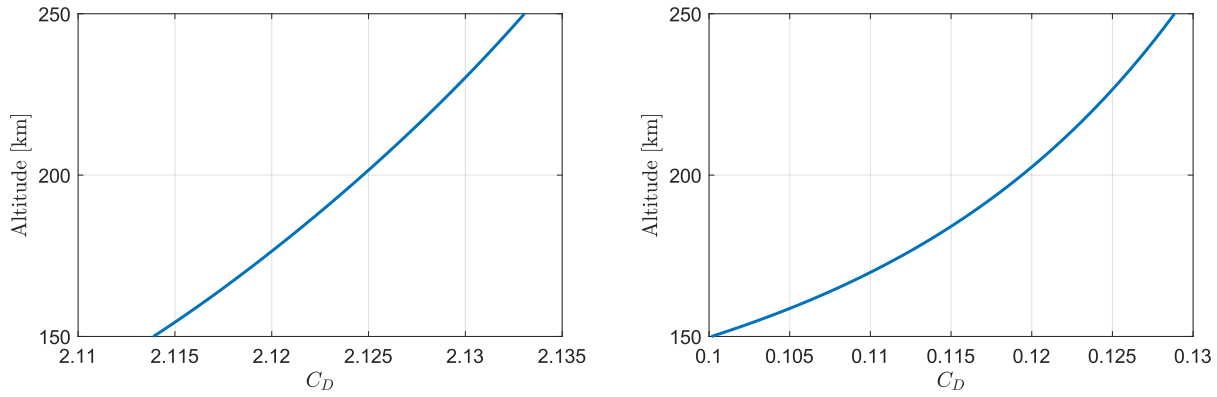

(a) $C_{D_\perp}$ for perpendicular incidence, $\alpha = 90°$ (b) $C_{D_\parallel}$ for parallel incidence, $\alpha = 0$

Figure 2.5: C_D for perpendicular and parallel incidence.

Drag on the front facing inlet is due to a combination of reflected particles described by the $C_{D_\perp}$ given by equation 2.9 which produce a drag force of $D_{reflected} = \frac{1}{2}\rho u^2 A_{in} C_{D_\perp}$ and ram drag due to particles captured by the inlet. Captured particles are described as inelastic collisions which impart a drag force of $D_{inelastic} = \rho u^2 A_{in}$. The ratio of reflected to absorbed particles is given by the inlet efficiency η_{in} defined by Equation 2.3. Thus the total drag force on the inlet can be written as $D_{in} = (1 - \eta_{in}) D_{reflected} + \eta_{in} D_{inelastic}$ or [2, 42]:

$$D_{in} = (1 - \eta_{in}) \frac{1}{2} \rho u_\infty^2 A_{in} C_{D_\perp} + \eta_{in} \rho u_\infty^2 A_{in} \tag{2.11}$$

For a flat plate at normal incidence $C_D \approx 2.13$ over the VLEO altitude range making the two terms in equation 2.11 almost the same, and thus η_{in} has little effect on drag.

Drag on the full spacecraft can be broken into two components: inlet drag and skin friction drag given by $D = D_{in} + D_{SF}$. Inlet drag is necessary for ABEP operation as there must be an inlet to collect air from the atmosphere. Skin friction drag is unnecessary

drag which can be reduced through the use of low drag materials with low accommodation coefficients. Summing the drag force on each surface yields the total drag force on the spacecraft:

$$D = \frac{1}{2}\rho u_\infty^2 \Bigg(2A_{SA}C_{D_\parallel} + 2A_{body}C_{D_\parallel} + (1-\eta_{in})\, A_{in}C_{D_\perp} \\ +2\eta_{in}A_{in} + 2st_{SA}C_{D_\perp} \Bigg) \tag{2.12}$$

$$\begin{cases} A_{SA} = s * L = d^2 \left(\frac{s}{d}\right)\left(\frac{L}{d}\right) & (2.13) \\ A_{in} = d^2 & (2.14) \\ A_{body} = d * L = d^2 \left(\frac{L}{d}\right) & (2.15) \\ st_{SA} = s^2 \left(\frac{t_{SA}}{s}\right) = d^2 \left(\frac{s}{d}\right)^2 \left(\frac{t_{SA}}{s}\right) & (2.16) \end{cases}$$

Through the way the reference geometry was defined, the total spacecraft drag is proportional to $A_{in} = d^2$.

$$D = \frac{1}{2}\rho u_\infty^2 A_{in} \Bigg(2\left(\frac{s}{d}\right)\left(\frac{L}{d}\right) C_{D_\parallel} + 2\left(\frac{L}{d}\right) C_{D_\parallel} + (1-\eta_{in}) C_{D_\perp} \\ +2\eta_{in} + 2\left(\frac{s}{d}\right)^2 \left(\frac{t_{SA}}{s}\right) C_{D_\perp} \Bigg) \tag{2.17}$$

Drag can be expressed as $D = \frac{1}{2}\rho u_\infty^2 A_{in} C_{D_{eff}}$ by defining an effective coefficient of drag:

$$C_{D_{eff}} = 2\left(\frac{s}{d}\right)\left(\frac{L}{d}\right) C_{D_\parallel} + 2\left(\frac{L}{d}\right) C_{D_\parallel} + (1-\eta_{in}) C_{D_\perp} \\ +2\eta_{in} + 2\left(\frac{s}{d}\right)^2 \left(\frac{t_{SA}}{s}\right) C_{D_\perp} \tag{2.18}$$

A breakdown of the drag contribution from each surface for two 10cm diameter spacecraft with differing L/d is shown in Figure 2.6. Doubling the L/d of the spacecraft from 3 to 6 causes the skin friction drag to overtake frontal area drag as the dominant drag force on

the spacecraft. Table 2.1 outlines the percent contribution from each drag source over the VLEO altitude range. In this table, drag is normalized to a point making drag independent of bus diameter and only dependent on L/d and s/d.

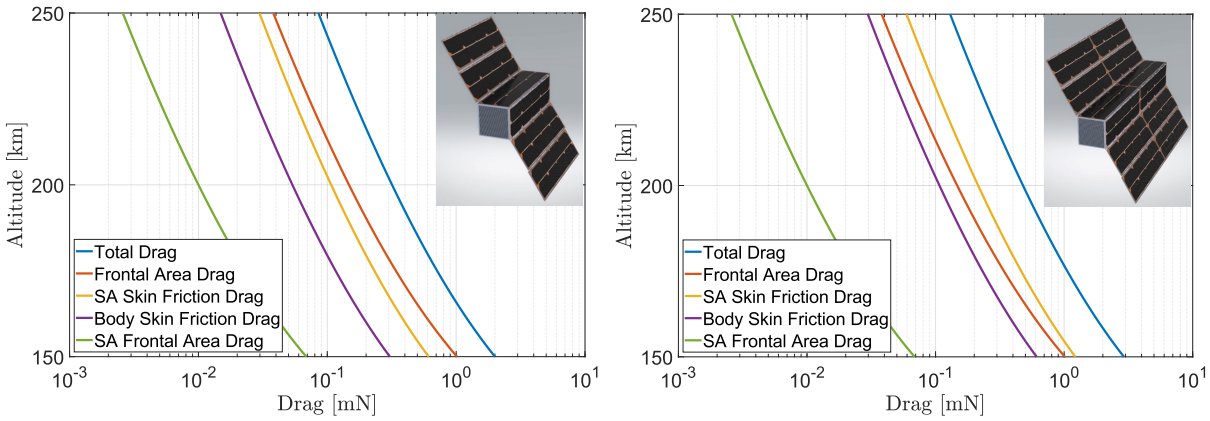

(a) 3U Drag

(b) 6U Drag

Figure 2.6: Drag comparison between a 1×3U and a 1×6U CubeSat

Orbital speed u is mostly constant with altitude for circular orbits in the VLEO altitude range. Atmospheric density ρ is roughly exponentially dependent on altitude, so for a given geometry, drag is dominated by $\rho \propto \exp(h)$. ρ is determined using the NRLMSISE-00 atmosphere model for this study.

2.1.5 Power Model

EP and ABEP spacecraft require power to drive the propulsion system. Power collected by a solar array is given by $P_{BOL} = \eta_{cell}\eta_{assy}\eta_t I_0 A_{SA} \cos\theta$ where θ is the angle between solar array normal and the solar vector [67]. The reference geometry described in Section 2.1.3 has two deployed solar arrays and body mounted solar panels over the entire length of the spacecraft bus which are angled 45° relative to the deployed solar arrays. The maximum available power to this reference spacecraft is given by:

Table 2.1: Percent drag contribution of each spacecraft surface for a $L/d = 6$ spacecraft. As altitude increases, skin friction drag becomes a larger percentage of the total drag due to an increase in C_D at higher altitudes for parallel incidence surfaces.

Altitude [km]	Total	Inlet	SA Skin	Body Skin	SA Frontal Area
150	1	36%	41%	21%	2%
160	63%	35%	42%	21%	2%
170	42%	34%	43%	21%	2%
180	29%	33%	43%	22%	2%
190	20%	32%	44%	22%	2%
200	14%	32%	44%	22%	2%
210	11%	32%	44%	22%	2%
220	8%	31%	45%	22%	2%
230	6%	31%	45%	22%	2%
240	4%	31%	45%	22%	2%
250	3%	30%	45%	23%	2%

$$P_{max} = 2\eta_{cell}\eta_{assy}\eta_t I_0 \left(A_{SA} + A_{body}\cos 45^\circ\right) \tag{2.19}$$

Similarly to drag in section 2.1.4, $P_{max} \propto d^2$. Typically, spacecraft will employ a combination of gimballed solar arrays and attitude control to point the solar arrays directly at the sun and collect maximum power. This is not an option in VLEO since the spacecraft must remain oriented with the minimum surface area in the direction of the velocity vector to keep drag at a minimum. At most, a compromise can be struck by rotating the spacecraft about its velocity vector as shown in Figure 2.7. The optimum spacecraft attitude for maximum power collection was derived by Singh [41].

The β angle is frequently used in spacecraft power analysis to determine the duration of

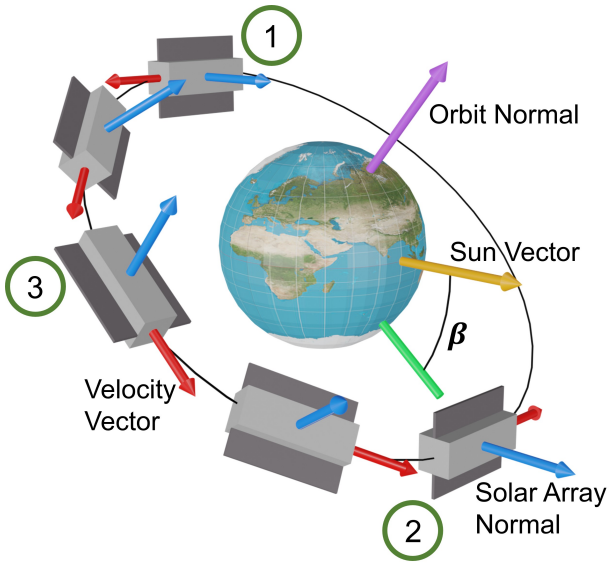

Figure 2.7: Diagram showing the optimal spacecraft attitude which maximizes collected power while keeping the spacecraft oriented for minimum drag. Spacecraft velocity vector is shown in red, solar array normal is shown in blue, orbit normal is shown in purple, and the sun vector is shown in yellow. β is the angle between the sun vector and the orbital plane.

eclipse periods and is defined as the angle between the orbital plane and the solar vector. Assuming the solar arrays can be rotated arbitrarily about the spacecraft velocity vector to collect the maximum amount of power, the collected solar array power is proportional to the magnitude of the cross product of the velocity unit vector and the solar unit vector: $P \propto \sin\psi$ where ψ is the angle between the solar vector and the velocity vector. At points 1 and 2 the spacecraft can be rotated such that the solar arrays are directly facing the sun and maximum power is collected. At point 3 the solar arrays make an angle $\frac{\pi}{2} - \beta$ to the sun. Assuming ψ varies sinusoidally between beta and pi/2 over the course of the orbit we can determine ψ:

$$\psi = \left(\frac{\frac{\pi}{2} - \beta}{2}\right)\cos(2\nu) + \frac{\frac{\pi}{2} + \beta}{2} \tag{2.20}$$

Instantaneous spacecraft power available when the spacecraft is not in eclipse is then

computed as:

$$\frac{P}{P_{max}} = \sin\psi \tag{2.21}$$

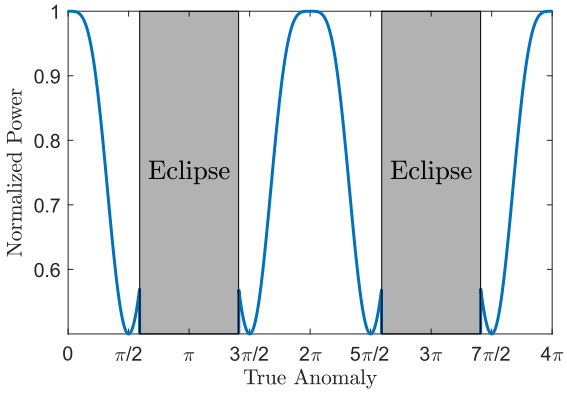

Figure 2.8: Power collected over two complete $\beta = 30°$, 200 km altitude orbits showing eclipse periods in grey and power reduction due to solar array cosine losses. Power is normalized to the maximum power collected. These results were verified using the Systems Toolkit software [4]

Beta angle analysis can then be applied to determine the eclipse fraction f_E of the orbit [68].

$$f_E = \frac{1}{\pi}\cos^{-1}\left[\frac{\sqrt{h^2+2Rh}}{(R+h)\cos\beta}\right] \tag{2.22}$$

Figure 2.8 shows the normalized power collected over two complete orbits including eclipse periods where no power is collected. Integrating over mean anomaly ν yields the mean power over the orbit as a function of the beta angle shown in Figure 2.9.

$$\frac{\bar{P}}{P_{max}} = \frac{1}{2\pi}\left(\int_0^{\pi\left(1-\frac{f_E}{2}\right)} \sin\psi\,\mathrm{d}\nu + \int_{\frac{\pi f_E}{2}}^{2\pi} \sin\psi\,\mathrm{d}\nu\right) \tag{2.23}$$

Average power can be reduced by as much as 70% from a sun-synchronous orbit leading to significant decreases in spacecraft performance. The results shown in Figures 2.8 and 2.9 are computed for a 200 km altitude circular orbit, but the results do not change significantly over the VLEO altitude range. This study will be limited to circular orbits and slightly elliptical orbits where the power analysis does not vary significantly from the circular case.

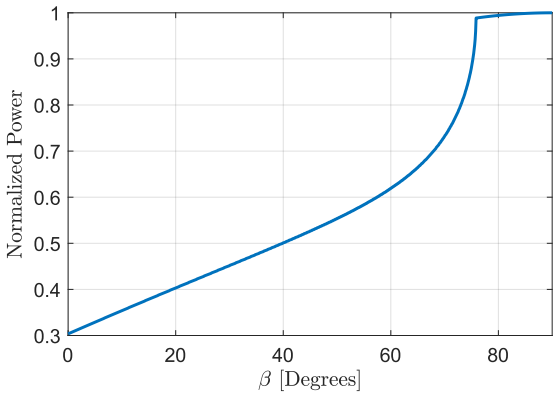

Figure 2.9: Normalized mean power collected vs β. High β orbits are in constant sunlight and do not have any eclipse periods. Low β orbits experience significantly reduced average power due to long eclipse periods and high cosine losses. This figure is computed for 200 km altitude, but the results do not vary significantly over the VLEO altitude range.

2.1.6 VLEO Orbit Types

ABEP spacecraft may operate in circular or elliptical orbits. Depending on mission needs, elliptical orbits can provide higher orbit apogee to reduce orbit average drag or allow a lower perigee for improved Earth proximity during part of the orbit. More highly elliptical orbits can be considered to further reduce the minimum operating altitude beyond what is possible with orbits entirely in the range of VLEO. These orbits can have apogee at a higher altitude where drag is reduced and dip to low altitudes near the Earth at perigee. These ”Super Low Perigee Orbits” (SuLPO) can provide benefits to certain space missions by bringing the

spacecraft very close to Earth for a portion of the orbit.

2.2 Results

2.2.1 Power Limited Altitude

A power-limited minimum operating altitude of any EP spacecraft can be determined through a power balance between the power required to compensate for drag, which is dependent on altitude, and the average power collected by the solar arrays over each orbit. Power required to compensate for drag is determined from the T/P of the propulsion system:

$$\bar{P} = D * \left(\frac{T}{P}\right)^{-1} \tag{2.24}$$

For a given geometry, average power available can be computed from the power model described in section 2.1.5, and drag can be determined as a function of altitude using equation 2.12. T/P is typically determined for each individual ABEP technology. Using the drag model, the power model, and an atmosphere model to relate atmospheric temperature and density to altitude, then the power limited minimum altitude can be determined by numerically solving Equation 2.24 for altitude.

As shown in Sections 2.1.4 and 2.1.5 both power available and drag are proportional to d^2. Scaling spacecraft diameter increases drag, but also scales the solar array size providing more power collected to compensate for drag. This scaling effect cancels in Equation 2.24 decoupling spacecraft performance from spacecraft diameter. Thus performance is only a function of $\frac{L}{d}$ and $\frac{s}{d}$. For example, a 3U CubeSat with 20cm long solar arrays (10 cm $\times$ 10 cm $\times$ 30 cm, $L/d = 3$, $\frac{s}{d} = 2$) can operate at the same altitudes as a larger scaled 1m $\times$ 1 m $\times$ 3 m, $L/d = 3$, $\frac{s}{d} = 2$ spacecraft provided T/P is the same for both propulsion systems. In practice, for a given type of thruster, larger thruster systems typically offer greater efficiency than smaller EP thrusters. Figures 2.10 show the power limited minimum operating altitude

for an EP or ABEP VLEO spacecraft with varying geometry and T/P.

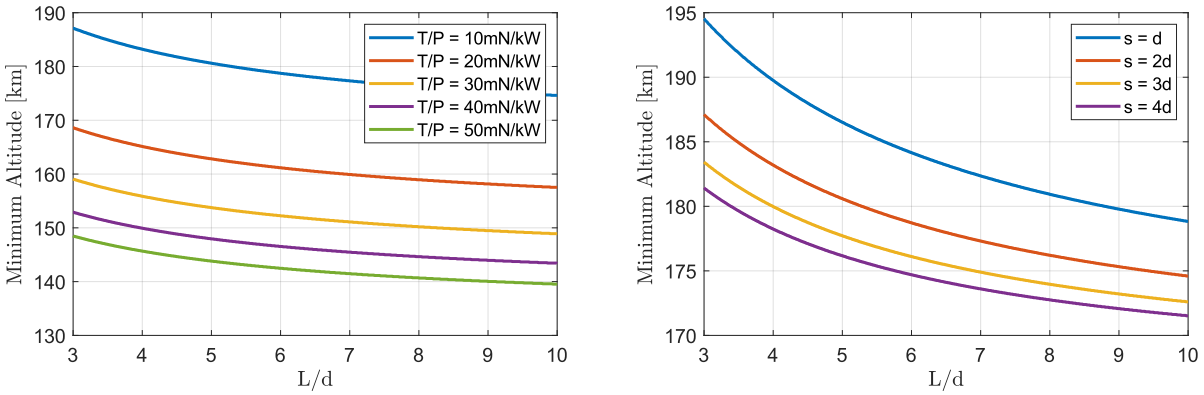

(a) $s = 2$ (b) $T/P = 10mN/kW$

Figure 2.10: Power limited minimum altitude for various geometries and T/P. T/P has the largest effect on minimum operating altitude.

Conventional HETs and gridded ion thrusters typically have high T/P in the 30 - 65 mN/kW range [69, 70] while ABEP propulsion has lower T/P in the 10 – 30 mN/kW range [7, 6] due to decreased performance from atmospheric propellants. Higher L/d spacecraft with larger solar arrays are able to collect more power and operate at lower altitudes. T/P has the greatest impact on the power limited minimum altitude, and improving T/P for the propulsion system leads to large decreases in operating altitude. Figure 2.11 shows how improving T/P reduces the power limited minimum altitude for a reference 6U geometry shown in Figure 2.6 at different solar activity levels. For this geometry, minimum operating altitude varies by up to 20 km over the solar cycle. Increasing T/P yields diminishing returns at lower altitudes approaching 150 km where atmospheric density increases rapidly as shown in Figure 2.1. Another concern is larger spacecraft operating at lower altitudes can approach the threshold for the transitional flow regime leading to further increases in drag not accounted for by this model.

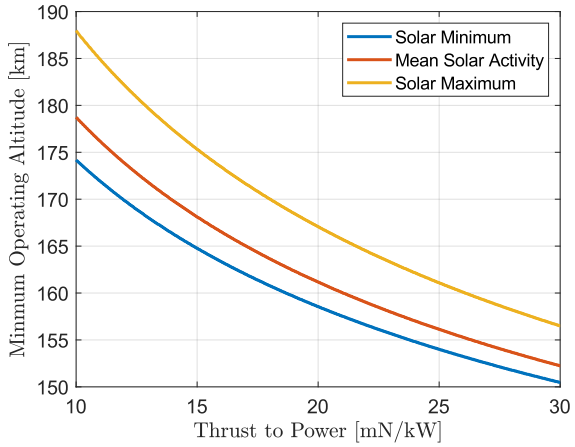

Figure 2.11: T/P vs power limited minimum operating altitude for the 6U reference geometry shown in Figure 2.6 $\left(L/d = 6, s = 2\right)$. Current air-breathing gridded ion thrusters achieve $T/P = 10$ mN/kW, inductive plasma thrusters can achieve $T/P = 20$ mN/kW [5, 6], and current air-breathing HET thrusters can achieve $T/P = 30$ mN/kW [7]. Minimum altitude varies by up to 20 km over the solar cycle for this geometry.

2.2.2 Thrust to Drag Ratio

In order for a spacecraft to maintain a stable orbit and avoid semi-major axis decay, adequate thrust must be produced to compensate for drag $T \geq D$, or $T/D \geq 1$. Equation 2.5 gives the thrust produced by an ABEP system, and equation 2.17 gives the drag on the spacecraft. Combining equations 2.5 and 2.17 and substituting $\sqrt{M_s} n_{a_s} = \frac{\rho_s}{\sqrt{M_s}}$ where ρ_s is the partial density given as $\rho_s = \mathcal{C}_s \rho$:

$$\frac{T}{D} = \frac{2\sqrt{2qV_b}\eta_m \eta_{in} \gamma \left(A_{in} - A_{ex}\Theta_n\right) \sum_s \mathcal{C}_s M_s^{-1/2}}{u_\infty A_{in} C_{D_{eff}}} \tag{2.25}$$

$\mathcal{C}_s$ is the mass fraction of each species in the atmosphere. The ρ dependence has dropped out of equation 3.4 removing any strong dependence on altitude. u_∞ varies slightly over the VLEO altitude range, and $C_{D_{eff}}$ is also weakly dependent on altitude through the speed ratio S and the ambient mean thermal velocity V_a. M_s varies slightly over the altitude range

due to composition changes in the atmosphere. Therefore T/D is mostly constant with altitude shown in Figure 2.12. Additionally, if $A_{ex}\Theta_n << A_{in}$, which is generally desirable to minimize propellant loss, then dependence on A_{in} also drops out of equation 3.4.

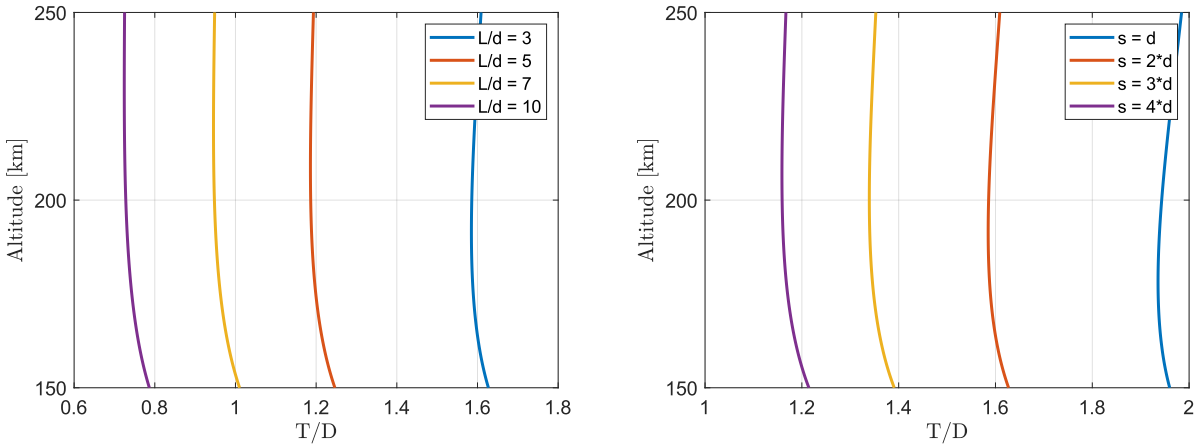

(a) $s/d = 2$ (b) $L/d = 3$

Figure 2.12: T/D vs altitude for a range of L/d. T/D is mostly constant with altitude with some variation due to small changes in $C_{D_{eff}}$ and u_∞ with altitude.

As L/d and s/d increases, drag increases as well, but the maximum thrust produced remains constant due to the constant inlet size. High L/d and s/d ABEP spacecraft have $T/D < 1$ and therefore cannot maintain a stable orbit. High power spacecraft are desirable to reduce the power limited minimum operating altitude, but high power spacecraft also suffer from low T/D which could make the geometry unviable if $T/D < 1$.

2.2.3 Parameter Sweep

The power limited minimum altitude model and the T/D model can be applied in a parameter sweep over a range of spacecraft geometries, thruster T/P, and orbit β angles to map these inputs to minimum operating altitude and T/D. Geometries with L/d between 3 and 10 and between 1 and 4 solar array panels are investigated. $L/d > 10$ and $s/d > 4$ are

considered unrealistic and not structurally sound. Current gridded ion thrusters running on atmospheric propellants achieve $T/P \approx 10$ mN/kW while current Hall thrusters running on atmospheric propellants can achieve $T/P \approx 30$ mN/kW [6, 7]. A range of T/P between 10 - 30 mN/kW is chosen to encompass the full range of current ABEP technology. β angles ranging from 0° to 90° encompasses the entire range of possible orbit cases. For each combination of inputs, the minimum T/D is checked to ensure $T/D \geq 1$. T/D is roughly constant with altitude, so only checking the minimum is considered sufficient for this analysis. Minimum operating altitude is then determined by the power limited minimum altitude analysis described in section 2.2.1. T/D is computed for the power limited minimum altitude.

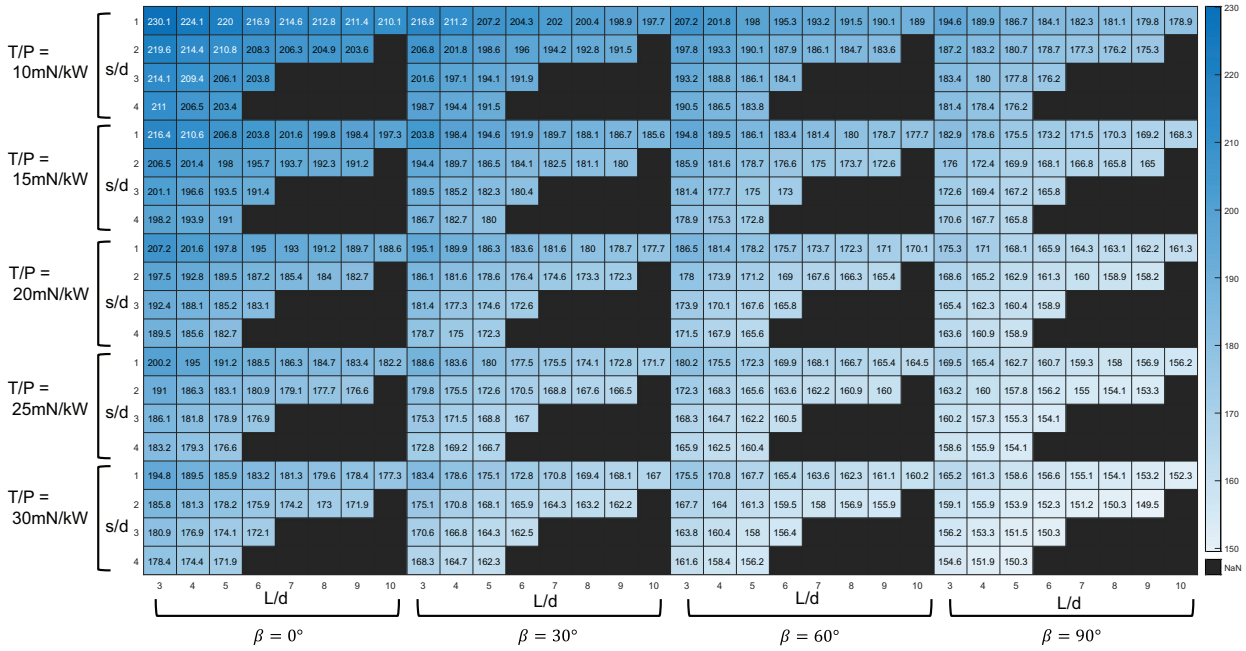

Figure 2.13: Minimum operating altitude for a range of spacecraft geometries, T/P, and β for an ABEP with $V_b = 1500$ V, $\eta_m = 0.85$, $\eta_{in} = 0.35$, $\gamma = 1$. Cases with $T/D < 1$ are blacked out. High β orbits offer lower altitude operation since they offer more power to the spacecraft.

Figures 2.13 and 2.14 show the results of the parameter sweep with $V_b = 1500$ V and Figures 2.15 and 2.16 show the results of the parameter sweep with $V_b = 500$ V. Current

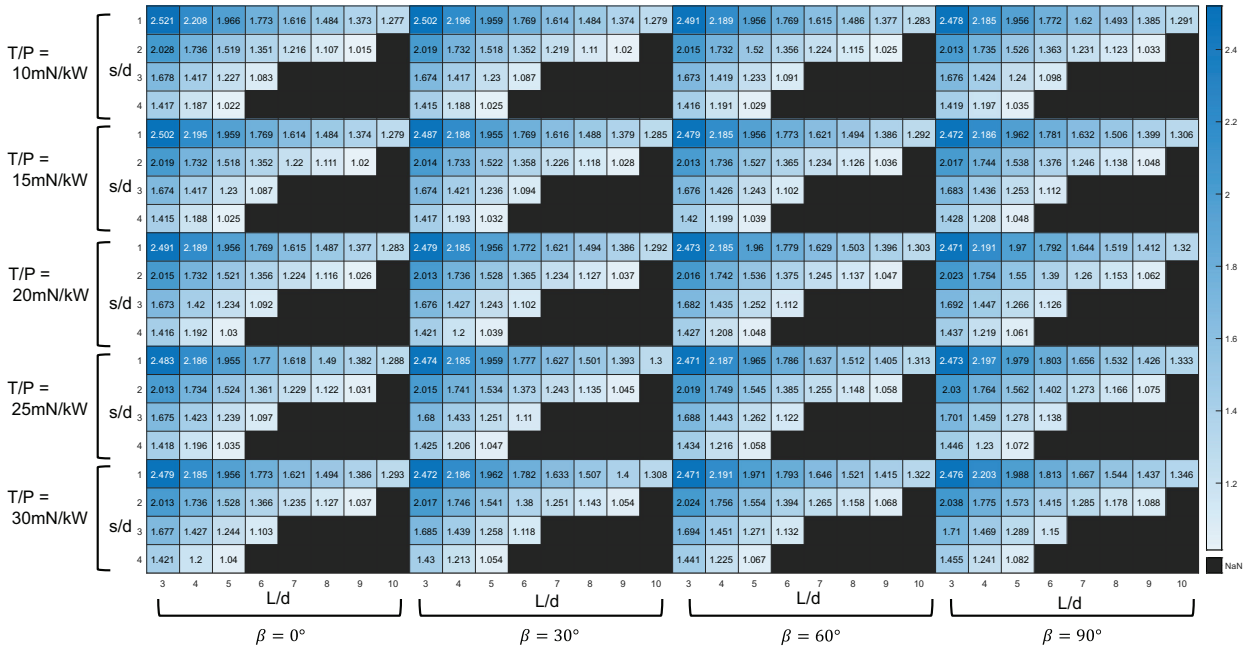

Figure 2.14: T/D for a range of spacecraft geometries, T/P, and β for an ABEP spacecraft with $V_b = 1500$ V, $\eta_m = 0.85$, $\eta_{in} = 0.35$, $\gamma = 1$. Cases with $T/D < 1$ are blacked out.

ABEP gridded ion thrusters have a T/P of 10 mN/kW and can support an ABEP spacecraft at a minimum of 175 km. ABEP HETs have a T/P of 30 mN/kW, but cannot provide as high T/D due to lower effective exhaust velocity per equation 3.4 and can support a spacecraft to as low as 155 km. Geometries with $T/D = 1$ are viable, but spacecraft designers may wish to use designs with slightly higher T/D to improve maneuverability and spacecraft survivability in unexpected environmental conditions. Aerodynamic maneuvering and orbit changing requires $T/D > 1$ to accommodate increased drag during these maneuvers.

Actuated solar arrays can be retracted during eclipse periods when they do not collect power to reduce drag. The mean drag over a complete orbit is computed as a weighted average of the total spacecraft drag with the solar arrays deployed and the total drag with the solar arrays retracted:

$$D = (1 - f_E)D_{\text{SA Deployed}} + f_E D_{\text{SA Retracted}} \tag{2.26}$$

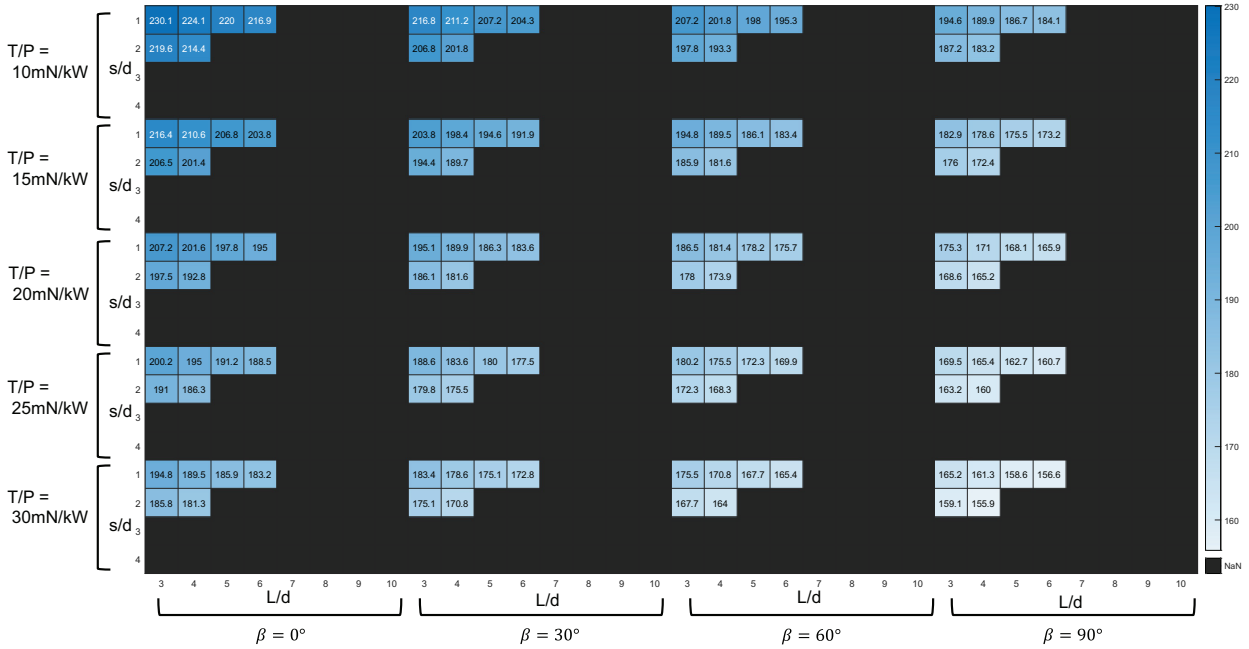

Figure 2.15: Minimum operating altitude for a range of spacecraft geometries, T/P, and β for an ABEP with $V_b = 500$ V, $\eta_m = 0.85$, $\eta_{in} = 0.35$, and $\gamma = 1$. Cases with $T/D < 1$ are blacked out. High β orbits offer lower altitude operation since they offer more power to the spacecraft. Note for $V_b = 500$ V lower T/D is achievable than for the high V_b case shown in Figure 2.13 and only low drag geometries are feasible.

where the weighting factor f_E is the eclipse period computed from a beta angle analysis. Retracting solar arrays reduces minimum operating altitude by up to 10km for geometries with large solar arrays. The added mass and complexity of actuated solar arrays may outweigh the relatively minor benefits. Additionally, atmospheric density is usually reduced on the eclipse side of the Earth further reducing the benefit of retracting the solar arrays during eclipse periods. Equation 2.26 is only valid for circular orbits. Elliptical orbits may benefit more from retracting the solar arrays for certain portions of the orbit, but that analysis is outside the scope of this study.

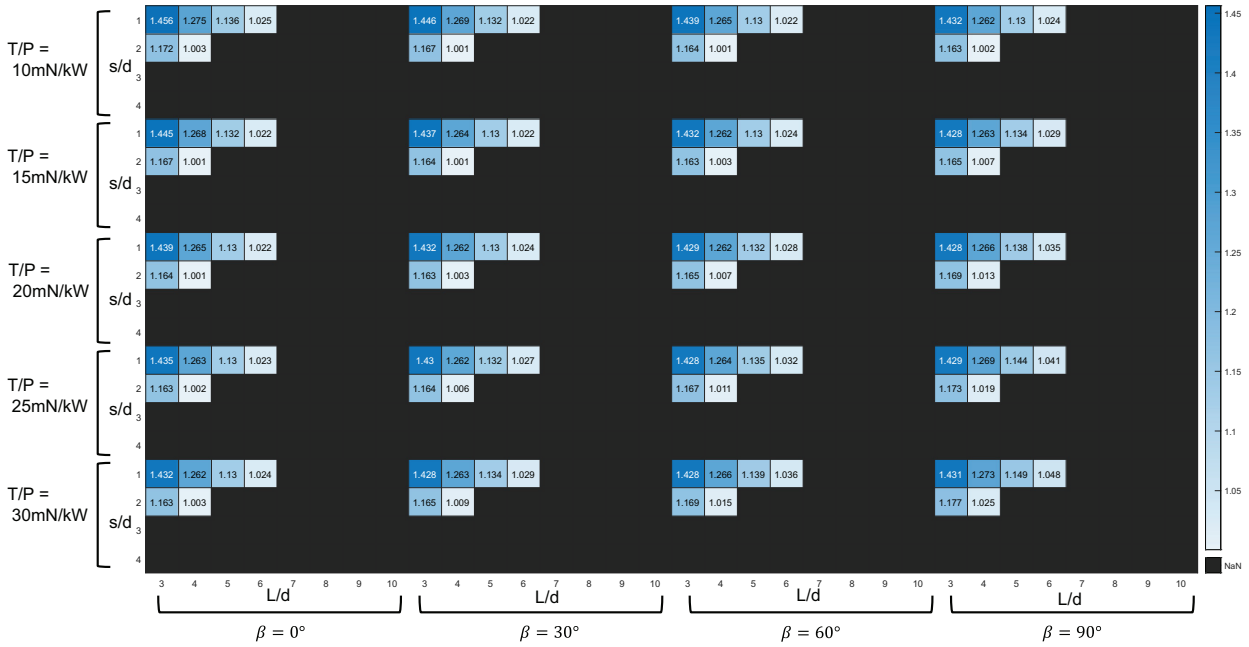

Figure 2.16: T/D for a range of spacecraft geometries, T/P, and β for an ABEP spacecraft with $V_b = 500$ V, $\eta_m = 0.85$, $\eta_{in} = 0.35$, and $\gamma = 1$. Cases with $T/D < 1$ are blacked out.

2.2.4 Comparison Between Conventional EP and ABEP

Conventional EP spacecraft operating in VLEO can be analyzed using the drag model from section 2.1.4, and propellant requirements can be determined from mission lifetime and drag compensation requirements. The parametric analysis in Section 2.2.3 shows that a spacecraft with $L/d = 6$ and $s/D = 2$ is found to perform well. A 6U ABEP CubeSat shown in Figure 2.17 can be directly compared to a conventional EP 6U spacecraft using the same bus. This analysis is similar to the analysis of a high ΔV CubeSat [71].

2.2.4.1 6U CubeSat With Conventional EP

A total volume of 6U is provided by the spacecraft bus, and the subsystem layout is shown in Figure 2.18. The propulsion unit is assumed to occupy 1.6U of volume based on commercial CubeSat EP thrusters [8]. COMMS, ADCS, and EPS are estimated to occupy 1.5U of

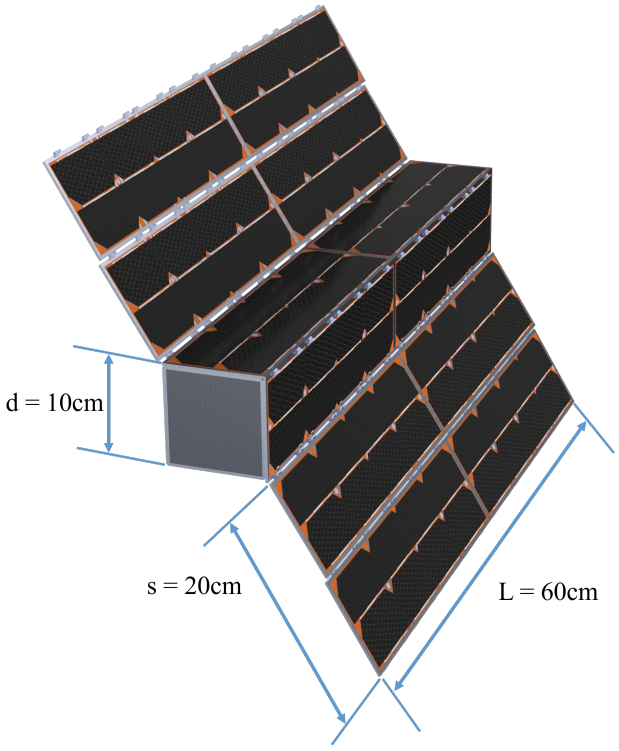

Figure 2.17: 6U CubeSat (10 cm×10 cm×60 cm, $s = 20$ cm). The ABEP variation has the air inlet on the front as shown. The conventional EP case has a flat front. Both configurations have similar drag.

volume in the spacecraft [71]. EPS mass is estimated to be 0.14 kg [72]. This leaves 2.9U for propellant and payload. The propellant tank is assumed to be at a temperature of 322 K and pressure of 161 bar [71]. As the propellant requirements grow, the propellant tank grows as a sphere until it is 9 cm in diameter, then it becomes stretched to become a cylinder [71].

Figure 2.19 shows the effect on payload volume vs spacecraft altitude and mission lifetime. At lower altitudes, the remaining payload volume decreases until there is no payload volume remaining and the spacecraft reaches its minimum altitude. The lifetimes shown in Figure 2.19 are in agreement with previous studies [39, 25] Similarly to high ΔV spacecraft, thruster I_{sp} has a major impact on propellant requirements. Spacecraft wet mass increases at lower altitudes and longer mission lifetimes due to the increased propellant mass required for low

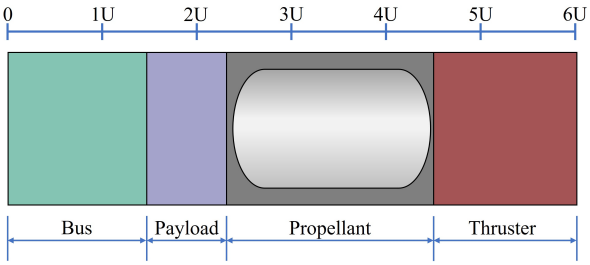

Figure 2.18: Block diagram of the subsystem layout in the 6U EP spacecraft. As propellant requirements increase, the propellant tank grows, reducing payload volume.

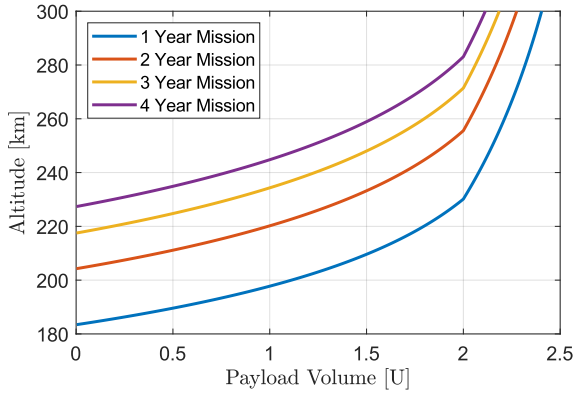

Figure 2.19: Payload volume of the 6U CubeSat operating in VLEO with a 2000 s I_{sp} EP propulsion system. The kink seen at 2U payload volume is where the propellant tank switches from expanding as a sphere to stretching as a cylinder.

altitude and long mission lifetimes. The 6U reference spacecraft has an estimated 5.3 kg dry mass not including propellant tank mass. Figure 2.20 shows how wet mass increases with increasing mission lifetime and decreasing operating altitude. The reference spacecraft can collect 96 W at peak solar power. For orbits that are not sun-synchronous with low β angles, the mean power collected is reduced by eclipse periods and non-optimal solar array pointing as shown in section 2.1.5. Lower altitude orbits require more thruster power to compensate for drag leaving less power available to the payload and other systems. Figure 2.21 shows the remaining power available to the spacecraft for a variety of orbit types. Lower altitude orbits

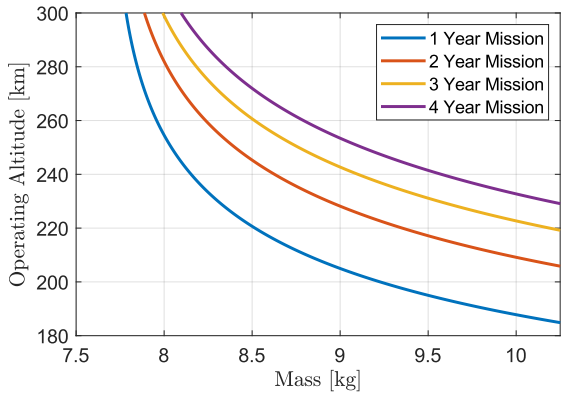

Figure 2.20: Wet mass of the 6U CubeSat operating in VLEO with a 2000 s I_{sp} EP propulsion system. The CubeSat has a dry mass of 5.3 kg not including propellant tank mass.

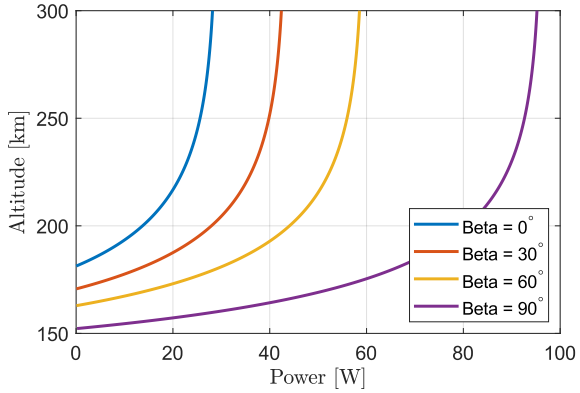

Figure 2.21: Power available to the payload and other subsystems for a 6U CubeSat operating in VLEO with a $T/P = 30$ mN/kW EP propulsion system [8].

leave very little power remaining for subsystems, and the power limited minimum altitude is considered where all of the available power is sent to the propulsion system to compensate for drag and the remaining power is zero. In practice, the minimum operating altitude will be above the power limited minimum altitude due to power draws from other subsystems.

2.2.4.2 6U ABEP CubeSat

The same 6U bus is now investigated for an ABEP propulsion system. Again, the bus provides 6U of total volume with 1.5U allotted to electronics and 1.6U allotted to the propulsion unit. The air handling system (AHS) includes the inlet and a tube that runs the length of the spacecraft to deliver air from the inlet in the front of the spacecraft to the thruster in the back as shown in Figure 2.22. ABEP spacecraft designers will need to take the AHS into consideration when planning spacecraft layout. AHS volume was estimated to be 0.54U. The remaining payload volume is then determined to be a constant 2.36U. The mass of the spacecraft is estimated using data from [71, 8] to be 8.05 kg including a standard mass margin [73]. ABEP spacecraft are lighter and less complicated than conventional EP spacecraft operating at similar altitudes since ABEP does not require heavy propellant, tankage or plumbing. Tables 2.2 and 2.3 show the complete mass and volume allocation for both the ABEP and conventional EP 6U reference spacecraft.

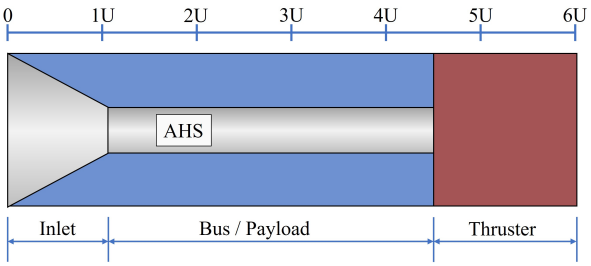

Figure 2.22: Block diagram of the 6U ABEP CubeSat Layout. This layout is similar to ABEP CubeSat layouts described by Jackson [9].

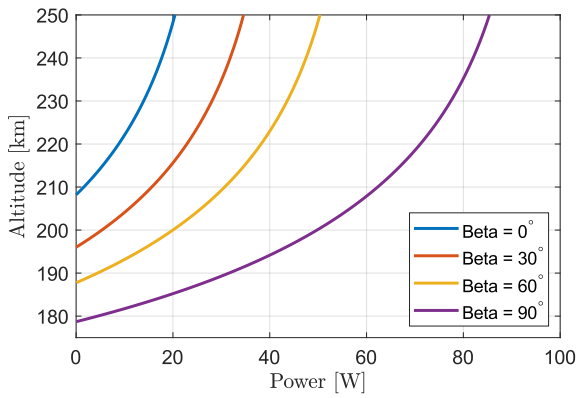

Figure 2.23: Power remaining for spacecraft subsystems and payload. At lower altitudes more power must be supplied to the propulsion system to compensate for drag. At low β average power collected is significantly reduced due to long eclipse periods and high cosine losses.

Table 2.2: Conventional EP (240 km, 3 year mission life) and ABEP Allocated Mass Budgets

		Conventional EP	ABEP
Subsystem	Component	Mass (kg)	Mass (kg)
Propulsion			
	Thruster System	1.40	1.40
	Tank	0.34	–
	Plumbing & Flow Control	0.20	–
	Propellant	0.68	–
	AHS	–	0.32
Structure			
	Primary Structure	1.10	1.10
	10x10 cm Panels	0.70	0.70
	Brackets	0.15	0.15
Power			
	EPS	0.14	0.14
	Battery	0.15	0.15
	Solar Panels	0.80	0.80
ADCS			
	Integrated ADCS Board	0.62	0.62
Thermal		0.15	0.15
CDH			
	CDH Board	0.10	0.10
COMM			
	COMM Board	0.10	0.10
	Antenna	0.10	0.10
20% Contingency		1.35	1.17
15% Margin		1.21	1.05
Total		9.29	8.05

Table 2.3: Conventional EP (240km, 3 year mission life) and ABEP Allocated Volume Budgets

		Conventional EP	ABEP
Subsystem	Component	Volume (U)	Volume (U)
Propulsion			
	Thruster System	1.6	1.6
	Tank	1.7	–
	AHS	–	0.5
Bus		1.5	1.5
Payload		1.2	2.4
Total		6	6

Figure 2.23 shows the remaining power available to the payload and other onboard systems. The minimum altitude is where the power available goes to zero and the spacecraft sends all available power to the propulsion system. High β orbits are favorable to provide larger amounts of power to the spacecraft and allow for lower altitude operation.

2.2.5 Super Low Perigee Orbit Analysis

The power limited minimum altitude of a SuLPO spacecraft can be found using an energy balance between the average power collected on orbit and the energy lost to drag over the orbit:

$$\int_0^T \bar{P}\,\mathrm{d}t = \int_0^T Drag * u\,\mathrm{d}t \tag{2.27}$$

Where $\bar{P}$ is given by Equation 2.23 and drag is given by Equation 2.17. Figure 2.24 shows the power limited minimum altitude for a range of geometries and apogee altitudes. SuLPO can have extreme instantaneous power requirements as shown in Figure 2.25. These instantaneous power requirements can limit the minimum altitude above the energy limited minimum altitude. Advanced, high-power propulsion technologies such as capacitor driven MPD thrusters may be desirable for SuLPO missions.

2.2.6 Discussion

The model results show that ABEP spacecraft can provide a unique and desirable mission capability for VLEO below 250 km. In contrast, conventional EP is favorable for shorter mission lifetimes at higher altitudes. The primary restrictions for EP for lower altitudes and longer mission lifetimes is due to propellant tank volume significantly reducing usable payload volume, as well as increasing overall mass of the spacecraft. Therefore, high I_{sp} EP is still the favorable choice for moderate mission lengths at higher altitudes. At lower altitudes and longer mission lifetimes, ABEP provides more payload volume than conventional EP,

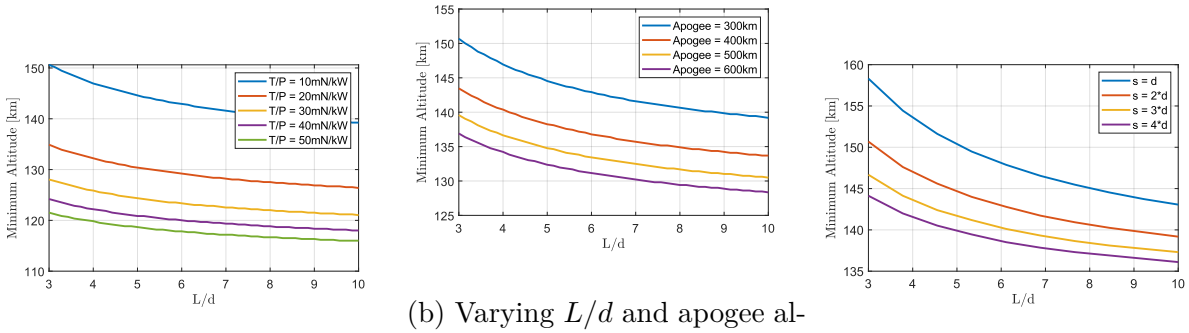

(a) Varying L/d and T/P.

(b) Varying L/d and apogee altitude.

(c) Varying L/d and s.

Figure 2.24: Power limited minimum perigee altitude for SuLPO orbits. $T/P = 10$ mN/kW, Apogee = 300 km, and s/d = 2 unless otherwise stated in the figure. These figures assume $\beta = 90°$.

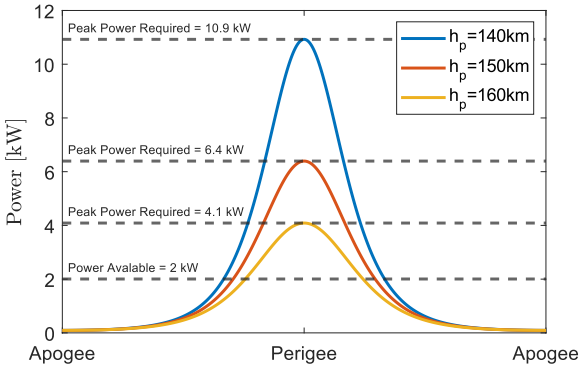

Figure 2.25: Instantaneous power required for SuLPO orbits with perigee altitudes of 140, 150, and 160 km and apogee at 300 km. The spacecraft bus is 50 cm × 50 cm × 250 cm. SuLPO spacecraft will need advanced high-power propulsion and power processing systems.

albeit less payload power. At lower altitudes ABEP is limited to high β orbits due to a combination of long eclipse times and SA cosine losses. Sun-synchronous orbits offer the highest ABEP performance, but as low as $\beta = 30°$ orbits are still viable for low-power payloads. $\beta = 0$ offers the worst ABEP performance and mission designers should avoid

these orbits if possible.

Spacecraft with high L/d and large solar arrays are favorable for ABEP spacecraft allowing them to collect large amounts of power to feed the propulsion system. There is a limit to the maximum wetted area of the spacecraft as the thrust is fixed for a given propulsion system and inlet area, and spacecraft designers must check to ensure that their spacecraft geometry can achieve $T/D \geq 1$. Higher T/D may be desirable to ensure spacecraft survivability at higher-than-expected atmospheric density or to allow for improved maneuverability. A linear 6U form factor with a 2 panel SA was determined to perform well for an ion thruster based ABEP system offering a $T/D = 1.35$ and a minimum altitude of 179 km in a SSO. HET based ABEP systems benefit from improved T/P relative to ion thrusters but suffer from reduced thrust due to the reduced effective exhaust velocity. A 4U spacecraft with 1 solar array panel offers the best performance for a HET ABEP system with $T/D = 1.27$ and a minimum altitude of 161 km in an SSO. Larger spacecraft with the same geometry scaling provide the same performance provided that the propulsion system offers the same T/P. Larger propulsion systems typically provide higher efficiency which could improve ABEP performance for larger spacecraft.

Compression ratio is a concern for operating ABEP thrusters as a minimum gas density must be maintained inside the thruster for proper operation. This gas density limit constrains the range of possible inlet efficiencies and also sets an upper altitude limit on ABEP operation as described in [32]. Deterioration of ABEP thruster components is a concern due to the highly reactive propellant, and oxygen resistant materials must be chosen to resist thruster erosion. Lotz performed grid erosion measurements a modified RIT-10 thruster and measured minimal erosion with titanium grids over a 500 hour test. Extended lifetime testing and accurate grid modeling is required to ensure thruster operation for longer durations.

ABEP performance can be improved with higher T/P propulsion, improved SA efficiency, low drag materials, and highly efficient inlet designs. Higher T/P enables lower altitude operation for ABEP spacecraft and leaves more power for the payload as less power is required

to maintain the orbit. Figure 2.11 shows the dependence of minimum operating altitude on thruster T/P. HET based ABEP offers higher T/P than gridded ion ABEP, but ABEP HETs are limited to smaller bus sizes due to the reduced effective exhaust velocity. Improved solar array efficiency is desirable for almost every space mission, but ABEP missions benefit by having more power available to the propulsion system and enabling lower altitude operation. Figure 2.26 shows the minimum operating altitude of an example 6U spacecraft with increasing solar cell efficiency. Low drag materials offer reductions in skin friction drag by retaining a low accommodation coefficient in VLEO altitudes and are currently being investigated by ESA's SOAR spacecraft [56]. Decreasing accommodation coefficient can facilitate up to a 25 km decrease in operating altitude as shown in Figure 2.27. Low drag materials also decrease propellant requirements for low-altitude conventional EP spacecraft. Improvements to inlet efficiency provides higher propellant flow rates to the ABEP propulsion system improving T/D. Increasing η_{in} from 35% to 45% increases T/D from 1.4 to 1.8 for the 6U reference spacecraft (V_b = 1500 V). Higher T/D improves spacecraft maneuverability and improves performance for aerodynamic attitude control and orbital maneuvers.

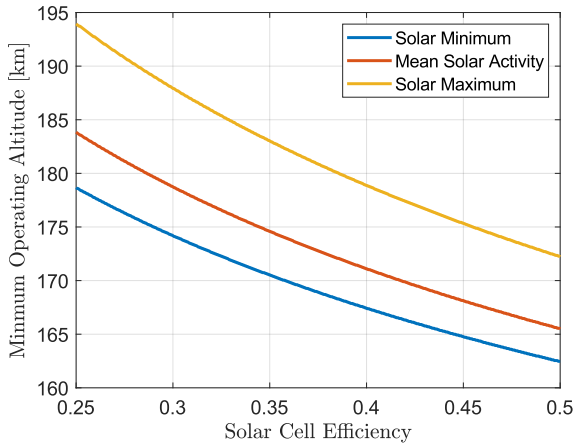

Figure 2.26: Power limited minimum operating altitude for an ABEP spacecraft with T/P = 10 mN/kW with varying solar array efficiency.

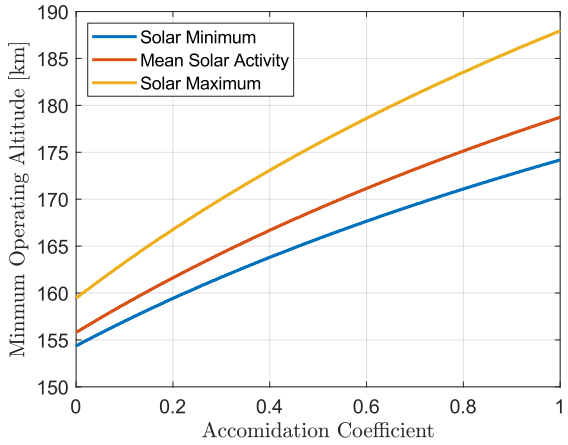

Figure 2.27: Power limited minimum operating altitude for an ABEP spacecraft with T/P = 10 mN/kW with varying accommodation coefficients. An accommodation coefficient of 0 leads to $C_{D_{\|}} = 0$ and no skin friction drag. The remaining drag is due to frontal area drag.

2.3 Aerodynamic Forces

Characterizing spacecraft lift and drag as a function of yaw angle is useful for predicting performance of aerodynamic maneuvers and estimating the effect of horizontal wind on the spacecraft. A bus geometry similar to the one shown in figure 2.17 was used, but the box shaped spacecraft body was replaced with a cylindrical body of diameter d and length L to simplify calculations.

Lift and drag coefficients (C_L and C_D) are given as a function of incidence angle by Storch for a flat plate and a cylindrical shell [62].

Incidence angle for slip surfaces is simply the yaw angle ψ while incidence angle for the inlet surface is given as $\frac{\pi}{2} - \psi$. Total drag on the spacecraft neglecting contribution from the front face of the solar arrays is given by $D = \frac{1}{2}\rho u_\infty^2 A_{in} C_{D_{eff}}$ where $C_{D_{eff}}$ is:

$$C_{D_{eff}} = 2\left(\frac{s}{d}\right)\left(\frac{L}{d}\right) C_{D_{plate}}(\psi) + \left(\frac{L}{d}\right) C_{D_{cyl}} + \left(1 - \eta_{in}(\psi)\right) C_{D_{plate}}(\frac{\pi}{2} - \psi) + 2\eta_{in}(\psi) \quad (2.28)$$

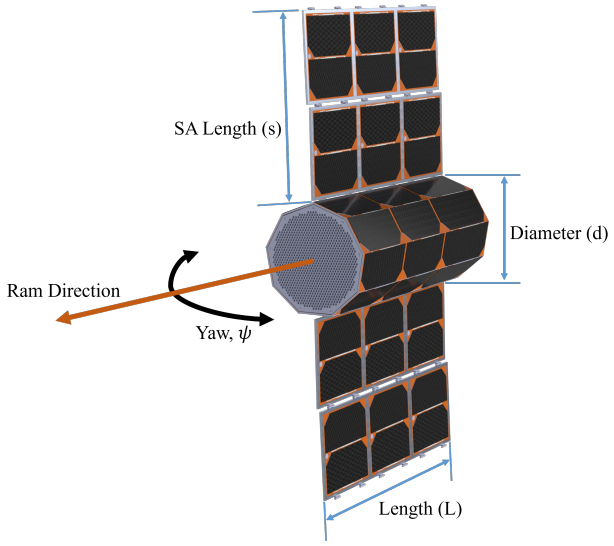

Figure 2.28: Diagram of the reference VLEO bus geometry used for aerodynamic force analysis. Length overall (L), solar array thickness (t_{SA}), and solar array length (s) are defined through ratios to the bus diameter d.

$C_{D_{plate}}$ and $C_{D_{cyl}}$ are the drag coefficients for a cylinder and flat plate as functions of ψ given by Storch [62]. η_{in} is a function of ψ as well, generally decreasing with increasing yaw [57]. Total lift generated by the spacecraft is given in a similar manner by $L = \frac{1}{2}\rho u_\infty^2 A_{in} C_{L_{eff}}$.

$$C_{L_{eff}} = 2\left(\frac{s}{d}\right)\left(\frac{L}{d}\right) C_{L_{plate}}(\psi) + \left(\frac{L}{d}\right) C_{L_{cyl}}(\psi) \tag{2.29}$$

Equation 2.29 neglects lift forces generated by the inlet surface which was found to be much smaller than lift generated by slip surfaces. Figure 2.29 shows the lift and drag coefficients for the spacecraft bus shown in figure 2.28.

It can be seen from the figure that yaw has little effect on drag for $\psi < 2°$. Parodi showed that an ABEP in a sun-synchronous orbit experiences a maximum yaw of 4 degrees [40]. For the case shown in figure 2.29, C_D increases by 28% from $\psi = 0$ to $\psi = 4°$. C_L with $\sigma = 0$ remains low for all yaw angles. Figure 2.30 shows C_L/C_D increasing for decreasing accommodation coefficient. High accommodation coefficient surfaces provide very poor lift-to-drag

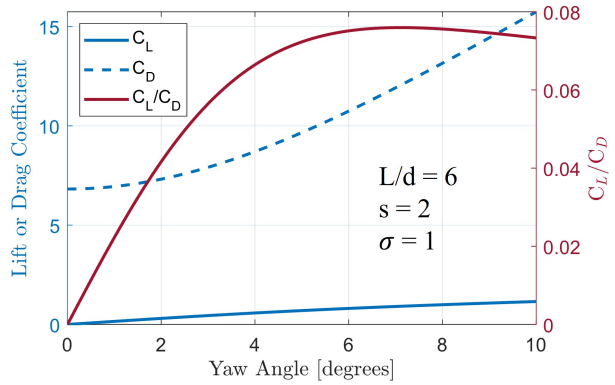

Figure 2.29: Coefficients of lift, drag, and lift to drag ratio for the spacecraft shown in figure 2.28 as a function of yaw angle for $L/d = 6, s = 2, \sigma = 1$.

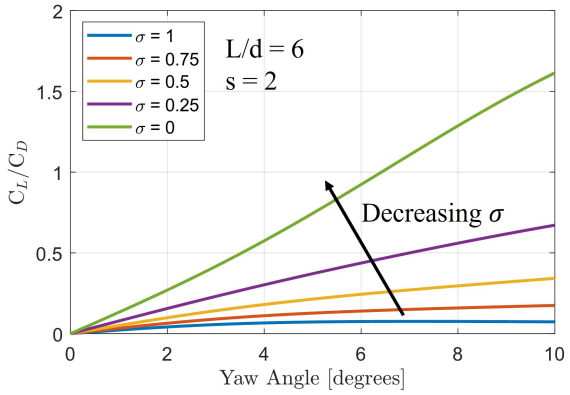

Figure 2.30: Lift to drag ratio for the spacecraft shown in figure 2.28 as a function of yaw angle for varying accommodation coefficients for $L/d = 6, s = 2$. Note $\sigma = 1$ is entirely diffuse reflection and $\sigma = 0$ is entirely specular reflection.

resulting in poor performance for aerodynamic maneuvers. Low accommodation coefficient materials which resist oxygen adsorption are required to enable aerodynamic maneuvering capabilities with high lift-to-drag.

2.4 Mission Study Conclusions

A model was developed to determine ABEP spacecraft performance based on spacecraft geometry and propulsion performance for VLEO orbits. It was found that spacecraft performance is not directly dependent on overall spacecraft size but rather on important non-dimensional geometric ratios such as spacecraft length-to-diameter (L/d) and solar array span to spacecraft diameter (s/d). Power collected on orbit was shown to be heavily dependent on β angle, leading to up to 70% reductions in average power collected from the SSO case for a VLEO spacecraft. The major drivers of ABEP spacecraft performance were shown to be T/D, η_{in}, L/d, and s/d. A parametric sweep was applied to find geometries which lead to the lowest operating altitude. Given a geometry optimized for low altitude operation, increasing T/P is the most fruitful way to further reduce the minimum operating altitude. It has been shown that a target $T/P = 10$ mN/kW can achieve sustained VLEO operation, while increases beyond this target can greatly improve performance.

ABEP CubeSat performance was compared with a conventional EP CubeSat with the same bus geometry to determine mission scenarios which favor ABEP over conventional EP. It was found that for missions of 3 years or longer, payload volume becomes severely reduced for EP spacecraft below 240 km and ABEP spacecraft become favorable, which is in agreement with previous studies [25].

CHAPTER 3

Geomagnetic Storm Risk to ABEP Missions

The February 2022 loss of several Starlink satellites due to increased drag during a geomagnetic storm event highlighted the geomagnetic storm risks associated with very low Earth orbit (VLEO) operation [74, 75, 76]. Air-breathing electric propulsion (ABEP) spacecraft in VLEO may face even greater mission risk than spacecraft with conventional electric propulsion (EP) due to the lower efficiency of ABEP thrusters and the lower VLEO altitudes proposed for ABEP missions [28, 26, 6, 77]. EP operating on air constituents, nitrogen and oxygen, has significantly reduced thrust-to-power compared with xenon thrusters, and thus ABEP operational altitude is severely constrained by the spacecraft power budget [10, 32]. ABEP missions which push their power budget to maintain orbit in calm conditions may be overcome by intense solar storms. For multi year missions, it is expected that several storms of up to G4 intensity will need to be endured by the spacecraft particularly during the solar cycle peak [78].

For ABEP mission viability, it is important to address risks such as those posed by geomagnetic storms. This work discusses two risk mitigation strategies: (1) preemptive orbit raising based on forecasted geomagnetic activity and (2) using onboard xenon propellant to enhance thruster performance during high drag events. Preemptive orbit raising is the simplest to implement as it requires no additional complexity onboard the spacecraft, but it requires accurate storm forecasting and may degrade mission performance during geomagnetic storms. Including xenon onboard to improve thruster performance during high drag periods may decrease power requirements during geomagnetic storms improving survivabil-

ity, but including xenon onboard significantly increases spacecraft complexity.

VLEO operation is difficult due to the large impact atmospheric drag has on the orbit, and onboard propulsion is required to compensate for drag and maintain the orbit. For long duration missions at low altitudes, propellant requirements using conventional EP technology become prohibitively large [25, 10]. Air-breathing EP (ABEP) reduces or removes these propellant constraints by collecting air from the local atmosphere to use as propellant. Multiple organizations are currently developing ABEP technologies based on a variety of EP devices [28, 79].

ABEP spacecraft generally operate in the 150-250km altitude range. EP thrusters operating on air constituents, primarily N2 and O2, exhibit much lower efficiency than with traditional propellants such as xenon resulting in much higher power draws [28, 26, 6, 77]. Previous ABEP mission studies have shown that the maximum drag an ABEP spacecraft can tolerate is significantly limited by the spacecraft power budget leading to many proposed spacecraft with large, high drag, solar arrays operating at low T/D [10, 32]. Rapid increases in drag due to geomagnetic storms can easily overwhelm the ABEP propulsion system and drop the spacecraft into an unrecoverable lower altitude orbit. The loss of 38 Starlink satellites, which used conventional EP, in February 2022 highlights the danger of geomagnetic storms to VLEO spacecraft [74, 75, 76].

Geomagnetic storms are transient events caused by high energy coronal mass ejections (CME) from the sun impacting the Earth's magnetic field. During a geomagnetic storm, highly energetic charged particles from the CME are injected into the magnetosphere energizing the ions in the magnetosphere ring current resulting in a decrease of the earth's magnetic field strength [80]. The reduction in magnetic field strength is catalogued by the Disturbance Storm Time (Dst) index which is determined by magnetometer measurements near the magnetic equator [81]. Increased ionospheric currents are induced at high latitudes driving atmospheric heating [82]. Heating causes the thermosphere to expand and increases density for a given altitude. Density increases initially occur at high latitudes and then

diffuse to lower latitudes over the course of several hours [83].

Previous ABEP mission studies have used orbit propagators to investigate long term drag compensation [32, 41]. Parodi (2019) performed orbit propagation with $T/D = 1$ for VLEO orbits to resolve ranges on several atmospheric properties including relative flow velocity and yaw angle through the HWM14 model [40]. Singh (2014) used the Systems Toolkit software (STK) to propagate an ABEP spacecraft and primarily investigated power requirements [41]. Tiseav et al. (2022) performed orbit propagation using the NRLMSISE-00 atmosphere model and incorporating an active altitude controller [32]. The orbit was simulated for 500 days from Jan. 1st 2000 to May 15th 2001 during which time the spacecraft experiences several high DST events, most notably on March 30th 2001 [11]. While this event caused a subsequent drop in altitude, the spacecraft was able to recover provided thrust-to-power was high enough. As the focus of Tisaev's work was on long term orbital stability, short term effects due to increased geomagnetic activity are not discussed. Tisaev et al., (2022) found that increasing spacecraft mass improved long term survivability, investigating spacecraft with ballistic coefficients in the range 400-3300 kg/m^2.

This chapter extends the current body of work in ABEP orbit propagation by focusing on short term effects from geomagnetic storms. The majority of previous publications have used the NRLMSISE-00 atmosphere model because it is able to predict orbit composition, but this model is less accurate than the Jacchia-Bowman 2008 (JB2008) model during periods of high geomagnetic activity [84]. This chapter incorporates the JB2008 model improving density resolution during geomagnetic storms. Additionally, this work investigates spacecraft with lower ballistic coefficients than those investigated by Tisaev et al. which exhibit a stronger response to drag effects.

Section 3.1 describes the orbit propagator and atmosphere model implementation. Methods for determining spacecraft parameters and thruster performance described. Geomagnetic storm impacts on spacecraft for a base, no action, case and for both risk mitigation strategies are presented in section 3.2.

3.1 Geomagnetic Storm Risk Analysis Approach

To investigate geomagnetic storm effects on ABEP spacecraft, an orbit propagator was used with the JB2008 atmosphere model and a simple ABEP performance model. Orbit propagation was performed using the Simulink spacecraft dynamics block [85]. This orbit propagator uses the EGM2008 spherical harmonic model.

For atmospheric density, the JB2008 atmosphere model was chosen over the NRLMSIS-00 atmosphere model due to its greater resolution in capturing density variations during geomagnetic storms [84]. JB2008 computes atmospheric density and temperature at a specified latitude, longitude and altitude, and can resolve variations based on solar cycle through the 10.7cm radio flux index, and geomagnetic activity through the DST index [86].

Spacecraft drag coefficients are computed using a panel method for spacecraft geometries as described in [10] for the reference spacecraft shown in Figure 3.1. All geometric features are normalized to the reference length d with $A_{in} = d^2$. Spacecraft maximum power, P_0, is given by [10]:

$$P_{max} = 2\eta_{sa} I_0 A_{in} \left(\left(\frac{s}{d}\right) \left(\frac{L}{d}\right) + \left(\frac{L}{d}\right) \cos 45^\circ \right) \tag{3.1}$$

Where solar array efficiency $\eta_{sa} = 0.22$ and incident solar flux $I_0 = 1367$ W/m^2 [67]. For this analysis, the spacecraft is assumed to be in a sun synchronous orbit and always collects maximum power. Eclipse durations can be taken into account by adding a margin on the maximum collected power. It is assumed that a maximum of 70% of the total spacecraft power is sent to the thruster leaving 30% power for subsystems. Thus the thruster power is $P_0 = 0.7 P_{max}$.

ABEP thruster performance is described in terms of the thrust to power, T/P, and the specific impulse, I_{sp}. Testing performed by Lotz (2013) on a RIT-10 gridded ion thruster running on air (1.27:1 N2 to O2) yielded $T/P = 12.8$ mN/kW and $I_{sp} = 5455$ s [6, 32]. Thrust

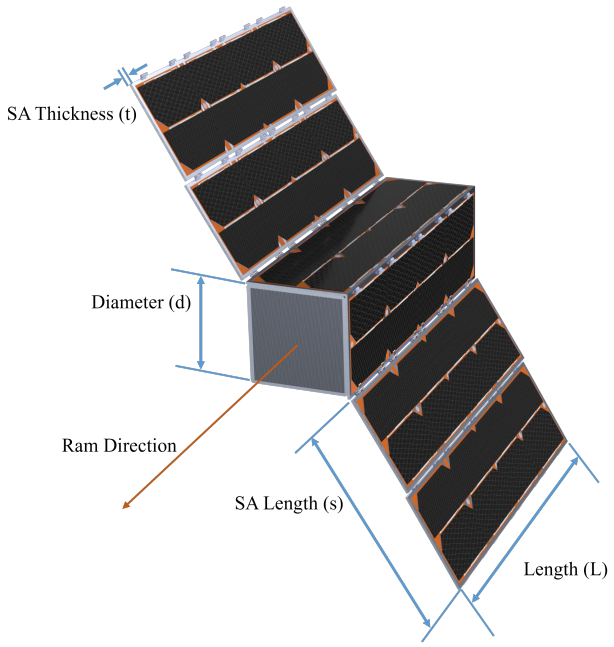

Figure 3.1: Diagram of the reference VLEO bus geometry used in this analysis [10]. Length overall (L), solar array thickness (t_{SA}), and solar array length (s) are defined through ratios to the bus diameter d.

produced by the spacecraft is defined to be the lesser of $T = \dot{m} I_{sp} g$ and $T = (T/P) P_0$ where $g = 9.81$ m/s^2. $\dot{m} = \eta_{in} \rho u_\infty A_{in}$ is the mass flow rate collected by the inlet and delivered to the thruster where ρ is the ambient atmospheric density, A_{in} is the inlet area, and η_{in} is the inlet efficiency. Inlet compression is neglected in this analysis, and it is assumed that the inlet can always provide sufficient compression to operate the thruster.

All orbits are initialized to a Keplarian orbit with $|\vec{r}| - R_e = 190$ km, inclination of 98°, zero eccentricity, right ascension of ascending node of zero, zero true anomaly, and an argument of periapsis of zero. While all orbits are initialized in circular orbits, the non-sphericity of Earth's gravity results in a small amount of eccentricity [32].

A large geomagnetic storm in November 2004 was chosen as a reference storm for this study [87]. This storm reached a peak Kp of 8.66 placing it at G4 (severe) intensity [88, 78]. On average, there are 60 days with G4 storms in an 11 year solar cycle [78]. Figure 3.2 shows the DST index for the reference storm.

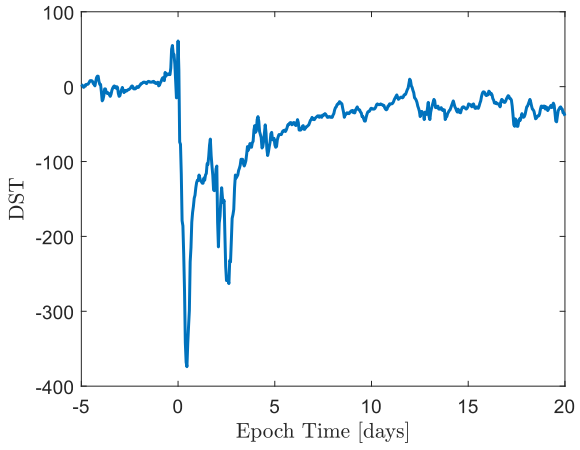

Figure 3.2: DST index for the reference storm. The geomagnetic storm begins when DST sharply drops negative. Data from [11].

3.1.1 Spacecraft Parameter Selection

Given equations for thrust and drag:

$$T = \dot{m} I_{sp} g = \eta_{in} \rho u_\infty A_{in} I_{sp} g \tag{3.2}$$

$$D = \frac{1}{2} \rho u_\infty^2 C_d A_{in} \tag{3.3}$$

The thrust to drag ratio can be written as:

$$\frac{T}{D} = \frac{2 \eta_{in} I_{sp} g}{u_\infty C_d} \tag{3.4}$$

T/D is independent of atmospheric density and is only a function of spacecraft geometry through C_d, inlet performance through η_{in}, and thruster specific impulse, I_{sp} [10, 32, 89]. The RIT-10 gridded ion thruster running on a N_2-O_2 mixture has been shown to achieve $I_{sp} = 5455$ s [6, 32]. Passive air intakes can achieve $\eta_{in} = 0.35$ with active inlets achieving higher efficiency [79]. Using $I_{sp} = 5455$ s, $\eta_{in} = 0.35$, $u_\infty = 7800$ m/s, and setting $T/D = 1$, the maximum viable C_d for these parameters can be computed as $C_d = 4.8$. A spacecraft body defined as in Figure 3.1 with $L/d = 5$ and $s/d = 1$ has $C_d = 4.4$ yielding $T/D = 1.09$.

The impact of mass on the spacecraft drag response is determined by the ballistic coefficient $C_b = \frac{m}{C_d A_{in}}$. For the GOCE spacecraft, $C_b = 297$ kg/m^3 [90]. While GOCE used traditional EP with onboard propellant, it is commonly used as a reference for ABEP spacecraft as operating altitudes and spacecraft geometries are similar between GOCE and proposed ABEP spacecraft [79, 32]. Taking $\frac{m}{A_{in}}$ to be in the range 400-1200 kg/m^2 gives a C_b range of $C_b = 90 - 272$ kg/m^2. Higher C_b reduces the impact of drag and improves spacecraft survivability.

3.2 Survivability Results

3.2.1 No Action

Prior to the storm, the spacecraft is set to operate in drag free mode where thrust is the lessor of drag or the maximum producible thrust based on equation 5.7 respecting $T \leq (T/P)P_0$. Epoch time $t = 0$ is set to be when the interplanetary magnetic field (IMF) B_z component flips negative based on the ACE spacecraft data [91]. For the reference storm this is Nov. 7th 2004 20:00:00. For the baseline case, the spacecraft is in drag free mode until $t = 0$ when it switches to always producing maximum thrust per equation 5.7 and $T \leq (T/P)P_0$ which allows the spacecraft to produce $T > D$ when able and raise its orbit.

For the base case of no action, survivability is found to be largely dependent on C_b and T/D. High C_b dampens transient drag effects and thus the spacecraft is able to ride through the relatively short drag increase during the storm. Figure 3.3 shows propagated orbits for fixed T/D and increasing C_b by increasing spacecraft total mass. Low C_b spacecraft are highly susceptible to drag effects, but as C_b is increased reentry is delayed until ultimately the spacecraft survives.

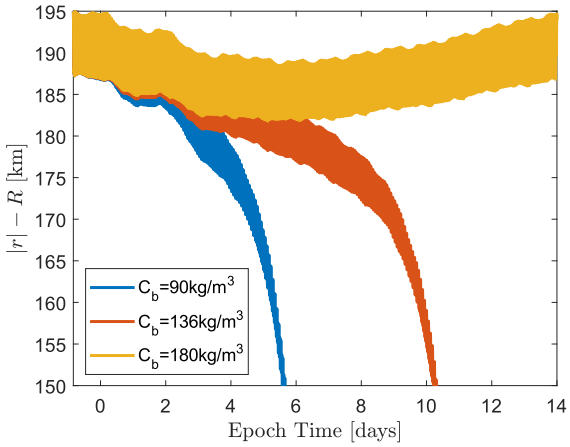

Figure 3.3: Propagated orbits for $\eta_{in} = 0.4$ and $C_b = 90, 136$, and 180 kg/m^2. Higher C_b spacecraft can survive the storm without advanced risk mitigation.

Spacecraft of all C_b with lower T/D are also more susceptible to geomagnetic storms as there is less excess thrust to make up for high drag periods. Figure 3.4 shows propagated orbits for fixed C_b and several T/D values. T/D is varied through the inlet efficiency η_{in} to keep thruster performance parameters constant. Spacecraft with higher T/D show improved survivability overall and do not require advanced risk mitigation. Low T/D spacecraft cannot effectively recover from the storm and quickly deorbit.

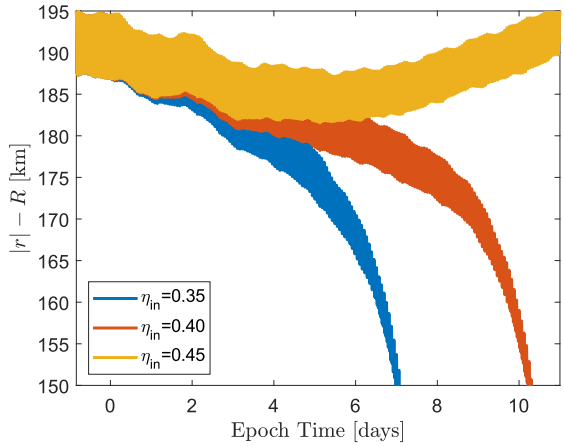

Figure 3.4: Propagated orbits for $C_b = 136$ kg/m^2 and $\eta_{in} = 0.35, 0.40$, and 0.45 corresponding to initial $T/D = 1.09, 1.25$, and 1.40 respectively. Higher T/D spacecraft can survive the storm without advanced risk mitigation.

The accumulated net along-track impulse, J, defined as equation 3.5 can be used to gauge spacecraft survivability. During high drag periods of the solar storm, $T/D < 1$ resulting in an impulse deficit which must be made up for during low drag periods. A spacecraft is assumed to survive the storm if J returns to zero after the storm passes.

$$J = \int_0^{t_1} (T - D)\, \mathrm{d}t \tag{3.5}$$

Figure 3.5 shows the accumulated impulse for $C_b = 90, 181$ and $\eta_{in} = 0.4, 0.45$. For low C_b spacecraft, net impulse diverges negative as thrust cannot keep up with drag resulting in

the spacecraft quickly deorbiting. Higher C_b spacecraft do not lose as much altitude, so the propulsion system can produce $T > D$ and regain lost impulse after the storm peak.

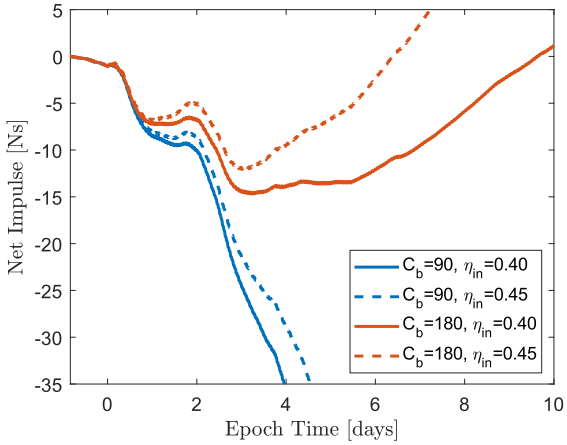

Figure 3.5: Net impulse for four spacecraft parameter sets. During the storm an impulse deficit is created due to increased drag which is then made up for during low drag periods.

For the no action case, spacecraft with high C_b and high T/D should be robust to geomagnetic storms and require no mitigation. Low C_b and low T/D spacecraft cannot regain impulse lost during the storm due to the limited power available onboard the spacecraft and require advanced risk mitigation strategies such as preemptive orbit raising or xenon addition. Low C_b spacecraft can employ either risk mitigation method, but low T/D spacecraft cannot create excess thrust to preemptively raise altitude, so low xenon addition is the only risk mitigation strategy available to low T/D spacecraft.

3.2.1.1 C_d During a Geomagnetic Storm

During the geomagnetic storm, ambient temperature increases significantly which changes the speed ratio $S = \frac{u_\infty}{V_a}$ where V_a is the most probable thermal velocity [62]. As atmospheric temperature increases during the storm, S decreases which increases drag on spacecraft surfaces perpendicular to the flow. Figure 3.6 shows an example of the evolution of C_d over the course of the reference storm for a spacecraft with $L/d = 5$ and $s/d = 1$. At the storm

peak C_d is 12% higher than during quiet times. Additional effects such as yaw angle may further increase C_d [40].

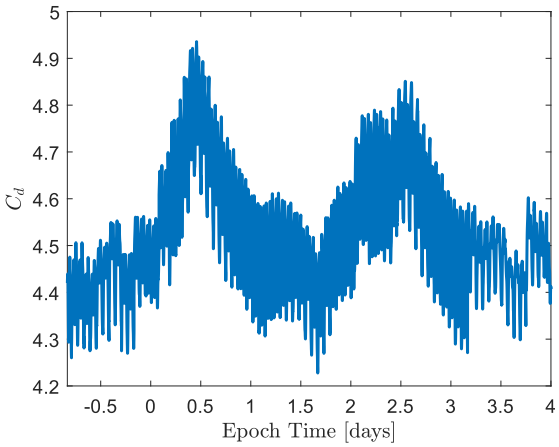

Figure 3.6: C_d for $L/d = 5$ and $s/d = 1$ during the reference storm.

3.2.2 Preemptive orbit raising

Preemptive orbit raising is modeled by removing the drag free limitation on thrust to times prior to $t = 0$ allowing $T/D > 1$ raising the spacecraft orbit ahead of the storm's arrival. Inlet efficiency is set to $\eta_{in} = 0.45$ making $T/D = 1.4$ allowing the spacecraft greater T/D margin to raise its orbit in calm atmospheric conditions, and ballistic coefficient is set to $C_b = 90$ kg/m^2. Figure 3.7 shows the effect of removing the drag free limitation at $t = -1, -4$, and -5 hours.

As the drag free limitation is lifted at earlier times, the spacecraft has additional time to accumulate positive impulse ahead of the storm arrival reducing altitude loss during the storm peak and improving survivability. It can be seen in Figure 3.7 that for the simulated $\eta_{in} = 0.45, C_d = 4.8, C_b = 90$ kg/m^2 case the drag free condition must be lifted at $t = -5$ hours for the spacecraft to survive the storm.

While accurate geomagnetic storm prediction is difficult, several probabilistic models

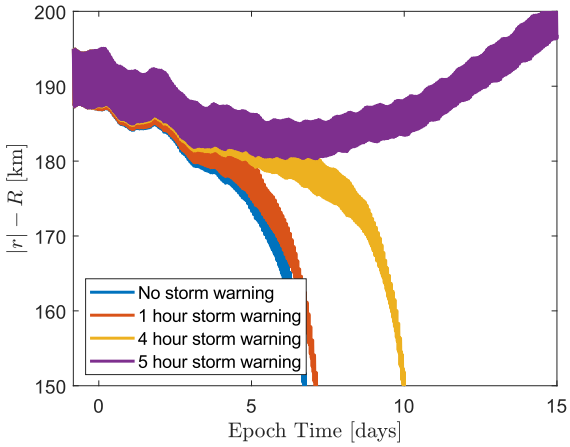

Figure 3.7: Propagated orbits for $\eta_{in} = 0.45, C_d = 4.8, C_b = 90$ kg/m^2. $t = 0$ is set to be when the IMF B_z crosses zero at 20:00:00 on November 7th 2004.

exist. The National Oceanographic and Atmospheric Administration (NOAA) provides a 3 day forecast for the Kp index [92], and several additional predictive models exist as well [93, 94]. Thus preemptive orbit raising may be a simple way to mitigate geomagnetic storm risks for spacecraft with low C_b that can achieve moderately high T/D. Spacecraft with higher C_b are less affected by the storm and can survive without preemptive orbit raising provided T/D is high enough.

3.2.3 Xenon Addition

Thrust-to-power is significantly reduced for EP thrusters by running on air compared with conventional propellants such as xenon. ABEP thruster performance can be boosted when required by the addition of small amounts of xenon gas [6]. Table 3.1 shows the RIT-10 thruster performance data on air, air + 10% xenon, and 100% xenon.

Applying a linear fit to T/P and I_{sp} yields equations 3.6 and 3.7:

$$\frac{T}{P} = 17.47\chi + 13.28 \tag{3.6}$$

Percent Xe	0	10	100
T/P [mN/kW]	12.8	15.57	30.7
I_{sp}	5455	5119	3000

Table 3.1: Performance of the RIT-10 gridded ion thruster operating on an air mixture with added xenon. Data extracted from [6]. RIT-10 I_{sp} operating on 100% xenon extracted from [18].

$$I_{sp} = 5410 - 2415\chi \tag{3.7}$$

Where $\chi = \frac{\dot{N}_{Xe}}{\dot{N}-air}$ is the fraction of xenon fed to the thruster by number density. Inlet efficiency of $\eta_{in} = 0.35$ is used yielding $T/D = 1.09$ with only ABEP thrust. Equations 3.6 and 3.7 are used to compute thrust using the fitted values for I_{sp} and T/P.

As in the previous section, epoch time $t = 0$ is defined as when the IMF B_z component goes negative based on ACE spacecraft data [91]. At $t = 0$, drag free mode is switched off and performance is defined in terms of equations 3.6 and 3.7 respecting the restraint $T \leq (T/P)P_0$. For a spacecraft with length scale $d = 1$ m, 3 sccm of added xenon corresponds to 5% xenon by number flow rate at the start of the simulation. Figure 3.8 shows the impact of adding 3 sccm xenon for this spacecraft compared with only using ABEP thrust. The addition of xenon allows the spacecraft to survive the storm using a total of 152 g of xenon. G4 intensity storms occur on average 60 days per solar cycle [78]. A rough estimate for xenon usage rate for this spacecraft can be computed as 152 g of xenon per G4 storm with an average of 5.5 G4 storms per year resulting in 836 g/year of xenon. Note that geomagnetic storms occur more frequently during the solar cycle peak.

Spacecraft dynamics scale with percent xenon fraction, so a smaller or larger spacecraft have an identical response provided C_b, χ, C_d, T/P, and I_{sp} are all the same and total power available is scaled appropriately. For example, a spacecraft with $d = 10$cm (A_{in}=0.01m^2),

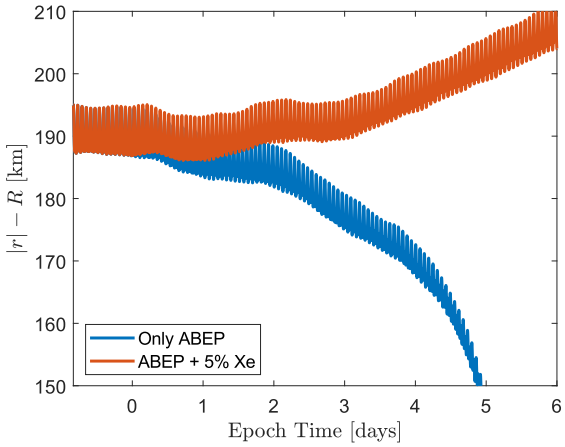

Figure 3.8: Propagated orbits for $\eta_{in} = 0.35, C_d = 4.8, C_b = 90$ kg/m^2. $t = 0$ is set to be when the IMF B_z crosses zero at 20:00:00 on November 7th 2004.

$\chi \approx 5\%$ corresponds to 0.03 sccm of xenon.

This analysis assumes that xenon remains in the thruster discharge chamber and does not diffuse to other parts of the inlet. Upstream diffusion in the inlet would result in xenon losses and higher required flow rates. High compression inlets with sufficient upstream pressure gradient should experience little xenon backflow maintaining high performance.

While xenon addition requires an increase in system complexity due to the inclusion of the xenon flow system, it can improve spacecraft survivability at a low xenon mass cost. This mitigation method is particularly useful for spacecraft with both low C_b and low T/D which cannot quickly orbit raise using ABEP alone.

3.3 Geomagnetic Storm Risk Conclusions

It has been shown that for large storms, low C_b and low T/D spacecraft are highly susceptible to geomagnetic storm risks. High C_b and high η_{in}, resulting in high T/D, reduces storm risks and can make the spacecraft robust to intense geomagnetic storms with no required mitigation. Thus risk mitigation is investigated for low C_b and low T/D spacecraft. Pre-

emptive orbit raising is shown to successfully reduce risk for spacecraft with sufficiently high T/D to quickly orbit raise ahead of a storm. Several hours of storm warning is required for this risk mitigation strategy necessitating accurate storm prediction. Xenon addition during a geomagnetic storm is shown to improve survivability for all spacecraft and is particularly useful for low T/D spacecraft which are not able to orbit raise quickly. A relatively small amount of xenon is shown to significantly improve survivability during high drag events at the cost of increased system complexity.

CHAPTER 4

RF Gridded Ion Thruster Overview

Gridded ion thrusters utilizing an inductively coupled plasma (ICP) discharge, typically called radiofrequency (RF) gridded ion thrusters, were initially developed in the 1960s [95] and have since been commercialized in a wide range of sizes [96, 97, 98, 99]. RF gridded ion thrusters utilize an inductively coupled plasma (ICP) discharge to generate a plasma and a set of biased grids to accelerate the ions to high velocity generating thrust. Commercial RF ion thrusters are available in a wide range of sizes and power levels [18, 8, 100]. As the ICP discharge does not require a thermionic emitter, RF thrusters are more robust to chemically reactive propellants. In processing applications ICP discharges are commonly operated with a wide range of gasses including N2, O2, Cl, and other reactive gasses [101]. DC discharges utilizing thermionic emitters are sensitive to oxygen poisoning which rules out propellants containing oxygen and necessitates careful handling procedures to avoid contamination [102]. RF discharges are simpler in construction than similar DC thrusters requiring fewer power supplies and no discharge cathode.

Off the shelf RF ion sources exist, but they are high cost and difficult to modify. A small lab model RF ion thruster is a useful platform for thruster experiments particularly for alternative propellant and air-breathing applications. Additionally, the high energy ion beam from the thruster can be used for investigating plasma-material interactions [103, 104]. This chapter provides a brief overview of RF ion thruster operating principles and concepts and how they apply to RF ion thruster design.

4.1 ICP Discharge Overview

RF ion thrusters utilize an inductively coupled plasma (ICP) discharge to generate plasma in the discharge chamber. Major components of an ICP are (1) the RF antenna which is driven with an AC current, (2) the discharge chamber which confines the plasma, and (3) the plasma itself as shown in Figure 4.1a. The simplest instance of the ICP discharge is a cylindrical geometry. Flat "stovetop" geometries are commonly used in processing applications as they can generate plasma in a very large area. In thruster applications, cylindrical, conical, or hemispherical geometries are most common. This paper will focus on the cylindrical geometry, but the general principles are broadly applicable.

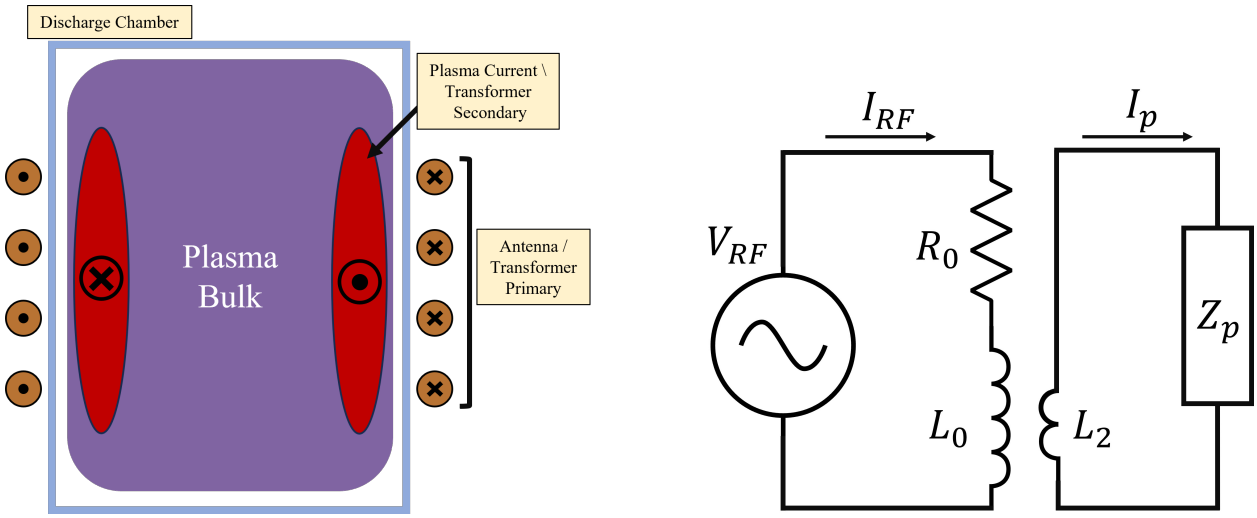

(a) Block diagram of an ICP discharge

(b) Circuit diagram of an ICP discharge

Figure 4.1: Diagram of a cylindrical ICP discharge. AC current flows through four turn antenna shown in the diagram which acts as the primary winding of a transformer. Current is induced in the plasma near the antenna forming a single turn transformer secondary. The ICP discharge is represented as a transformer in a circuit diagram [12].

An ICP can be thought of as an air core transformer with the RF antenna as the primary winding and the plasma as a single turn secondary winding [12, 101]. Assuming a plasma already present in the discharge chamber, startup will be discussed in section 4.1.2, current

in the primary induces a current in the plasma secondary. Plasma impedance Z_p contains a real part due to collisions in the plasma and an imaginary part due to electron inertia [14, 101]. Power is dissipated in the secondary due to the real part of Z_p which results in heating of the electron population to energies where ionization can be sustained, usually a few eV.

Another important power deposition mechanism for low pressure ICP discharges is stochastic heating [101, 14]. Stochastic heating is a collisionless heating method where thermal electrons are directly heated by the oscillating electric fields present at the discharge chamber walls. This effect allows for efficient ICP operation at low pressure where there are few collisions [14].

4.1.1 Capacitive Coupling

Driving RF power in the coil can induce high voltages across the antenna particularly for high inductance antennas (high number of turns). In the simplest configurations, one antenna leg is grounded while the other is at an oscillating high voltage [13]. High voltages present in the antenna can capacitively couple to the plasma depositing power to the bulk plasma [14]. Capacitive coupling is less efficient than inductive coupling as high energy ion can impact the discharge chamber walls increasing losses [15]. Capacitive coupling can be reduced through the use of a Faraday shield or through advanced match network topologies [105, 106]. A Faraday shield is a slotted metal shield placed between the antenna and the discharge chamber. The slots allow the magnetic component of the RF field to penetrate into the discharge sustaining the ICP but blocks the electric component of the RF field reducing capacitive coupling. Faraday shields are effective at reducing capacitive coupling but can add loss if poorly designed as well as increase complexity [105, 106]. Advanced match topologies rely on the use of additional capacitors in the match network to reduce voltage across the antenna coil ends as described in [106, 107].

4.1.2 Discharge Startup

Startup in a gridded RF ion thruster can be achieved in two ways, through the E-H mode transition, or if a neutralizer is present, reverse bias of the grids [108]. E-H mode transition is a simple way to start the discharge as no neutralizer is required, but in practice for gridded ion thrusters it may require higher RF power than normal and a gas puff. Puffing the gas initiates a capacitive plasma in the discharge chamber known as E mode which can be seen as a dim glow in the discharge chamber. Increasing RF power results in a transition to inductively coupled H mode with a corresponding sharp increase in brightness and change in impedance. After H mode is initiated, RF power can be decreased due to a hysteresis effect [108]. Starting using the E-H mode transition requires capacitive coupling, so inclusion of a Faraday shield can impede startup using this method [105].

Startup with a neutralizer already on can be performed by setting a positive bias on the accel grid drawing electrons from the neutralizer into the discharge chamber initiating the discharge. RF power and gas flow can be left at normal levels during this procedure reducing requirements on the RF generator and chamber pumping capacity. A DPDT switch can be used to easily switch accel grid polarity.

4.2 Antenna Matching

Antenna matching is required to effectively deliver power to the plasma. A description on how a user should approach antenna matching is provided. There are also several engineering considerations for RF ion thruster construction which can impact device operation and performance.

4.2.1 Match Network

In AC power transfer circuits, source and load impedance must be matched for effective power transfer. If there is a mismatch in the system then power is reflected from the load instead of absorbed. Load in an ICP is the combination of the antenna coil and plasma which forms a complex impedance [12]. Most commercial RF equipment has a standardized, real 50 ohm source impedance but ICPs are dynamic, complex RF loads. Therefore, insertion of an impedance matching network between the source and the load is used to transform the complex load impedance to the 50 ohm source. Several match topologies exist, but an L topology shown in Figure 4.2 is the most common [13]. Match topologies which utilize inductors can experience higher losses [106].

System impedance changes significantly with the presence of a plasma which requires the matching network to be robust to instantaneous changes in impedance between the on and off condition. A sharp rise in impedance can result in high voltages and breakdown of the matching network components. Plasma operating conditions also lead to changes in impedance that the matching network must be robust to.

Several ideal transformer models exist to estimate plasma impedance [13, 12]. Implementation of these models in practice can be difficult though due to nonideal effects in the system. An iterative approach is used to design the PCB match network. The antenna is first matched with no plasma, then the impedance is measured with the plasma on and the match network is adjusted for the plasma on condition.

The antenna with no plasma represents a complex impedance which must be matched reasonably well to the generator output to create a plasma. Antenna impedance $Z = R + Xj$ can be measured using a vector network analyzer (VNA) connected to the antenna terminals. Coupling to the environment can be significant so VNA measurements should be taken with the antenna installed in the thruster. Complex impedances can be plotted on a Smith chart [109]. Smith charts are commonly used in impedance matching where real loads exist on

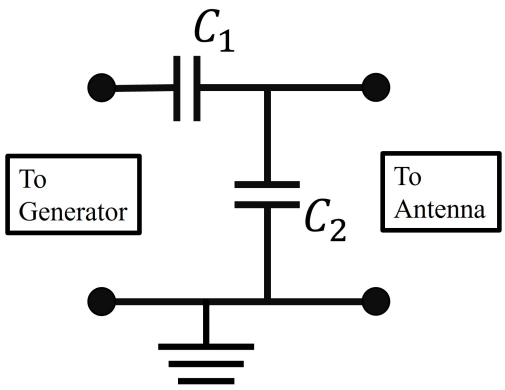

Figure 4.2: Electrical diagram of an L match network [13]. In some match networks the order of the shunt and series capacitors are swapped.

the horizontal axis, inductive loads are located above the axis, and capacitive loads are located below the axis. ICP antennas are inductive loads so are located in the top portion of the Smith chart. Several programs exist to compute the required capacitor values for the match network topology shown in Figure 4.2 [110, 111]. The match network should be shielded from the environment in a repeatable way as coupling to metal enclosures can have a significant effect on matching. Similarly, match network capacitors should be mounted in a way which minimizes changes to the circuit for consistent matching. Capacitors should be chosen such that they are rated to the driving frequency, rated to high RF voltage, and have a flat temperature response to minimize thermal effects on the match.

Once the antenna is matched with no plasma, power can be delivered to the antenna generating a plasma. With the plasma on, the match will be poor and reflected power will be high. Load impedance with the plasma on can be measured using a directional coupler inserted on the generator side of the match network and an oscilloscope connected to the forward and reflected power outputs. The forward wave has the form $V(t) = V^+ \sin(2\pi ft)$ with the reflected wave $V(t) = V^- \sin(2\pi ft + \psi)$ where ψ is the phase shift between the forward and reflected waves and V^+ and V^- are the wave amplitudes. The complex reflection coefficient Γ can be computed as: [112]

$$\Gamma = \frac{V^-}{V^+} e^{j\psi} \tag{4.1}$$

Impedance Z can then be computed from Γ using [113]:

$$Z = Z_0 \frac{1+\Gamma}{1-\Gamma} \tag{4.2}$$

Where $Z_0 = 50\ \Omega$. Additionally, the standing wave ratio (SWR), s can be computed from Γ using $s = \frac{1+|\Gamma|}{1-|\Gamma|}$. SWR can be used as a measure of how well matched a load is with SWR=1 being perfectly matched.

Commercial automatic adjustable match networks are available and can adjust a set of variable capacitors to match to a broad spectrum of load impedances. These systems are useful for laboratory experiments and development where operating conditions are expected to vary widely. Adjustable match networks are generally located outside the vacuum chamber and require a high voltage feedthrough and a feed line to the source. Long feed lines can create significant losses before reaching the antenna and transform the load impedance reducing specificity of the thruster impedance and changing system response. If a current measurement on the feed line is possible, then coupler loss can be computed as described by [106]. PCB match networks with fixed capacitors may be attractive to some users as it is more similar to a flight system and minimizes losses in the coupler at the cost of reduced flexibility and more upfront development costs.

4.2.2 Antenna Design

In practice, the antenna coil makes a non-ideal air core transformer with the plasma which can increase loss and change the electrical response of the ICP relative to an ideal transformer model [114, 115]. A physical diagram of non-ideal effects is shown in Figure 4.3a.

Major non-ideal transformer effects are leakage inductance, coupling to the thruster body, and the skin effect. These effects can result in weak coupling to the plasma and higher

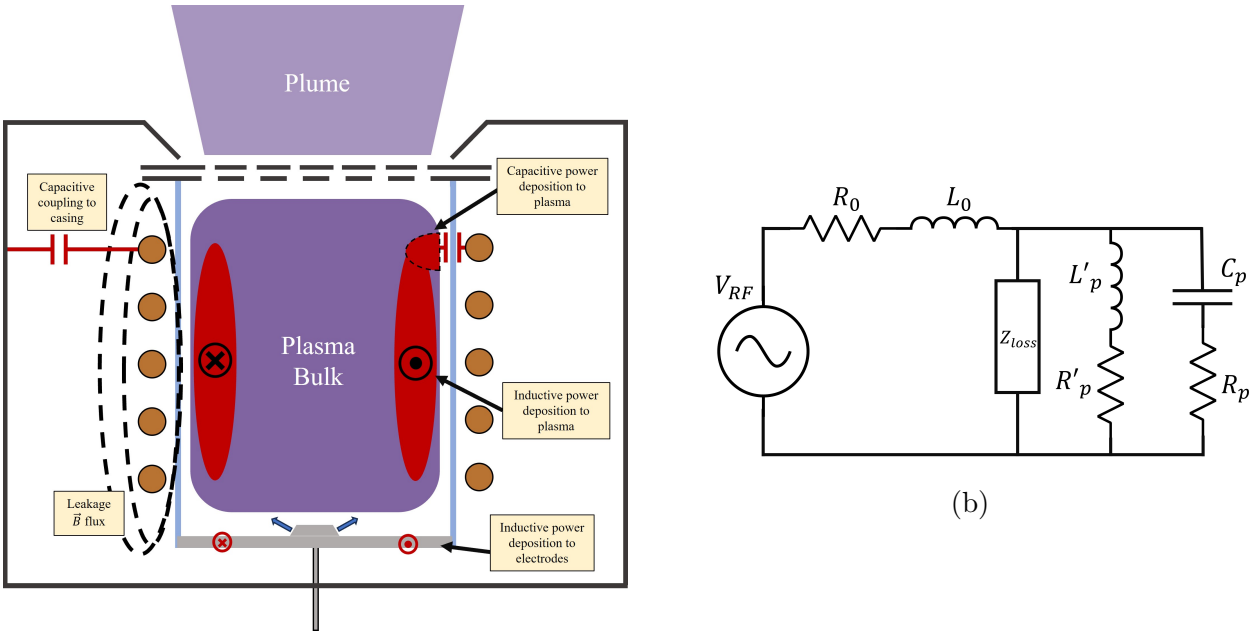

Figure 4.3: Block diagram and circuit diagram of an RF gridded ion thruster showing coupling to the plasma and loss mechanisms which can have capacitive and inductive components [14, 15].

reactance increasing losses. Leakage inductance is generated magnetic field that 'leaks' between the primary and secondary and does not contribute to current generation in the secondary [116]. In an ICP this is determined by the discharge chamber wall thickness. A thin discharge chamber increases inductive power transfer, but also increases capacitive coupling, a less efficient mechanism [106, 15]. On the opposite side of the coil to the load, the antenna can couple to the thruster casing, grids, and other metal parts near the coil. Coupling to the casing determines the minimum device size where smaller devices will have more coupling to the coil and higher loss. The skin effect causes increased coil heating by increasing wire resistance in the antenna. At high frequency current tends to travel on the surface of conductors instead of through the bulk of the material as in DC circuits reducing the effective size of the conductor.

4.2.3 RF Safety

RF systems can emit harmful levels of non-ionizing radiation if not properly shielded. OSHA recommends a voluntary maximum exposure of 10 mW/cm^2 while FCC regulations limit exposure to $900/f$ mW/cm^2 where f is the frequency in MHz [117, 118]. The American Radio Relay League provides information on safe operation of RF devices [119]. Care should always be taken to shield users from RF radiation particularly with high-power devices.

4.3 RF Thruster Overview Summary

RF gridded ion thrusters are robust devices useful for laboratory experiments for new EP devices and investigation in areas such as PMI and plasma-based manufacturing. For EP, RF ion sources are particularly attractive for alternative propellants and emerging applications such as ABEP. A review of principles of RF gridded ion thruster design is provided to increase accessibility of these thrusters to new users. These principles were applied to create a low-cost lab model thruster at the UCLA PESPL for ABEP and alternative propellant experiments as presented in the following chapter.

CHAPTER 5

PESPL RF Gridded Ion Thruster

RF gridded ion thrusters have received interest for air-breathing electric propulsion (ABEP) and multi-mode propulsion applications due to the ability of the ICP discharge to handle reactive gasses [33, 34, 17, 79]. Additionally, there is interest from the electric propulsion (EP) community in krypton and argon as low-cost propellant alternatives to xenon [35].

Krypton is a popular xenon alternative with a lower price and higher production capacity at the cost of reduced performance. Patterson and Williams conducted tests with krypton on a 30 cm DC gridded ion thruster finding increased neutral losses and a 20% reduction in total performance at the same specific impulse [120]. Scholze et al. tested the IonJet combined gridded ion thruster system with xenon and krypton [121]. Krypton propellant required higher RF power for the same beam current compared with xenon [121]. Esteves et al. simulated the Pegasus thruster using a global model on several propellants including krypton which showed reduced thrust-to-power (T/P) than xenon [122]. Argon propellant was also simulated showing a further reduction in T/P compared with krypton [122].

Air-breathing electric propulsion (ABEP) relevant propellants include N2, O2, air, and air + seed gas mixtures where the seed gas is an easily ionizable gas such as xenon [26]. Lotz presented results on a modified RIT-10 RF gridded ion thruster operating on N2, O2, and a 56% N2, 44% O2 gas mixture [6]. Thrust-to-power and specific impulse (I_{sp}) were reported to be 12.8 mN/kW and 5455 s [6, 28]. A mixture of 10% xenon, 90% air was tested resulting in a reduction in RF power and thrust increase, but no other mixture ratios were tested.

Hydrazine is a common storable monopropellant for chemical propulsion systems. Elec-

tric propulsion systems utilizing hydrazine can operate as a multimode high I_{sp} / high thrust propulsion system [37]. Additionally, chemical and electric propulsion systems operating on a common propellant can simplify orbital refueling architectures. A gridded ion thruster operating on hydrazine can achieve higher I_{sp} than an arcjet based system potentially increasing mission flexibility.

This chapter presents performance of a single RF gridded ion thruster operating on several propellants to add to the body of available data on performance scaling between propellants. Xenon is used as the baseline control propellant for comparison to other propellants. Krypton and argon are tested as low cost noble gas alternatives. N2, air, and air-xenon mixtures are tested as ABEP relevant propellants. Several air-xenon mixture ratios, with more increments at low xenon fractions, are presented to extend the dataset collected by Lotz and better resolve the influence of small amounts of xenon addition. Additionally, xenon addition as a method to achieve ignition at lower air flow rates than would be possible with air alone is demonstrated. Hydrazine is not directly tested as a propellant in this study due to its toxicity, and instead a stoichiometric mixture of N2 and H2 is used as a hydrazine surrogate.

5.1 Thruster Description

The thruster used in this study is a 3 cm RF gridded ion thruster developed at PESPL [17]. Thruster design was influenced by commercial miniature RF gridded ion thruster designs such as BIT-3, NPT30-I2, and RIT-4, as well as taking heritage from the 3 cm MiXI DC discharge thruster [96, 97, 98, 123].

A CAD model of the thruster with major components labeled is shown as Figure 5.1a. Unique features of the thruster include a dedicated anode and a floating screen grid [124]. A dedicated anode was chosen for additional electrical contact to the plasma, reduced grid recycle impact, simplified gas distribution, and to provide a replaceable electrode for materials studies.

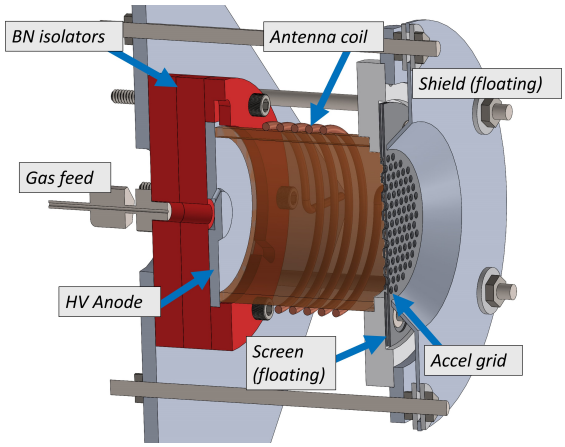

(a) Design model of the thruster head.

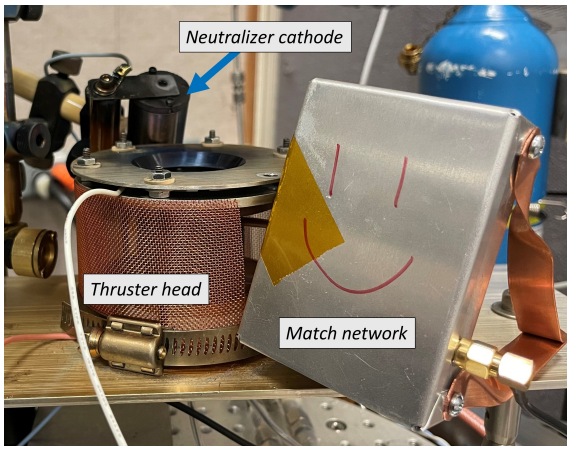

(b) Assembled thruster in the vacuum chamber.

Figure 5.1: CAD model of the thruster showing major components and photo of the thruster in the vacuum chamber showing the match network box and neutralizer cathode.

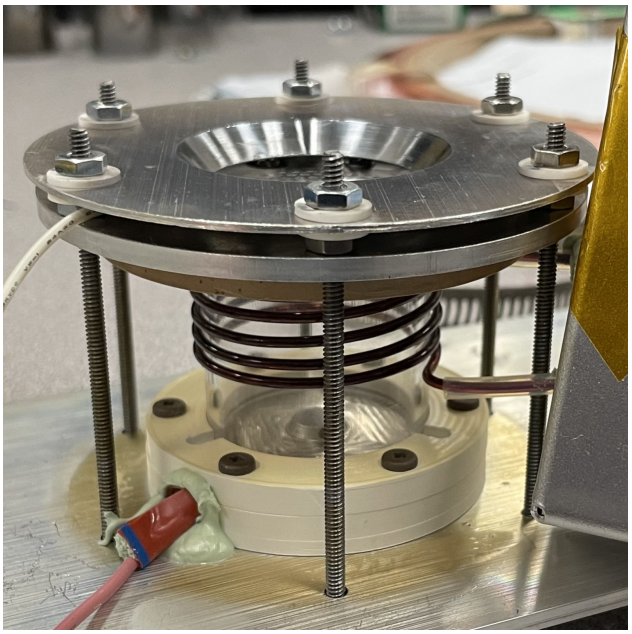

Figure 5.2: Photo of the thruster with the Faraday shield removed.

Figure 5.2 shows the thruster with the Faraday shield removed revealing the antenna and thruster internals. PEEK screws are shown in this photo which were later replaced with

steel due to heating issues. An additional 0.25 inch BN isolator was added under the HV anode to better isolate the plasma from the gas feed line. Ceramic washers are used to isolate the floating shield. Insulating paste is used to shield the HV anode electrical connection to prevent unwanted arcing and corona discharges.

The grid face is 3 cm in diameter with the same ion optics as the MiXI gridded ion thruster [123]. Precise grid spacing is achieved using metal shim washers placed in oversized cutouts in the screen grid to avoid electrical contact between the grids. The floating shield located downstream of the grids blocks the exposed screen grid mounts from the neutralizer so there is no direct current path from the neutralizer to the anode through the discharge and discourages neutralizer coupling to facility ground [125]. A Macor grid mount holds the grid assembly and interfaces with the discharge chamber. A 35 mm long quartz tube with a 32 mm inner diameter and 36mm outer diameter is used as the discharge chamber. The clear discharge chamber allows easy access for optical diagnostics. At the upstream end of the discharge chamber is the high voltage (HV) anode which also serves to distribute gas in the discharge chamber. The discharge chamber tube is held in place between the grid assembly and the anode by threaded tension rods. Angled holes drilled in the anode divert propellant gas away from the grid face reducing neutral losses [98]. The gas feed connection is left floating to eliminate any current paths through the gas feed. Boron nitride is used for the base construction material shown in red due to its machinability and high temperature tolerance. A 5-turn antenna coil is wrapped around the discharge chamber. The antenna is made of 14 AWG magnet wire.

A circuit diagram of the thruster and cathode electrical system is given as Figure 5.3 showing all power supplies.

Two DC power supplies are used for the thruster, the beam supply and the accel grid supply. Beam voltage, V_b, is connected to the high voltage (HV) anode biasing the plasma discharge to the beam voltage. A PCB match network shown in Figure 5.4 is used to match the thruster to the 50 Ohm RF source providing a VSWR of roughly 3:1 for most operating

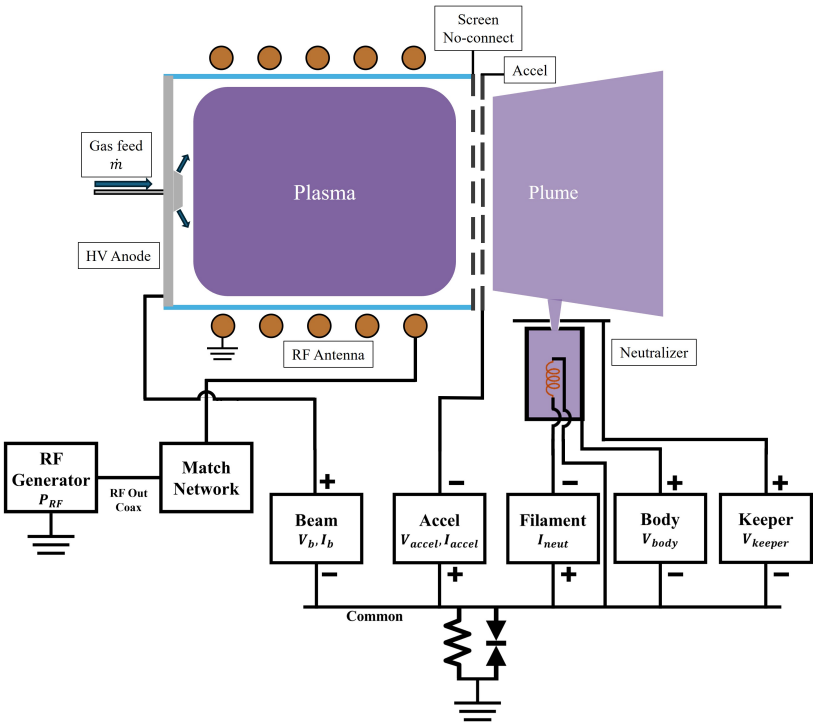

Figure 5.3: Block Diagram of the thruster showing connections with all power supplies.

conditions. High frequency, high voltage capacitors with a NP0 temperature coefficient are used in the match network. Insulating thermal compound is used to heat sink the match network to the case and eliminate arcing at the exposed solder pads.

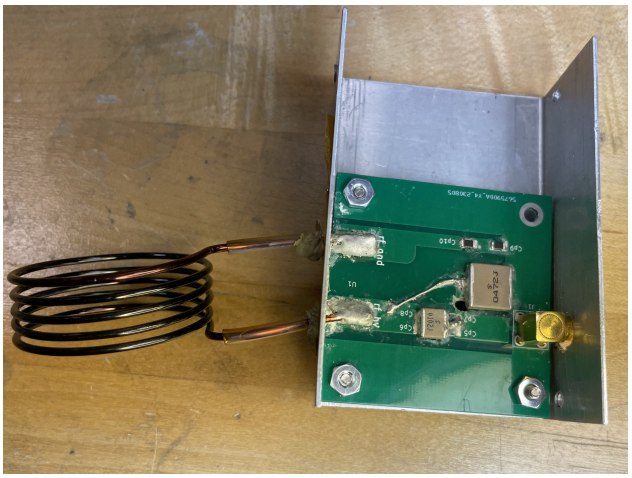

Figure 5.4: Photo of the antenna and fixed capacitor match network with the cover removed. RF power is delivered via a 50 Ohm SMA connector.

Discharge startup is achieved by first starting the neutralizer and then applying a reverse bias to the accel grid drawing electrons into the discharge chamber and starting the ICP discharge. A DPDT switch can be used to quickly flip the polarity of the accel grid. RF power and gas flow rate are set at the desired setpoint when starting. Beam voltage is applied to the anode (1000 V for the results discussed in this publication), and the accel grid is set at the nominal operating voltage (-250 V for the results discussed in this publication). The accel grid is then quickly flipped positive and then back to negative. If the discharge does not ignite, RF power is increased and the process is repeated until ignition occours.

5.1.1 Neutralizer

A shielded filament cathode is used as the neutralizer [16]. A CAD model of the cathode is shown in Figure 5.5. The cathode contains a tungsten filament contained within a 1-inch diameter cylindrical steel housing and a downstream steel keeper electrode. Argon is used as the working gas for the cathode. Current is driven through the filament heating it to thermionic emission temperatures. The cathode body is then biased to 25 V accelerating electrons from the filament through the argon gas ionizing it. Then, the keeper is biased to

85 V drawing the plasma out of the cathode body and collecting current. After the keeper begins drawing current, the cathode body power supply is shut off allowing the body to float. During nominal operation, the keeper collects 0.3 - 0.4 A of current with 3 sccm of argon gas feed. A shielded filament cathode more closely matches operational geometry for a hollow or RF cathode and allows for better observation of the plume than an unshielded filament. Continuing efforts are underway to integrate a RF cathode.

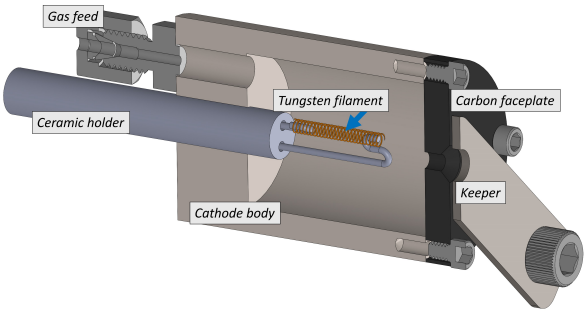

Figure 5.5: Cutaway CAD model of the shielded filament cathode showing major components [16].

5.2 Methods

Experiments were conducted in the UCLA PESPL bell jar chamber [123]. The chamber is 20 inches in diameter, 36 inches tall, and is pumped by a CT-8 cryopump. Base pressure is 3 x 10^{-7} Torr and operating pressure is 2 x 10^{-4} Torr. Figure 5.6a shows the vacuum chamber setup with the power supply rack next to it. A Glassman series EQ 3 kV DC high voltage supply is used as the beam supply. A Sorensen DLM 300-2 is used for the accel supply. Sorensen DLM series power supplies are used for the cathode DC supplies as well. An Electronics & Innovation 1020L 10 kHz – 5MHz broadband power amplifier operated at 2.2 MHz was used to power the RF discharge. RF power is fed into the vacuum chamber to the match network SMA connector via LMR100 coaxial cables. A power loss of 5.5% was measured along the RF coaxial lines using a VNA. A directional coupler is placed near the

match network input to measure forward and reflected voltage waveforms.



(a) Facilities and power supply rack setup.



(b) Multi-gas feed system.

Figure 5.6: A photo of the full vacuum chamber setup with the power supply rack, and a closeup photo of the gas mixture flow manifold set up for noble gasses.

Figure 5.6b shows the flow manifold used to feed propellant to the thruster. The manifold is capable of mixing up to three gases and is based on a design published by Lotz (2013) [6]. 20 sccm range N2 calibrated mass flow controllers (MFCs) from Apex Vacuum are used for the flow manifold.

Thruster performance is computed using the measured parameters: total propellant feed rate, RF forward $P_{forward}$ and reflected $P_{reflected}$ power measured at the generator, and beam current I_b measured at the beam power supply. Propellant feed rate $\dot{m}$ is a combination of gas fed through he MFC and gas ingested due to facility background pressure. Gas ingestion is taken into account using a Clausing factor, η_c, and all ingested flow is assumed to be argon

from the neutralizer cathode. Total mass flow delivered to the thruster in kg/s is given by equation 5.1:

$$\dot{m} = \sum_k \dot{N}_k M_k + \frac{n_0 \bar{c}_{Ar}}{4} A_{open} \eta_c M_{Ar} \tag{5.1}$$

Where $\dot{N}_k$ is the particle flow rate in atoms per second, M_k is the mass of the species, and all inputted species are summed over. Chamber neutral density, computed from the chamber operating pressure, is n_0, A_{open} is the open area of the grid face, $\bar{c}_{Ar}$ is the thermal velocity of the neutrals given by $\bar{c} = \sqrt{\frac{8k_BT}{\pi m}}$. The Clausing factor, η_c, is determined to be 0.7 for the grid geometry using the aspect ratio of the circular grid holes [126, 127, 51, 52].

RF power towards and reflected from the thruster is derated by the coaxial cable loss $L = 0.055$, so the total delivered RF power is given as equation 5.2. Primary performance metrics are discharge loss η_d, electrical η_e, mass η_m, and total efficiency η_t, thrust T, I_{sp}, and thrust-to-power (T/P) given by equations 5.3 to 5.9, respectively.

$$P_{RF} = P_{forward}(1 - L) - P_{reflected}(1 + L) \tag{5.2}$$

$$\eta_d = \frac{P_{RF}}{I_b} \tag{5.3}$$

$$\eta_e = \frac{I_b V_b}{I_b V_b + P_{RF}} \tag{5.4}$$

$$\eta_m = \frac{\sum_k I_{b,k} M_k}{e\dot{m}} \tag{5.5}$$

$$\eta_t = \eta_m \eta_e \tag{5.6}$$

$$T = \sum_k \sqrt{\frac{2M_k}{e}} I_{b,k} \sqrt{V_b} \tag{5.7}$$

$$I_{sp} = \frac{T}{9.81\dot{m}} \tag{5.8}$$

$$T/P = \frac{T}{V_b I_b + P_{RF}} \tag{5.9}$$

Equations 5.5 through 5.9 require on knowledge of beam composition for the summations. Beam composition for multispecies plasmas is estimated through the use of the global model described in appendix A which provides the percent composition of each species extracted in the beam. Currently oxygen is neglected from the global model, so air experimental results rely on the nitrogen model. Improved models and experimental plume diagnostics such as an ExB probe can improve results accuracy. Performance stated is only thruster head performance which does not take into account power supply inefficiencies or neutralizer cathode losses. Future standalone cathode tests and thruster-cathode system experiments can inform total system performance. The presented analysis neglects double ion and plume divergence losses. Plume diagnostics such as Faraday and ExB probes can provide values for these losses. Neutral ingestion is assumed to be an additional mass flow to the thruster.

5.3 Results

Thruster performance is presented for xenon, krypton, argon, diatomic nitrogen (N_2), air (78% N2 + 21% O2), air-xenon mixtures, and a $N_2 + 2H_2$ mixture representative of hydrazine (N_2H_4). Thruster operation on helium and hydrogen was attempted but was not successful.

5.3.1 Noble Gasses: Xenon, Krypton, Argon

Xenon, krypton, and argon are popular propellants for EP due to their relatively high mass, low reactivity, and large ionization cross sections. Xenon is the most common EP propellant, and in this study is used to baseline other propellants. Krypton is a common xenon alternative with slightly lower performance, but offering higher I_{sp} and lower cost than xenon. Argon propellant is commonly used as a low cost propellant for thruster development, and recently has been implemented at scale for the Starlink constellation [128]. Images of the PESPL RF gridded ion thruster running on xenon, krypton, and argon are shown as Figure 5.7.

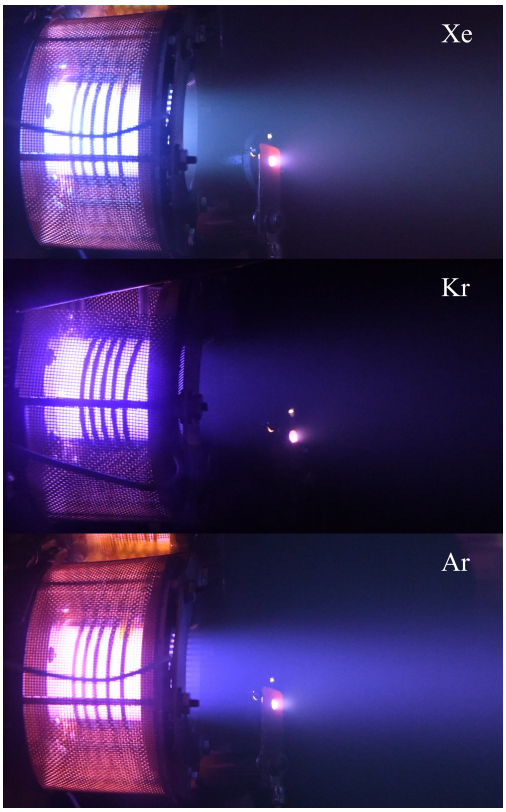

Figure 5.7: Composite image of the PESPL RF gridded ion thruster running on noble gas propellants. From top down, the propellants are: xenon, krypton, and argon.

Thruster total efficiency and discharge loss plots for xenon, krypton, and argon are

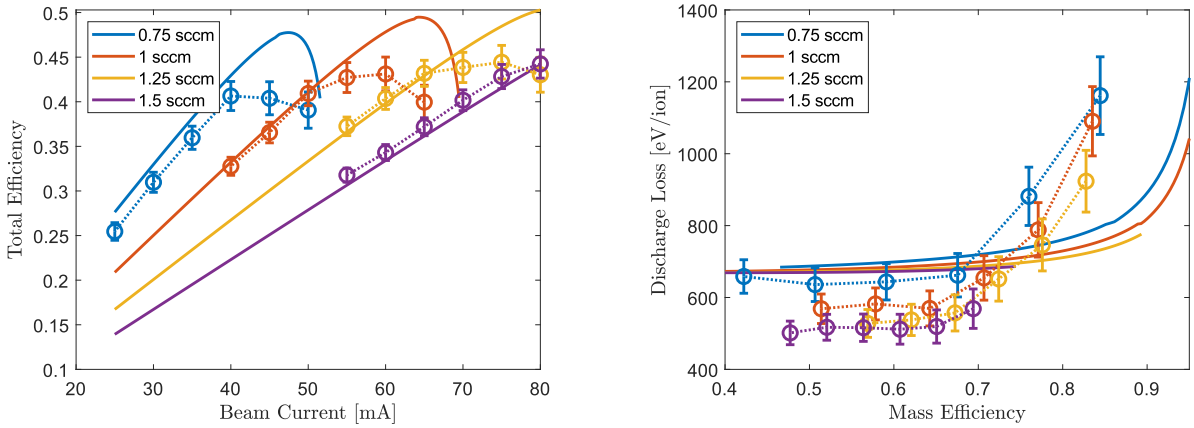

(a) Total efficiency

(b) Discharge loss

Figure 5.8: Thruster performance running on xenon propellant.

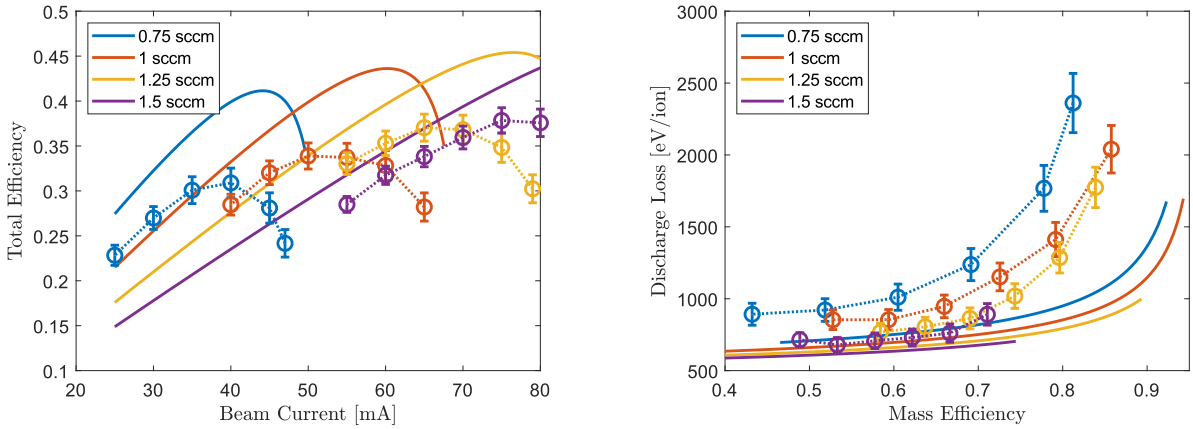

(a) Total efficiency

(b) Discharge loss

Figure 5.9: Thruster performance running on krypton propellant.

shown in Figures 5.8 to 5.10. For xenon propellant maximum total efficiency is about 44%. Maximum thrust is estimated to be 4 mN, and maximum I_{sp} is about 3400 s. Xenon performance is comparable to similarly sized thrusters including MiXI and BRFIT-3 [123, 96]. For krypton propellant maximum total efficiency is about 38%. Maximum thrust is estimated to be 3.3 mN, and maximum I_{sp} is about 4200 s. For argon propellant maximum total

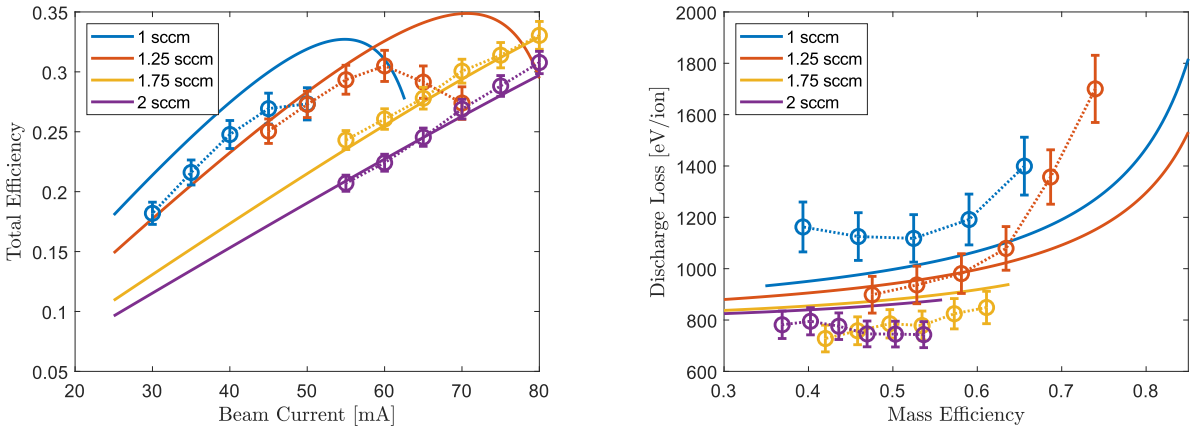

(a) Total efficiency

(b) Discharge loss

Figure 5.10: Thruster performance running on argon propellant.

efficiency is about 33%. Maximum thrust is estimated to be 2.3 mN, and maximum I_{sp} is about 5200 s. Total power usage is between 41 W at low beam currents with xenon and 190 W at high beam currents with argon.

5.3.2 Nitrogen Based Propellants: Molecular Nitrogen, Air, N2 + 2H2

Nitrogen based propellants tested in this study include molecular nitrogen (N_2), air (78% N2 + 21% O2), and a hydrazine surrogate mixture (N_2 + $2H_2$). Thruster performance on air propellant is important for ABEP applications and mission studies. At altitudes relevant to ABEP applications, the percent composition of oxygen is higher than at the ground, but the natural air mixture at the ground was deemed acceptable for this study. Comparing thruster operation with molecular nitrogen to air is useful for determining the contribution of oxygen to thruster performance. Due to the toxicity of hydrazine, a stoichiometric mixture of molecular nitrogen and molecular hydrogen is used as a surrogate. Hydrazine is a common storable propellant used in hypergolic thrusters, and may be useful for multi-mode propulsion architectures [37]. Images of the PESPL RF gridded ion thruster running on molecular nitrogen, air, and N_2 + $2H_2$ are shown as Figure 5.11.

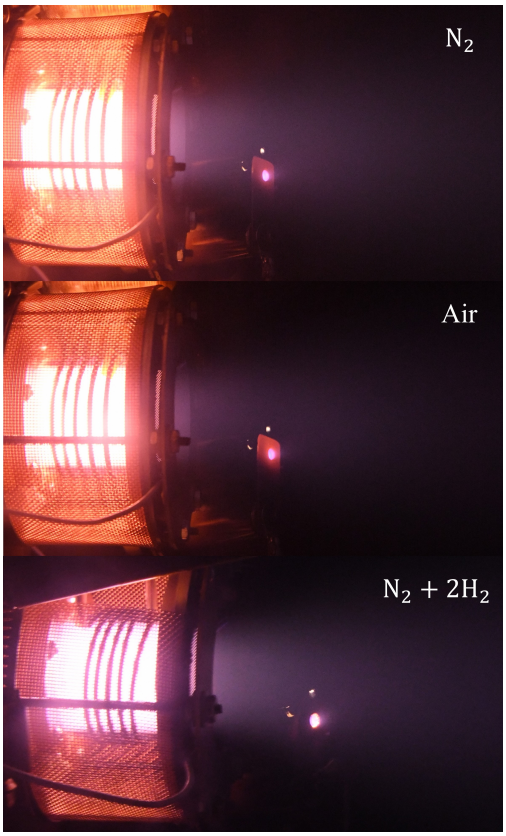

Figure 5.11: Composite image of the PESPL RF gridded ion thruster running on nitrogen based propellants. From top down, the propellants are: N_2, air (78% N2 + 21% O2), and $N_2 + 2H_2$.

Thruster total efficiency and discharge loss plots for molecular nitrogen, air, and $N_2 + 2H_2$ are shown in figures 5.12 to 5.14. A coupling coefficient of 0.5 is applied to the RF power for the modeled results to better match experimental data. Data analysis relies on the global model presented in appendix A.2 to compute the beam composition. For air and $N_2 + 2H_2$, the molecular nitrogen global model is used as well. This has the effect of assuming that the extracted beam is entirely composed of N^+ and N_2^+. Oxygen has a similar mass to nitrogen, so this assumption likely has a small effect on the calculated performance for the air test case. Assuming the extracted beam is entirely composed of N^+ and N_2^+ likely has a larger impact on calculated performance for the $N_2 + 2H_2$ case due to the large mass difference

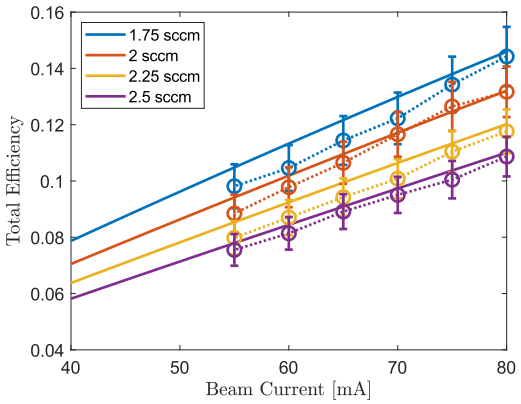

(a) Total efficiency

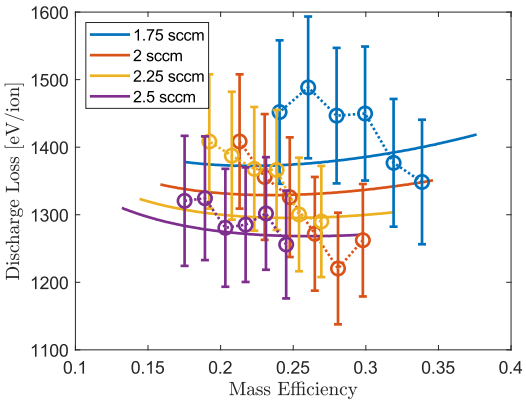

(b) Discharge loss

Figure 5.12: Thruster performance running on molecular nitrogen (N_2) propellant.

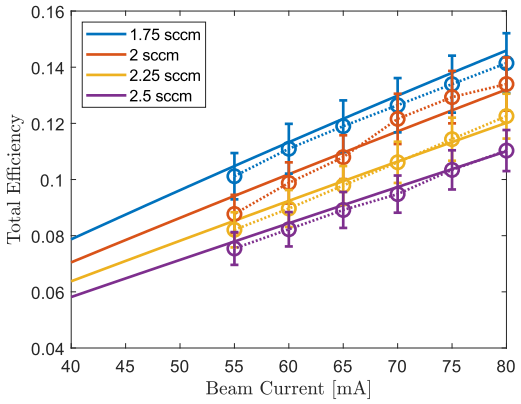

(a) Total efficiency

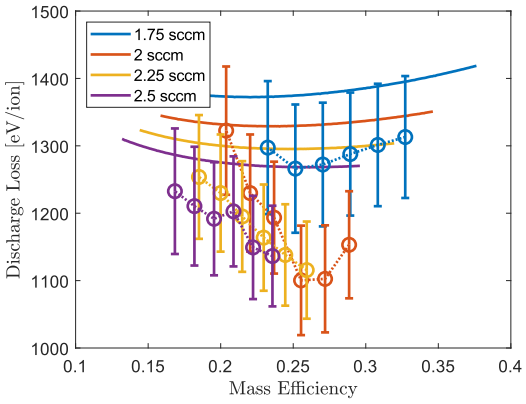

(b) Discharge loss

Figure 5.13: Thruster performance running on air (78% N2 + 21% O2) propellant.

between nitrogen and hydrogen. Improvements to the global model to include hydrogen would improve accuracy for the N_2 + $2H_2$ propellant.

For molecular nitrogen propellant maximum total efficiency is about 14%. Maximum thrust is estimated to be 1.4 mN, and maximum I_{sp} is about 3800 s. Performance on air propellant is similar to nitrogen with a maximum total efficiency of about 14%, maximum thrust of 1.4 mN, and maximum I_{sp} is about 3700 s. Nitrogen and air performance are similar

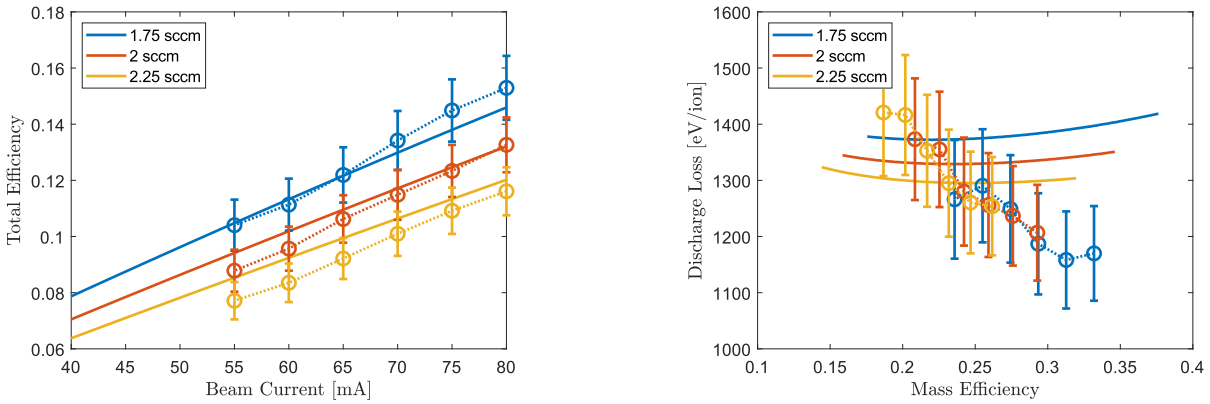

(a) Total efficiency

(b) Discharge loss

Figure 5.14: Thruster performance running on N2 + 2H2 propellant.

to measurements collected from an ABEP RIT-10 thruster [6]. For N2 + 2H2 propellant maximum total efficiency is about 15%. Maximum thrust is estimated to be 1.4 mN, and maximum I_{sp} is about 3700 s. Total power usage is between 120 W at low beam currents and 190 W at high beam currents.

5.3.3 Thruster Performance Comparison

Thruster performance parameters for each propellant option at 70 mA beam current are shown in table 5.1. $\dot{N}$ is the propellant particle feed rate in sccm. Beam voltage for all presented cases in this work is fixed at 1000 V. Thruster performance only takes into account the thruster head neglecting cathode and power supply losses. Neutral ingestion is computed using the chamber background pressure and a grid Clausing factor. Ingested flow is assumed to be 100% argon from the filament cathode. Thrust for all of the nitrogen based propellants is computed to be the same value because beam composition is assumed to only be N^+ and N_2^+.

Total efficiency decreases going from xenon to lighter noble gasses, and then falls off sharply for the nitrogen based propellants. Low total efficiency I_{sp} for nitrogen based pro-

Propellant	$\dot{N}$ [sccm]	P_{RF} [W]	η_m	η_e	η_t	I_{sp} [s]	T [mN]	T/P [mN/kW]
Xe	1.25	45.6	0.72	0.61	0.44	2904	3.56	30.8
Kr	1.25	71.3	0.74	0.50	0.37	3682	2.88	20.4
Ar	1.75	54.5	0.53	0.56	0.30	3787	2.01	16.2
N_2	1.75	101.5	0.30	0.41	0.12	3339	1.26	7.3
Air	1.75	90.1	0.29	0.44	0.13	3226	1.26	7.9
$N_2 + 2H_2$	1.75	83.1	0.29	0.46	0.13	3272	1.26	8.2

Table 5.1: Thruster performance at 70 mA beam current. $V_b = 1000$ V. Total power usage for 70 mA beam current can be computed as $P_{RF} + 70$ W. Thruster performance is only computed for the thruster head and neglects cathode and power supply losses. Neutral ingestion is accounted for via a Clausing factor.

pellants is largely due to low mass utilization driven by propellant dissociation. Minimum gas feed for thruster ignition on all nitrogen based propellants is 1.75 sccm. The global model estimates that most of this propellant dissociates within the discharge chamber. If all the propellant dissociates, then the effective flow rate is 3.5 sccm of nitrogen atoms. To achieve $\eta_m = 0.5$, the thruster would need to extract $I_b = 125$ mA with the same 1.75 sccm gas input. In order to improve thruster performance on nitrogen based propellants, the thruster should be made to extract higher beam currents or be made to ignite at lower flow rates. Current grid design is limited to 80 mA, but new grid designs may enable higher current density. Advanced ignition methods may enable lower flow rate ignition.

RF power coupling for nitrogen based propellants is estimated to be low based on global model results. RF power coupling is reduced at high electron temperatures due to a decrease in the sheath length. Improvements to RF power coupling would decrease RF power requirements improving η_e.

5.3.4 Air-Xenon Mixtures

Air-xenon mixtures are investigated for increasing thrust-to-power (T/P) of the thruster. The thruster was run at a fixed air flow rate and increasing amounts of xenon were added to the propellant feed.

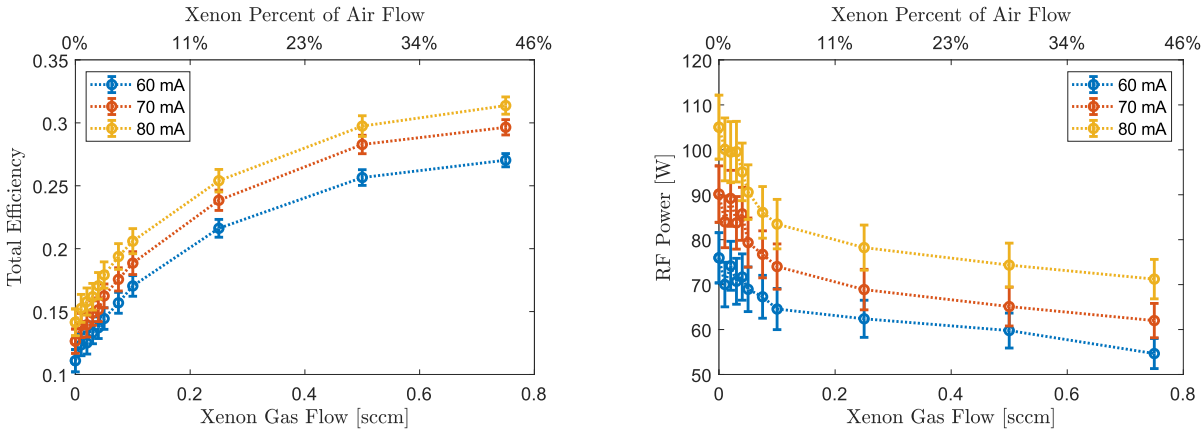

(a) Total efficiency

(b) Delivered RF power

Figure 5.15: Thruster performance running on an air-xe mixture. Air flow rate is a constant 1.75 sccm.

Figure 5.15 shows performance data for air-xe mixtures operating at fixed beam currents. A fixed 1.75 sccm air feed rate is used and xenon is added to the mixture. It can be see that RF power requirements fall off sharply at low xenon feed rates and then decreasing returns are realized for increasing xenon addition. T/P increases from 8 mN/kW with no xenon flow to 21 mN/kW with 0.75 sccm xenon flow. Thus xenon addition can be used to increase T/P to a level where ABEP operation is viable [10]. Xenon addition can also be used to operate the thruster on lower air flow rates than possible on only air. The thruster was ignited on 1 sccm of air flow with 0.075 sccm of xenon added whereas the minimum air flow rate for ignition on pure air was 1.75 sccm. Figure 5.16 shows thruster performance with 1.00 sccm of air flow.

Thrust-to-power (T/P) is compared for each case and showed as figure 5.17. T/P in-

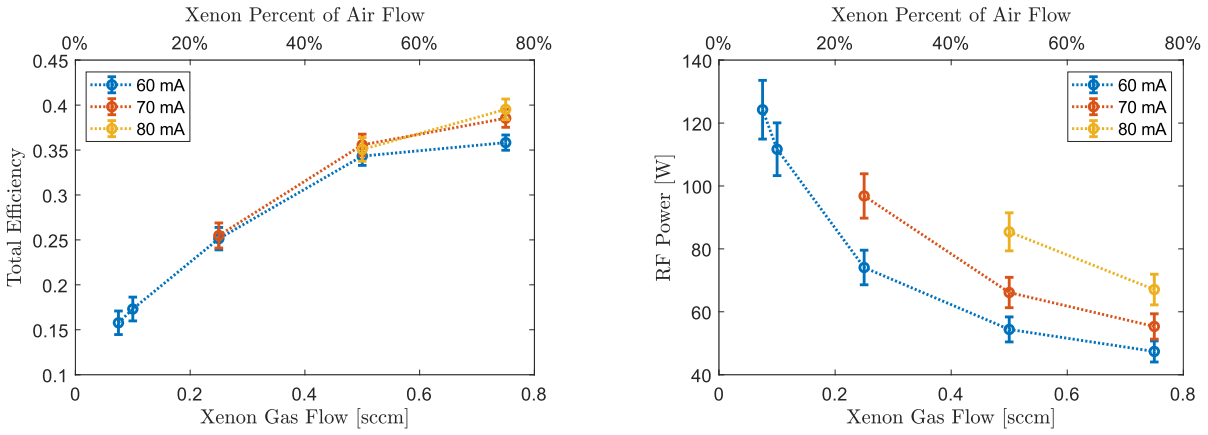

(a) Total efficiency

(b) Delivered RF power

Figure 5.16: Thruster performance running on an air-xe mixture. Air flow rate is a constant 1.00 sccm.

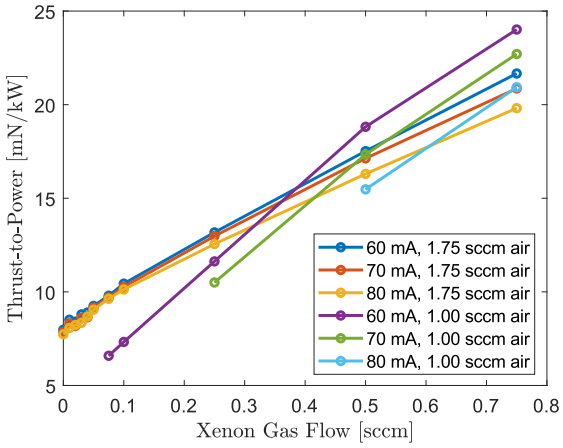

Figure 5.17: T/P for the 1.75 sccm air flow case and the 1.00 sccm air flow case.

creases linearly for both flow conditions with the 1.00 sccm case having a steeper slope. Larger performance gains are made with the 1.00 sccm case because there is less air present to contribute to losses. I_{sp} is shown for both flow cases using equation 5.8 where $\dot{m}$ is the total mass flow rate delivered to the thruster.

For ABEP applications, it may be useful to define a system specific impulse, $I_{sp,sys}$, which

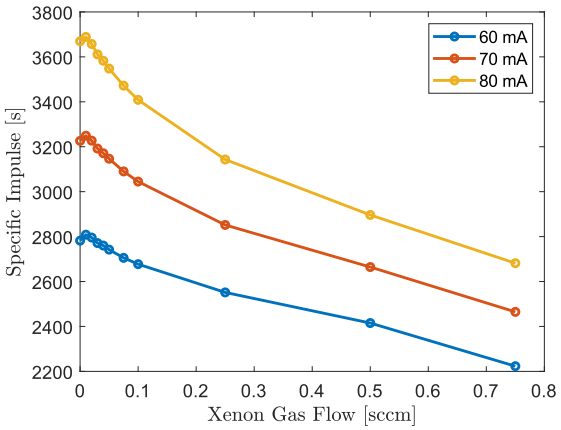

(a) 1.75 sccm air flow

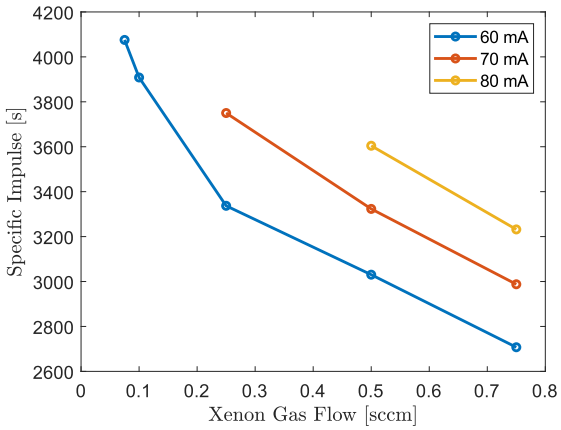

(b) 1.00 sccm air flow

Figure 5.18: Thruster specific impulse for air-xenon mixtures.

uses the mass flow rate of the onboard propellant, in this case xenon, instead of the total mass flow rate to the thruster, similar to how I_{sp} is defined for air breathing aircraft engines.

$$I_{sp,sys} \equiv \frac{T}{9.81 * \dot{m}_{ob}} \tag{5.10}$$

$\dot{m}_{ob}$ is the mass flow rate of the onboard propellant. For a fully air breathing system with no added propellant $I_{sp,sys} \rightarrow \infty$.

Figure 5.19 shows the system specific impulse of the PESPL RF ion thruster. Very high $I_{sp,sys}$ can be realized for ABEP spacecraft with xenon addition allowing for very efficient use of onboard propellant increasing spacecraft maneuverability.

5.3.4.1 Air-xenon Mixture Model Insights

The global model described in appendix A can be used to estimate the extracted beam composition for air-xenon mixtures as well as plasma conditions inside the discharge chamber. Figure 5.20 shows the composition of the extracted beam for the 1.75 sccm air flow and 1.00 sccm air flow cases.

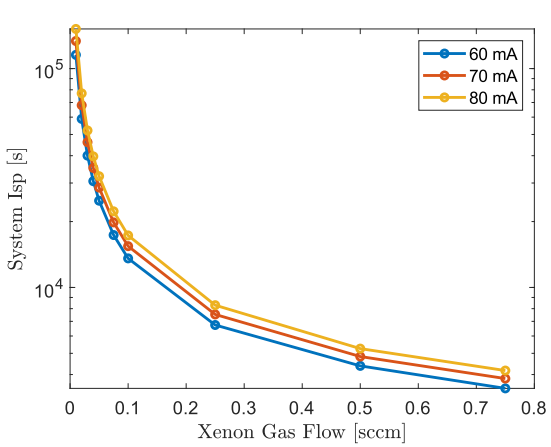

(a) 1.75 sccm air flow

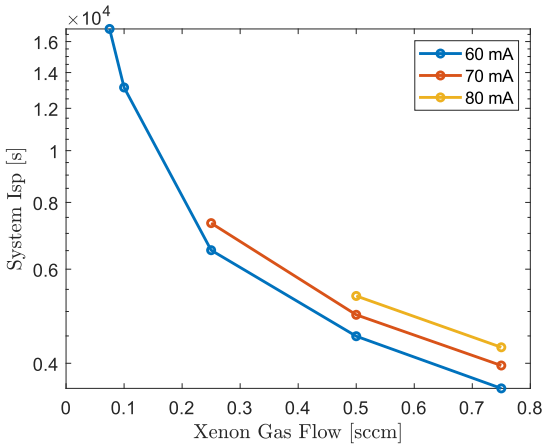

(b) 1.00 sccm air flow

Figure 5.19: System specific impulse for air-xenon mixtures.

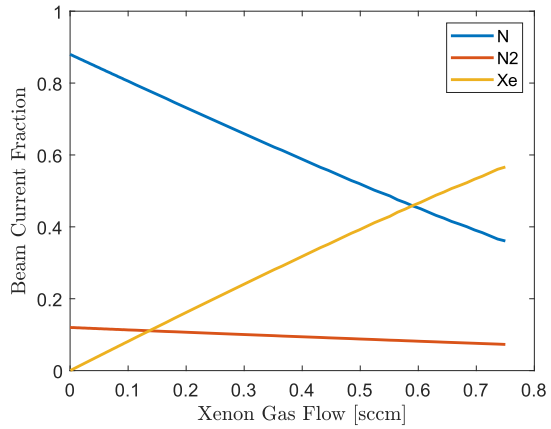

(a) 1.75 sccm air flow

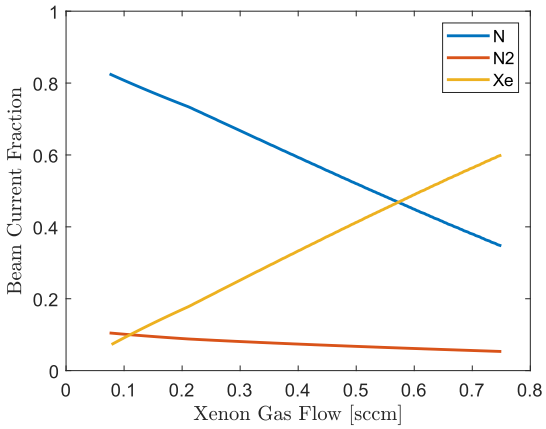

(b) 1.00 sccm air flow

Figure 5.20: Extracted beam composition at 80 mA computed using the global model.

As xenon flow rate is increased, the percentage of xenon ions in the beam linearly increases, with a linear decrease in nitrogen ions. Molecular nitrogen ion percentage remains roughly constant.

Figure 5.21 shows the plasma species composition in the thruster discharge chamber for the 1.75 sccm air flow and 1.00 sccm air flow cases. With increasing xenon flow rate, xenon

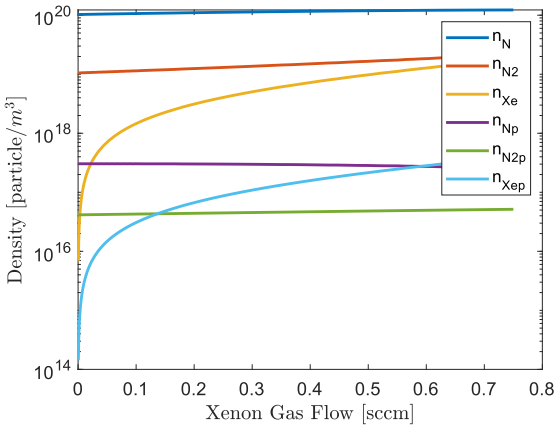

(a) 1.75 sccm air flow

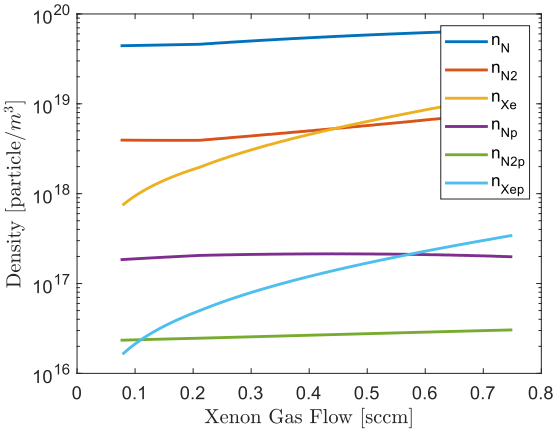

(b) 1.00 sccm air flow

Figure 5.21: Plasma composition inside the discharge chamber at 80 mA computed using the global model.

ions in the discharge rapidly increases at low xenon flow rates, and then increases linearly at higher xenon flow rates.

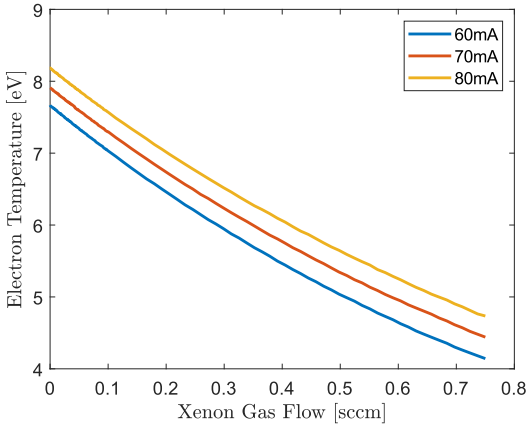

(a) 1.75 sccm air flow

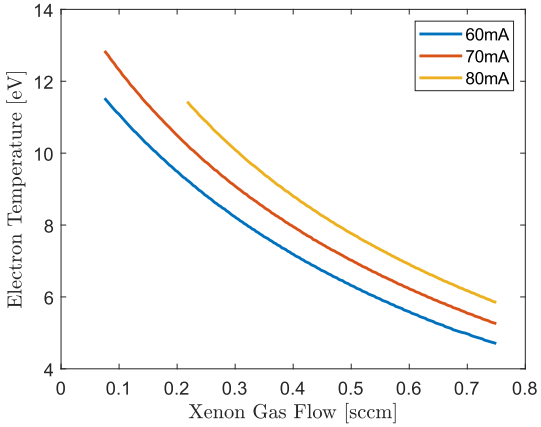

(b) 1.00 sccm air flow

Figure 5.22: Electron temperature in the discharge computed using the global model.

Figure 5.22 shows the electron temperature inside the plasma discharge from the global model. A high electron temperature at low xenon flow rates results in high discharge loss.

Increasing xenon flow rates decreases electron temperature. Future experiments will employ optical diagnostics to experimentally measure the electron temperature and species density within the plasma discharge. An ExB probe in the plume can measure extracted beam composition.

5.3.5 Helium and Hydrogen

Thruster ignition was achieved with helium, but sustained operation was not possible due to cryopumps not being able to pump helium. Users attempting to operate on helium propellant should use turbopumps. Ignition on hydrogen gas was not achieved at any flow rate. Ignition was achieved with a H2-Xe mixture, but the discharge extinguished when xenon flow was removed.

5.4 PESPL Thruster Testing Conclusions

The PESPL 3 cm RF gridded ion thruster was run on xenon and several alternative propellants including air and a hydrazine surrogate. By operating the same thruster on several propellants, direct comparisons can be made between propellants. A global model presented in appendix A is used to support experimental measurements and predict extracted beam composition for dissociative propellants and gas mixtures. Nitrogen based propellants are predicted to be highly dissociated in agreement with previous global models [129].

Air-xenon mixtures were tested experimentally showing significant decreases in RF power requirements for low xenon flow rates. Through xenon addition, thruster performance can be brought to a level where it becomes viable for ABEP applications [10]. Thruster ignition and operation was achieved at lower air flow rates with the addition of low xenon flow rates. ABEP architectures utilizing air-xenon mixtures may be able to operate at higher altitudes than pure ABEP systems increasing mission flexibility and reducing risk [130].

Future research efforts should focus on measuring the extracted beam composition, ex-

tending the global model to include oxygen and hydrogen, and accurately determining the RF coupling coefficient. These efforts would increase understanding of thruster operating conditions and improve the accuracy of measured performance values.

CHAPTER 6

Thruster Materials Compatibility

ABEP and molecular propellant thrusters operate with highly reactive plasmas which can degrade thruster performance and reduce thruster lifetime. In gridded ion thrusters, Hall-effect thrusters, and cathodes, electrode integrity can be degraded by the presence of a reactive plasma in the device.

Tejeda and Knoll investigated anode material compatibility for an oxygen Hall thruster finding that stainless steel works well at low power [131]. A tungsten anode was tested as well, but showed poor oxygen resistance. The tungsten anode formed an oxidation layer after 20 minutes of operation which degraded thruster performance [131]. Tejeda et al. operated a water electrolysis Hall thruster (WET-HET) on oxygen with a stainless steel anode and a hydrogen fed lanthanum hexaboride (LaB6) hollow cathode running on hydrogen [36]. Anode oxidation was found to be accelerated compared with previous tests due to the prescience of hydrogen from the cathode [36]. Oxidation was observed on the hollow cathode as well, but performance did not noticeably degrade over the duration of the test [36]. Cifali et al. tested a PPS1350-TSD HET on a nitrogen-oxygen mixture observing rust on the stainless steel anode [33, 34]. Thruster operation on pure oxygen was not performed due to oxidation concerns [33, 34]. A long duration thruster test was performed where the PPS1350-TSD HET was run for 300 hours before failure due to anode oxidation [28].

A modified RIT-10 RF gridded ion thruster was run on pure oxygen as well as an air mixture [33, 34, 6]. High grid erosion on oxygen propellant was seen with the standard graphite grids due to chemical etching of the grid material by oxygen. The grid was replaced

with a titanium grid set which was run for 500 hours with no noticeable degradation of performance or erosion [6]. A molybdenum screen grid was used in these tests [6].

Tisaev et al. observed molybdenum erosion and oxidation in the AMPCAT microwave cathode running on air [132]. AMPCAT uses a molybdenum microwave antenna in contact with the plasma to generate the discharge. High electric fields at the antenna caused physical sputtering of the antenna via ion bombardment [132]. Sputtered molybdenum redeposited inside the cathode forming a layer of non-conductive molybdenum oxide [132]. Coating the antenna in alumina eliminated physical sputtering and no noticeable layer was formed inside the cathode discharge chamber [132]. Reactions with the stainless steel cathode discharge chamber after coating the microwave antenna were not investigated.

Based on existing literature, titanium and stainless steel have been identified as potential high-performing materials for ABEP and other reactive propellants. Experiments are performed to further investigate these materials and probe surface chemistry processes due to reactive nitrogen and air plasmas. X-ray photoelectron spectroscopy (XPS), scanning electron microscopy (SEM), and energy-dispersive X-ray spectroscopy (EDS) are commonly used surface analysis techniques which are employed in this work to characterize material surface layers.

6.1 Test Setup

Tests were performed using a modified PESPL RF gridded ion thruster described in chapter 5 and shown in figure 5.1a repeated here for convenience as figure 6.1. The grids on the thruster are molybdenum, and the discharge chamber is quartz glass. Material investigations were performed on the HV anode piece in the thruster. Two anode materials were tested: titanium and stainless steel, with two gas feeds: pure molecular nitrogen (N_2) and air (78% N2 + 21% O2).

Material studies were conducted with a modified version of the PESPL thruster. Due

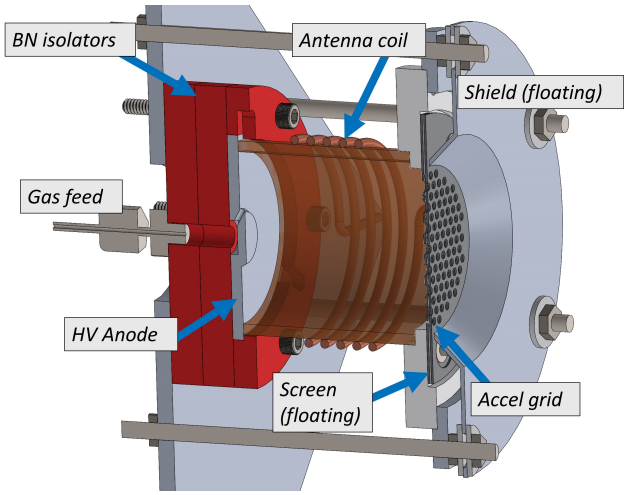

Figure 6.1: Design model of the thruster head. Note the HV anode used in the materials studies [17]. The grids are made of molybdenum.

Gas Feed	Anode Material
20 sccm N_2 + 2 sccm Xe	Titanium
20 sccm N_2 + 2 sccm Xe	Stainless Steel
20 sccm air + 2 sccm Xe	Titanium
20 sccm air + 2 sccm Xe	Stainless Steel

Table 6.1: Table showing all test combinations for the study.

to poor thermal sinking of the PCB match network, the thruster could not be operated at high power for longer than 30 minutes. Also, the match network was not finalized when the materials experiments were conducted. Thus the thruster was instead operated with an Advanced Energy Cesar 13.56 MHz RF generator and VM600 automatic variable match network located outside the vacuum chamber. A Pearson coil on the RF feed line downstream of the match network was used to measure the coil current during operation.

Grids with an NSTAR style hole sizing was used which necessitated a higher gas flow rate than was required for normal thruster operation with MiXI style hole sizing [133]. Xenon was also added to the gas feed to aid ionization and reduce power requirements. All tests

were run with 20 sccm of air or nitrogen gas with 2 sccm on xenon added. Table 6.1 shows the test combinations. All tests were run for 45 minutes. The device was operated at 150 W RF forward power from the generator, but using the measured current the power delivered to the plasma is 50% the forward power or 75 W [17, 106]. The high power losses are due to the long feed line between the match network outside of the vacuum chamber and the thruster. After each test, the anode plates were replaced, but the molybdenum grids were left in place during the entire test. Nitrogen tests were performed before air tests. A beam was not extracted during the tests to avoid contamination due to grid erosion.

6.2 Material Characterization Results

Post test characterization was performed on the four anode samples. Optical and SEM imaging were used to qualitatively analyze surface properties. XPS was used to identify surface atomic composition. Optical images of the samples are shown as figure 6.2. The outer edge of the plate is covered by the discharge chamber wall and not exposed to the plasma.

A surface layer is easily seen on the air exposed samples. The nitrogen exposed stainless steel sample does not have a visible surface layer, while the nitrogen exposed titanium sample shows a faint tan layer as seen in figure 6.3. This layer is likely titanium nitride (TiN) formed during exposure to the nitrogen plasma.

XPS analysis was used to determine the surface atomic composition of each sample. Data was taken from halfway between the center and the outer edge of the exposed portion. Table 6.2 shows the percent composition of each sample obtained via XPS analysis.

Carbon present on the samples is likely due to environmental contamination. Both of the air exposed samples show the same composition of molybdenum and oxygen regardless of sample material. This is likely molybdenum oxide forming on the grids and then depositing on the bottom anode. The deposited molybdenum oxide coating is thick enough that

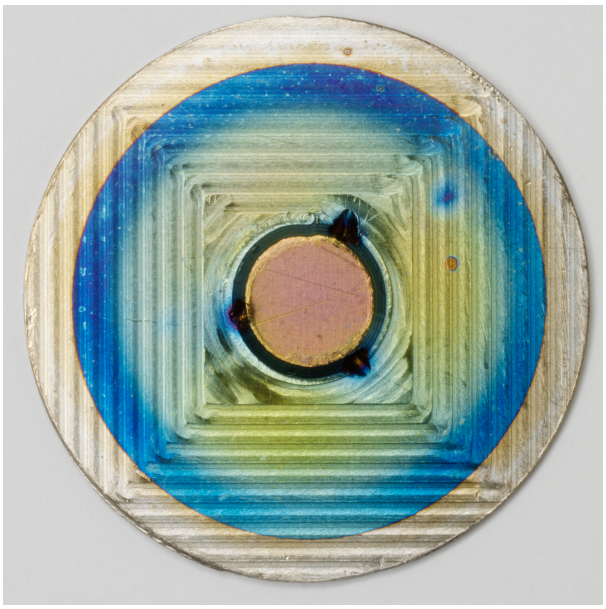

(a) Air - titanium

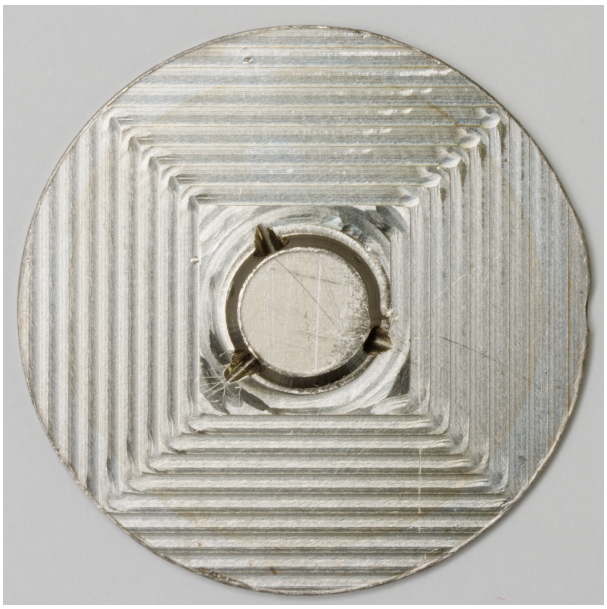

(b) Nitrogen - titanium

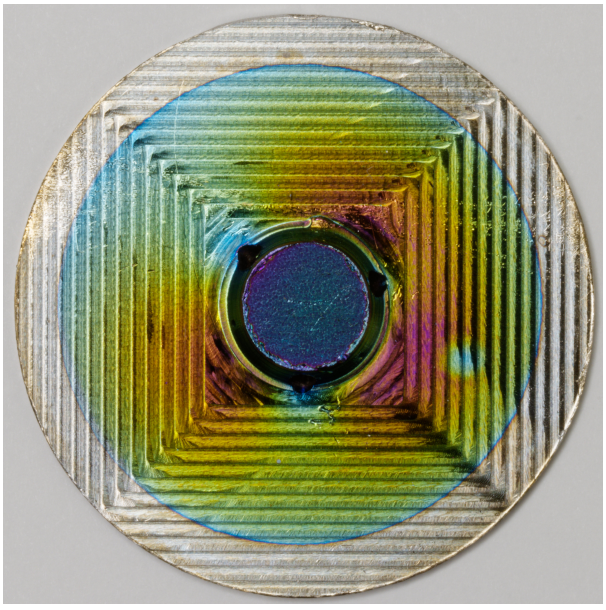

(c) Air - stainless steel

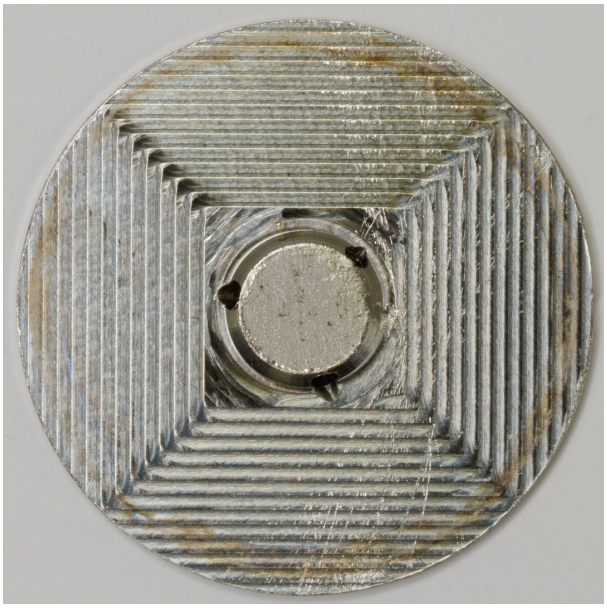

(d) Nitrogen - stainless steel

Figure 6.2: Anode samples after plasma exposure. The blue color seen on the air exposed samples is likely from molybdenum oxide. The outer edge was not exposed to plasma.

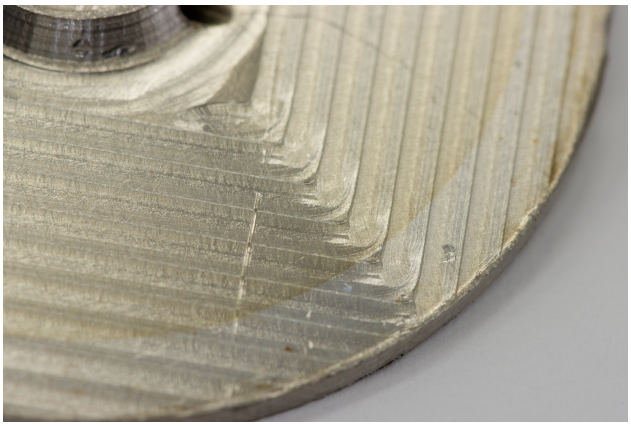

Figure 6.3: Detail of the nitrogen exposed titanium sample showing the faint surface layer. This layer is likely titanium nitride (TiN).

	O	Mo	C	Ti	N	Si	B	Cr	Fe
Air - Ti	45.13	30.6	24.27	-	-	-	-	-	-
Air - SS	45.36	31.32	23.32	-	-	-	-	-	-
N_2 - Ti	24.35	0.24	16.5	25.47	27.61	5.83	-	-	-
N_2 - SS	45.25	0.22	7.75	-	6.72	16.36	7.01	4.92	11.76

Table 6.2: Atomic percent composition of each sample from XPS analysis.

the underlying anode material is not visible with XPS. Optical images support this as the deposited layer of blue molybdenum oxide is clearly visible.

For the nitrogen exposed titanium sample, very little molybdenum is seen. This implies that pure nitrogen has little reactivity with the grids, and oxygen interaction is the source of molybdenum on the air exposed samples. A high percentage of nitrogen is seen on the surface due to formation of titanium nitride. A peak at 455 to 456 eV supports the presence of TiN. TiO has a similar binding energy, but TiO_2 is more stable and more likely to form upon exposing titanium to the atmosphere, so it is unlikely that a significant amount of TiO is present on the surface. Oxygen present on the surface is likely due to TiO_2 formation after exposure to the atmosphere. Optical imaging shows a faint tan layer formed on the surface

shown in figure 6.3 which may be TiN. A small amount of silicon is on the surface. The only source of silicon in the system is the quartz glass (SiO_2) discharge chamber walls. Nitrogen does not form volatile species with quartz glass through chemical interactions, but physical sputtering can occur due to capacitive coupling to the high voltage side of the antenna coil [17]. Capacitive coupling causes some ions to impact the discharge chamber wall at high energies sputtering material. Sputtered SiO_2 can redeposit onto the anode sample.

Silicon is also present on the nitrogen exposed stainless steel sample, again due to physical sputtering of the discharge chamber wall from capacitive coupling. Low amounts of molybdenum is again seen on the sample showing low reactivity of molybdenum with nitrogen. Boron and nitrogen are seen on the surface. These elements are likely contamination from the boron nitride (BN) ceramic used to electrically isolate the anode. BN parts are shown in red in figure 6.1. Oxygen on the surface could be due to chromium oxide (Cr_2O_3) formation on the surface after exposure to the atmosphere.

The grids were removed and photographed after the conclusion of all tests, shown as figure

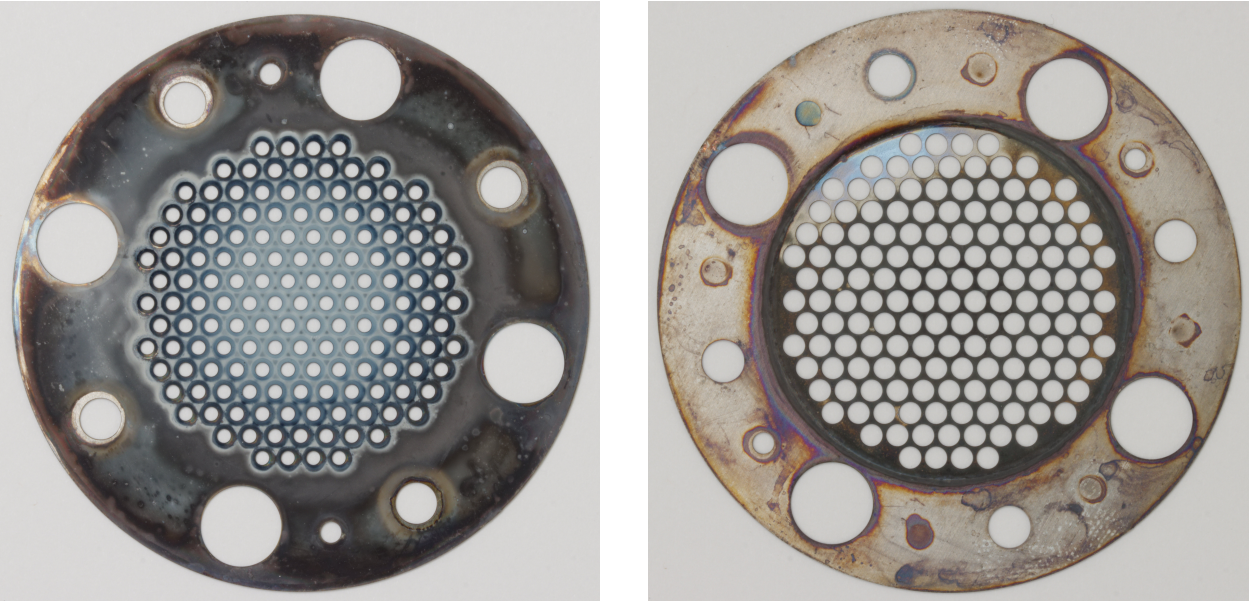

(a) Accel grid upstream face

(b) Screen grid upstream face

Figure 6.4: Screen and accel grids after all runs. The accel grid shows a blue-white coating which may be molybendnum oxide. This coating is not present on the screen grid.

6.3 Material Characterization Conclusions

Materials analysis of the anode plate in the PESPL RF gridded ion thruster shows that molybdenum has poor oxygen resistance, forming oxides which deposit elsewhere inside the plasma discharge chamber. Molybdenum showed little reactivity with pure nitrogen, so it is likely a suitable material for nitrogen based propellants. The thick molybdenum oxide layer which formed on all air exposed anode samples made direct study of air - titanium and air - stainless steel interactions impossible. Future studies should use an inert grid substitute or a grid material matching the anode material.

In the presence of a nitrogen plasma, titanium forms a titanium nitride (TiN) layer. TiN is electrically conductive, so this layer will likely not degrade anode performance. Stainless steel shows little reactivity to the nitrogen plasma with no directly discernible nitrogen compounds formed from the plasma.

Silicon is seen on both nitrogen exposed samples, likely due to capacitive coupling with the high voltage side of the RF coil. Deposition of silicon on thruster electrodes can decrease electrode conductivity to the plasma and degrade performance. Improved antenna match networks can significantly reduce capacitive coupling mitigating this issue [106].

CHAPTER 7

Conclusion

7.1 Summary of Conclusions

This dissertation presents a system level analysis and experimental thruster data for air breathing electric propulsion (ABEP) spacecraft and alternative propellants. Major findings of this work include:

1. Thrust-to-power (T/P) of an ABEP thruster is a major driver of spacecraft mission performance.

2. Geomagnetic storms present a risk to low ballistic coefficient ABEP spacecraft, but this risk can be mitigated through preemptive orbit raising or xenon propellant addition.

3. Performance data for a 3 cm RF gridded ion thruster operating on xenon, several alternative propellants including air, and air-xenon mixtures was collected.

4. Nitrogen propellant shows little reactivity with titanium, molybdenum, or stainless steel, but air propellant shows poor compatibility with molybdenum.

An ABEP spacecraft system model was developed in chapter 2 to determine mission performance based on spacecraft geometry and propulsion performance for VLEO orbits. Power collected on orbit is shown to be heavily dependent on β angle, leading to up to 70% reductions in average power collected from the sun-synchronous orbit case for a VLEO spacecraft. Given a geometry optimized for low altitude operation, increasing T/P of the

propulsion system is the most impractical way of minimizing operating altitude and improving power margin. A target ABEP T/P of 10 mN/kW was identified, while increases beyond this target greatly improved system performance. ABEP CubeSat performance was compared with a conventional EP CubeSat of the same bus geometry to determine mission scenarios which favor ABEP over conventional EP. It was found that for missions of 3 years or longer, payload volume becomes severely reduced for EP spacecraft below 240 km and ABEP spacecraft become favorable, which is in agreement with previous studies [25].

Chapter 3 shows that low C_b and low T/D spacecraft are highly susceptible to increased atmospheric drag during geomagnetic storm events which can cause the spacecraft to deorbit. Preemptive orbit raising and xenon addition to the propulsion system are investigated as risk mitigation strategies for geomagnetic storm events. Preemptive orbit raising is shown to successfully reduce risk for spacecraft with sufficiently high T/D to quickly orbit raise ahead of a storm. Xenon addition during a geomagnetic storm is shown to improve survivability for all spacecraft and is particularly useful for low T/D spacecraft which are not able to orbit raise quickly. A relatively small amount of xenon is shown to significantly improve survivability during high drag events at the cost of increased system complexity.

Experimental development of a lab model 3 cm RF gridded ion thruster for operation on air as well as other alternative propellants is described in chapters 4 and 5. RF gridded ion thrusters do not require a thermionic emitter cathode making them particularly attractive for reactive alternative propellants such as air. A review of the basic principles of RF gridded ion thruster design is provided in chapter 4 to increase accessibility of these thrusters to new users. These principles were applied to create the PESPL RF gridded ion thruster, a low-cost lab model thruster.

The PESPL 3 cm RF gridded ion thruster was characterized on xenon and several alternative propellants including air and a hydrazine surrogate. Section 5.2 the experimental setup for operating the thruster. Direct performance comparisons are made between propellants. A global model presented in appendix A is used to support experimental measurements and

predict extracted beam composition for dissociative propellants and gas mixtures. Nitrogen based propellants are predicted to be highly dissociated in agreement with previous global models [129]. A thrust-to-power of 7.9 mN/kW at 3200 s I_{sp} was demonstrated on air. Air-xenon mixtures were tested experimentally showing significant increases in thrust-to-power. Through xenon addition, thruster performance can be brought to a level where it becomes viable for ABEP applications [10].

XPS surface analysis was performed on the anode plate of the PESPL RF gridded ion thruster operating on pure nitrogen and air. Results presented in chapter 6 show that molybdenum has poor oxygen resistance, but little reactivity with pure nitrogen, so it is likely a suitable material for nitrogen based propellants. Titanium and Stainless steel showed little reactivity to the nitrogen plasma making them good candidates for future studies. The thick molybdenum oxide layer formed on the anode during operation with air propellant making air-titanium and air-stainless steel studies inconclusive. Silicon is seen on both nitrogen exposed samples, likely due to capacitive coupling with the high voltage side of the RF coil. Improved antenna match networks can significantly reduce capacitive coupling mitigating this issue [106].

It is the author's hope that results presented in this dissertation will support further ABEP development as well as provide an understanding of RF gridded ion thrusters for future generations of EP scientists and engineers.

7.2 Future Work

7.2.1 ABEP System Analysis

Several ABEP system performance studies have been published extending the work presented in chapter 2. Tisaev et al. identified operating envelopes for ABEP spacecraft and control algorithms for ABEP stability using fixed values for I_{sp} and T/P [32]. Ko et al. extended the work of Tisaev by using a global model to compute thruster performance values [134].

Mission studies could be further extended by incorporating experimental thruster data into the system analysis. Experimental thruster data can be combined with an orbit propagator as described in chapter 3 to further validate the ABEP operating envelope. A further realization of this could be to perform a hardware in the loop (HTTL) simulation to control the gas feed to the thruster based on inlet and atmosphere parameters, and then measure thrust and power usage in real time. This may also be useful for determining ABEP thruster lifetime under conditions which would be experienced on orbit.

7.2.2 RF Thruster Design Methodology

Current literature on practical RF ICP design is limited, particularly in regard to match network design. The EP community would benefit from a tutorial on ICP design for propulsion as these devices become more common.

7.2.3 Advanced PESPL Thruster Diagnostics

Improved thruster diagnostics can be used to gain more insight into thruster operation and improve the accuracy of measured performance metrics. A Faraday probe can be used to measure the plume profile yielding plume divergence and verifying the extracted beam current. An ExB probe can be used to determine the extracted beam composition. Sweeping the ExB probe through the plume can reveal insights into the distribution of species within the plume (light particles at high angles, ect...).

Spectrographic diagnostics can provide insight to thruster discharge processes. A collisional radiative model for xenon and krypton is currently in development which can be used to determine plasma density and temperature for xenon and krypton. Advanced spectroscopy techniques such as actinometry can be applied to molecular plasmas to investigate excitation modes [101].

7.2.4 PESPL Thruster Improvements

Several improvements can be made to the PESPL RF gridded ion thruster to improve robustness and performance. Hardware design improvements can be made to increase build repeatability between users and reduce facility interaction. The current match network housing has a poor thermal sink leading to overheating during long duration tests. Additionally, the current match network provides a VSWR of 3 during operation. High VSWR causes increased coil voltage increasing capacitive coupling to the plasma reducing discharge efficiency, changing coupling efficiency, and in general changing the operating conditions relative to how a thruster would operate in practice. A new match network PCB with properly sized traces for the capacitors used should improve reliability. Match networks utilizing a split series capacitor, one on the upstream side and one on the downstream side, can further reduce coil voltage increasing efficiency [106]. Faraday shields can be used to reduce capacitive coupling to the plasma, but they can be difficult to implement properly and reduce power coupling to the plasma [105, 106].

7.2.4.1 Ferromagnetic Enhanced ICP Discharge

Ferromagnetic enhanced ICP (FMICP) discharges have been investigated for improving power coupling to the plasma discharge in semiconductor plasma reactors and neutral beam sources [135, 136, 115, 137, 138, 139, 140]. Few FMICP concepts have been presented for propulsion applications. The PEGASES and MINT gridded ion thrusters utilizing electronegative gasses employed ferromagnetic enhanced discharges [141, 142]. Godyak, Raitses, and Fisch tested a neutralizer cathode based on a FMICP discharge [143]. Celik and Kurt tested a FMICP cathode finding reduced performance relative to a standard ICP cathode with the same geometry. Reduced performance with the FMICP discharge is likely due to poor implementation of the ferrite cores providing weak magnetic coupling to the plasma [106].

In a traditional ICP, magnetic flux lines can be reflected from the plasma discharge instead coupling with other parts of the thruster as described in chapter 4. The addition of ferrite cores around the RF antenna coil can direct magnetic flux towards the plasma discharge significantly improving coupling, particularly at high electron temperatures. Care must be taken in the design to ensure that the ferrites have low-loss and the magnetic flux is directed to the plasma [144]. Ferrite material should be rated to the driving frequency and the ferrites should be sized to accommodate the magnetic flux [145, 116]. A major challenge to implementing ferrite cores is heat rejection. Ferrites have a low operating temperature, so a FMICP based thruster would need to effectively remove heat from the thruster keeping the ferrite cores within the operating temperature range.

7.2.5 Future Material Compatibility Studies

Further work on material compatibility with reactive plasma discharges should investigate oxygen and air compatibility with titanium and stainless steel. Results presented in chapter 6 could not investigate air plasma interaction with titanium or stainless steel due to the molybdenum oxide layer which formed on the anode samples. Future studies could use the same material for the thruster grids as the anode plate. Nitrogen and hydrogen mixtures could be investigated as well. Tejeda at al. observed reduced oxygen resistance of stainless steel when hydrogen is included [36].

Appendix A

Global Model

A global model of the plasma discharge is used to provide insight into thruster plasma conditions at different operating points and to estimate the ion beam composition for thrust calculations. Global models ignore spatial variations in the plasma computing average values for the plasma discharge. The model is based on existing global models from the materials processing community as well as models specifically for ABEP applications [101, 146, 147, 129, 134]. Ion extraction from the discharge is included in the model based on work published by Chabert et al. [148].

A.1 Non-Dissociative

For non-dissociating plasmas, such as noble gas propellants or molecular propellants where dissociation is neglected, the global model reduces to a simplified form which can be solved directly for a given beam current [101]. Using conservation of particles, gas flow rate into the thruster can be equated to the gas lost as beam and neutrals:

$$\dot{N}_p = \frac{I_b}{e} + \frac{n_g \bar{c} A_g \Theta_n}{4} \tag{A.1}$$

Where A_g is the total grid area, $\dot{N}_p$ is the propellant particle flow rate, and Θ_n is the grid neutral transparency defined as $\Theta_n \equiv \eta_c \frac{A_{open}}{A_g}$. Rearranging equation A.1 to solve for the neutral gas density in the thruster n_g yields:

$$n_g = \frac{4}{\bar{c} A_g \Theta_n} \left(\dot{N}_p - \frac{I_b}{e} \right) \tag{A.2}$$

After calculating the neutral density, the electron temperature can be found by numerically solving equation A.3 where $u_B = \sqrt{\frac{eT_e}{M}}$ is the Bohm velocity [101]. T_e is in units of eV.

$$\frac{K_{iz}(T_e)}{u_B(T_e)} = \frac{1}{n_g d_{eff}} \tag{A.3}$$

K_{iz} is the ionization rate coefficient for the gas as a function of electron temperature. Rate coefficients for any process (ionization, excitation, dissociation, ect...) can be computed for a Maxwellian plasma from the reaction cross section $\sigma(\epsilon)$ by numerically solving equation A.4 [149]. Cross sections for various processes can be found in the literature.

$$k(T_e) = \int_0^\infty \sigma(\epsilon) \left(\sqrt{\frac{8eT_e}{\pi m_e}} \right) \frac{\epsilon}{T_e} \exp\left(-\frac{\epsilon}{T_e} \right) \frac{1}{T_e} d\epsilon \tag{A.4}$$

d_{eff} is an effective plasma size defined as:

$$d_{eff} = \frac{1}{2} \frac{Rl}{2Rh_l + lh_R} \tag{A.5}$$

Where R is the radius of the cylindrical plasma volume, l is the length of the cylindrical plasma volume, and $h_R = 0.86 \left(3 + \frac{l}{2\lambda_i} \right)^{-\frac{1}{2}}$ and $h_l = 0.8 \left(4 + \frac{R}{\lambda_i} \right)^{-\frac{1}{2}}$ are the empirically derived radial and axial edge-to-center density ratios for intermediate density plasmas [101]. $\lambda_i = \frac{1}{n_g \sigma_i}$ is the ion mean free path where $\sigma_i = 1 \times 10^{-18} \mathrm{m}^2$ is the global scattering cross section [101].

Taking the equation for beam current $I_b = h_l n_e e u_B(T_e) A_g \Theta_i$ and rearranging to solve for plasma density n_e yields equation A.2 which can be solved using the T_e from equation A.3.

$$n_e = \frac{I_b}{e A_g \Theta_i u_B(T_e) h_l} \tag{A.6}$$

Ion transparency is computed for the individual grid ion optics and can change depending on operating conditions. For the PESPL RF ion thruster ion transparency is assumed to be a constant $\Theta_i = 0.73$ based on CEX-2D simulations [150]. Required RF power absorbed by the plasma can be computed using the electron temperature T_e and plasma density n_e in equation A.7 [101].

$$P_{abs} = e n_e u_B(T_e) A_{eff} \epsilon_T(T_e) \tag{A.7}$$

Total collisional energy lost per ion generated ϵ_T is given as $\epsilon_T = \epsilon_c + \epsilon_e + \epsilon_i$ where ϵ_c is the collisional energy loss, $\epsilon_e = 2T_e$ is the mean energy lost per electron lost to the wall, and $\epsilon_i = V_s + \frac{1}{2}T_e$ is the mean energy lost per ion lost to the wall [101]. $V_s = T_e \log\left(\frac{M}{2\pi m_e}\right)$ is the sheath voltage in a single species plasma. Collisional energy loss taking into account ionization, electronic excitation, and momentum transfer collisions can be written as [101]:

$$\epsilon_c = \epsilon_{iz} + \frac{K_{ex}(T_e)}{K_{iz}(T_e)}\epsilon_{ex} + \frac{K_{el}(T_e)}{K_{iz}(T_e)}\frac{3m}{M}T_e \tag{A.8}$$

Where K_{iz}, K_{ex}, and K_{el} are the ionization, excitation, and elastic scattering rate coefficients respectively computed for a Maxwellian plasma using equation A.4.

Solving equations A.2, A.3, A.5, and A.7 yields the plasma conditions and required RF power absorbed by the plasma for a given beam current for a non-dissociating propellant gas. This simplified model for a single species is useful as it does not rely on simultaneously solving a set of nonlinear equations reducing computational time.

A.2 Nitrogen Model Including Dissociation

Nitrogen plasma models in literature have shown significant dissociation of molecular nitrogen for ABEP operating conditions [129]. Accounting for dissociation requires the use of unsimplified ion and power conservation equations presented by Lieberman and Lichtenberg

[101]. A modification from the originally published models has been made to the ion sound speed to accommodate multispecies plasmas. Baalrud et al. [151] showed theoretically that the ion sound speed in a multispecies plasma is the same for all species due to slowing of lighter, faster, ions by the two stream instability. The system ion sound speed c_s, shown as equation A.9 where all ionized species k are summed over, is incorporated into the global model replacing the Bohm velocity [152, 151].

$$c_s = \sqrt{\sum_k \frac{n_k e T_e}{n_e M_k}} \tag{A.9}$$

Recent literature suggests this system ion sound speed may break down for plasmas containing more than two species, but this is ignored for this work [153]. The use of the system sound speed for the ion velocity entering the sheath leads to a modified sheath voltage, V_{sm}, for the multispecies plasma. V_{sm} is computed by equating the electron and ion fluxes entering the sheath: $n_e c_s = \frac{1}{4} n_e \bar{c}_e \exp\left(\frac{-V_{sm}}{T_e}\right)$ where $\bar{c}_e = \sqrt{\frac{8eT_e}{\pi m_e}}$ is the electron thermal velocity. Solving for V_{sm} yields the multispecies sheath voltage:

$$V_{sm} = T_e \log \sqrt{\frac{eT_e}{2\pi m_e}} \frac{1}{c_s} \tag{A.10}$$

The global model uses a set of particle conservation equations to track ion and neutral species densities as well as a power conservation equation to determine electron temperature. The set of governing equations for nitrogen including dissociation is:

$$\frac{dN_{N_2^+}}{dt} = K_{iz}^{(N_2)}(T_e) n_{N_2} n_e V - n_{N_2^+} c_s A_{eff} \tag{A.11}$$

$$\frac{dN_{N^+}}{dt} = K_{iz}^{(N)}(T_e) n_N n_e V - n_{N^+} c_s A_{eff} \tag{A.12}$$

$$\frac{dN_{N_2}}{dt} = \dot{N}_{N_2} - K_{diss}^{N_2}(T_e) n_{N_2} n_e V - \frac{1}{4} n_{N_2} \bar{c}_{N_2} n_e V - h_l n_{N_2^+} A_g \Theta_i c_s - V \frac{dn_{N_2^+}}{dt} \tag{A.13}$$

$$\frac{dN_N}{dt} = 2K_{diss}^{N_2}(T_e)n_{N_2}n_eV - \frac{1}{4}n_N\bar{c}_N n_e V - h_l n_{N^+}A_g\Theta_i c_s - V\frac{dn_{N^+}}{dt} \tag{A.14}$$

$$\frac{dT_e}{dt} = T_e\left(\frac{P_{abs}}{W_e(n_e,T_e)} - \sum_j\left(\frac{2}{3}\frac{\epsilon_c^{(j)}}{T_e}+1\right)K_{iz}^{(j)}n_j - \left(\frac{2}{3}\frac{V_{sm}+\frac{5}{2}T_e}{T_e}-1\right)\frac{c_s}{d_{eff}}\right) \tag{A.15}$$

$$\frac{dN_e}{dt} = \sum_k \frac{dN_k}{dt} \tag{A.16}$$

For equation A.15 all neutral species j are summed over, and for equation A.16 all ionized species k are summed over. $\dot{N}_{N_2}$ is the nitrogen gas feed rate. The set of governing ODEs are solved using ODE45 for the steady state by allowing the time differentials to relax to steady state values $\left(\frac{d}{dt}\to 0\right)$ [154]. Initially, the author tried to solve the governing set of equations in steady state by setting $\left(\frac{d}{dt}=0\right)$ and using a nonlinear solver, but this solution method did not converge. Allowing the ODEs to relax to steady state values provided better convergence.

A.2.1 Xenon-Nitrogen Mixtures

The global model can be extended to include additional species through the addition of more conservation equations for those species. This work focuses on xenon-nitrogen mixtures to approximate air-xenon mixtures. Conservation equations added to the governing set for xenon are:

$$\frac{dN_{Xe^+}}{dt} = K_{iz}^{(Xe)}(T_e)n_{Xe}n_eV - n_{Xe^+}c_sA_{eff} \tag{A.17}$$

$$\frac{dN_{Xe}}{dt} = \dot{N}_{Xe} - \frac{1}{4}n_{Xe}\bar{c}_{Xe}n_eV - h_l n_{Xe^+}A_g\Theta_i c_s - V\frac{dn_{Xe^+}}{dt} \tag{A.18}$$

Xenon should be included in the summations for equations A.15 and A.9.

A.3 Discussion of Global Models

Thruster performance can be predicted using the presented global models along with equations 5.3 to 5.9. Determining thruster performance for dissociating species or gas mixtures without experimental measurements of the plume composition relies on the global model in section A.2 to estimate the beam composition. A limitation of the presented models is that the power absorbed by the plasma P_{abs} is not necessarily the power delivered to the thruster. A coupling coefficient k can be used to determine the percentage of RF power delivered to the thruster is absorbed by the plasma where $P_{abs} = kP_{RF}$ [12].

Appendix B

EDS Data

This appendix contains EDS data for the thruster anode material study. EDS data agrees with the presented XPS data, but the EDS data is inconclusive as the energy peaks for many of the species of interest are overlapping. Figures B.1 shows SEM images of the anode sample edge. The exposed and unexposed portions of each sample are labeled. Two data points were taken for each sample, one in the exposed region and one in the unexposed region. Figures B.2 and B.3 contain the EDS spectra for all sampled points. Many of the species of interest have overlapping EDS spectra making it difficult to differentiate between species. For this reason, XPS is prefered over EDS in hte material study.

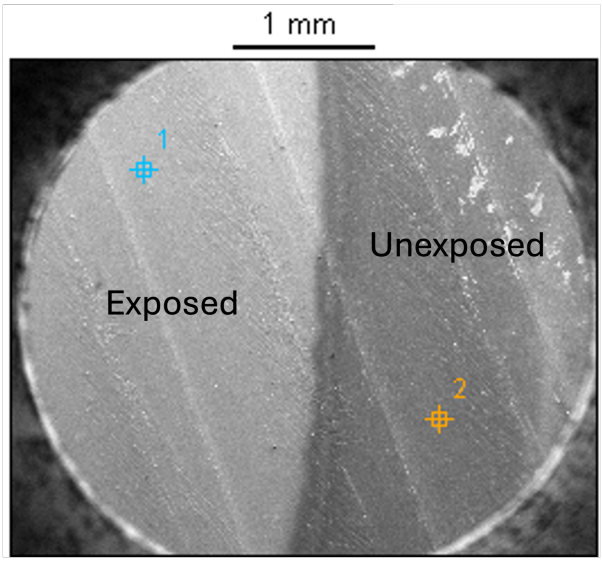

(a) Air - titanium

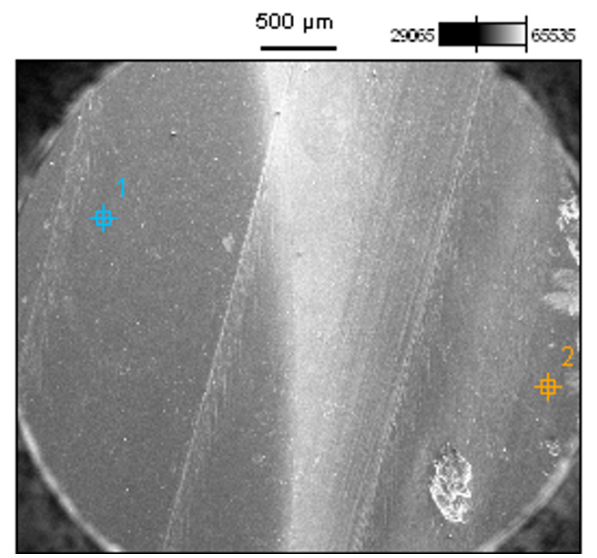

(b) Nitrogen - titanium

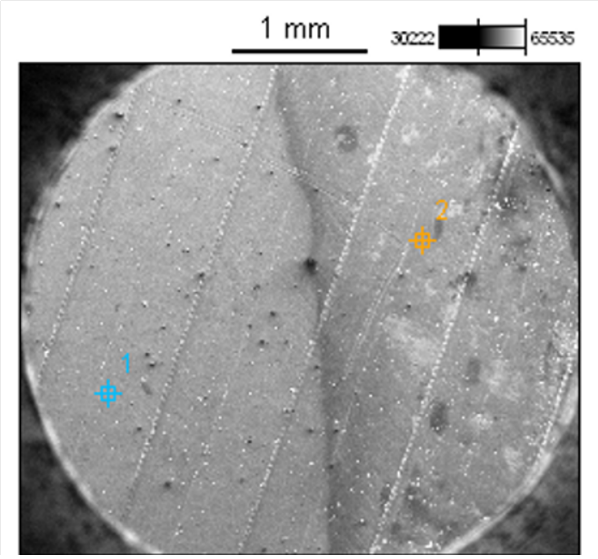

(c) Air - stainless steel

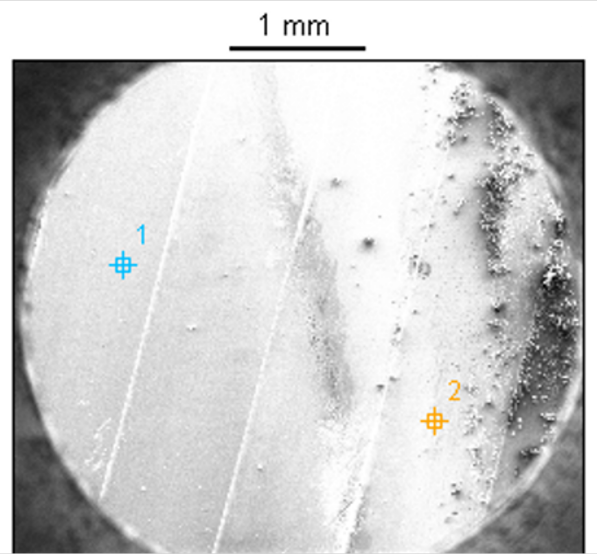

(d) Nitrogen - stainless steel

Figure B.1: SEM images of the anode sample edge showing the interface between the exposed and unexposed portions of the sample. Labeled spots are where EDS data was taken.

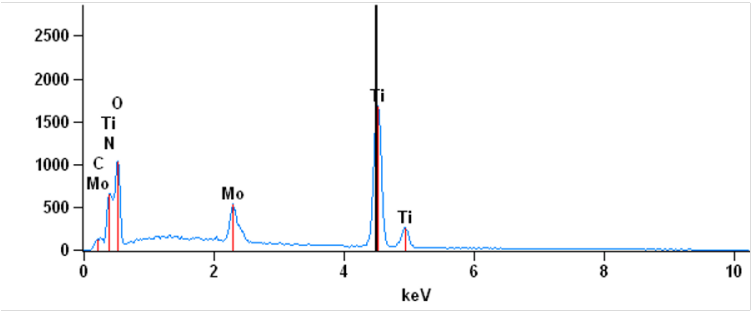

(a) Air - titanium point 1

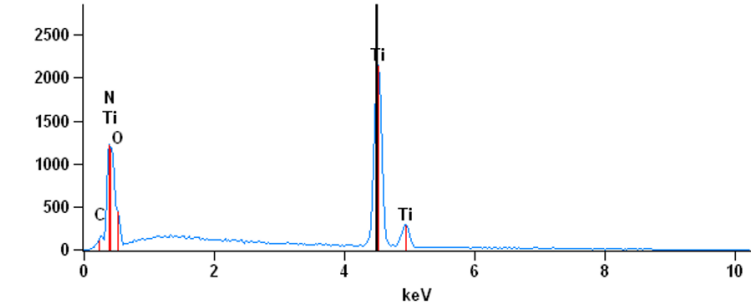

(b) Air - titanium point 2

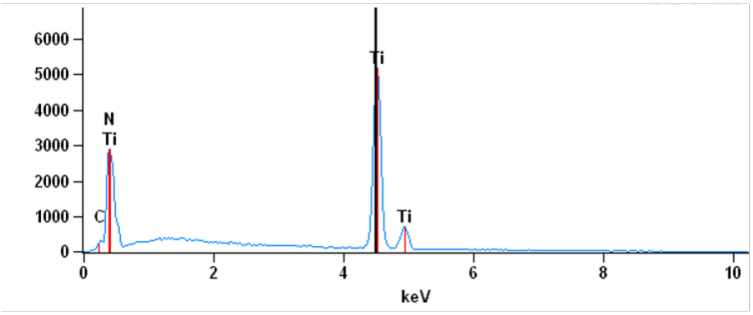

(c) Nitrogen - titanium point 1

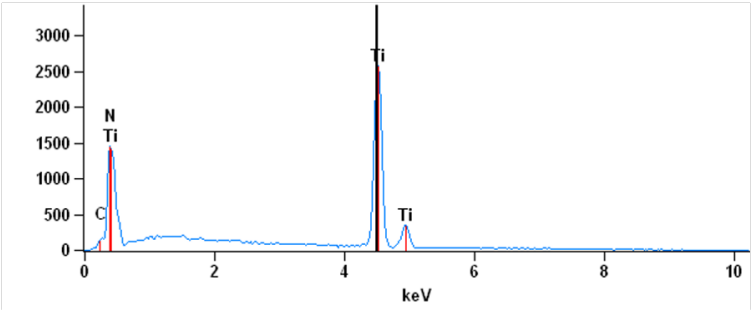

(d) Nitrogen - titanium point 2

Figure B.2: EDS spectra for all surveyed points on the titanium anode.

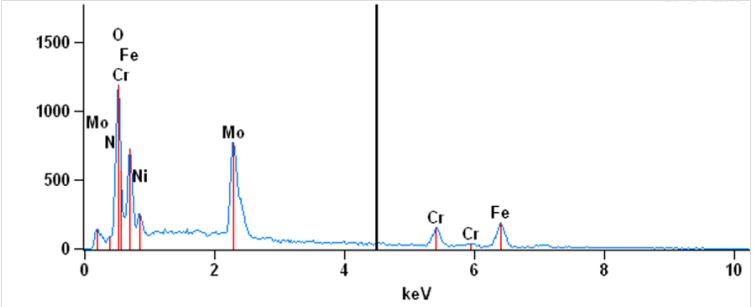

(a) Air - stainless steel point 1

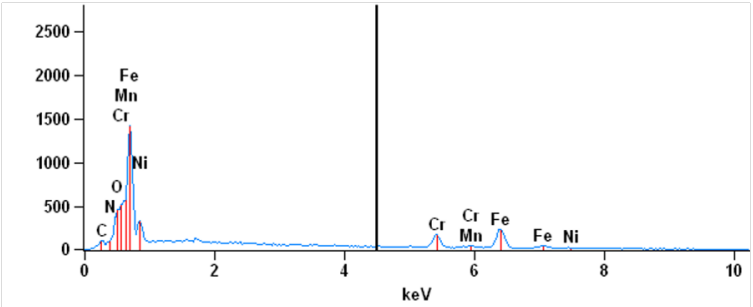

(b) Air - stainless steel point 2

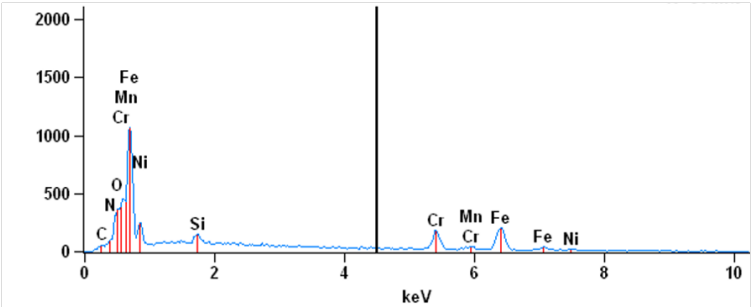

(c) Nitrogen - stainless steel point 1

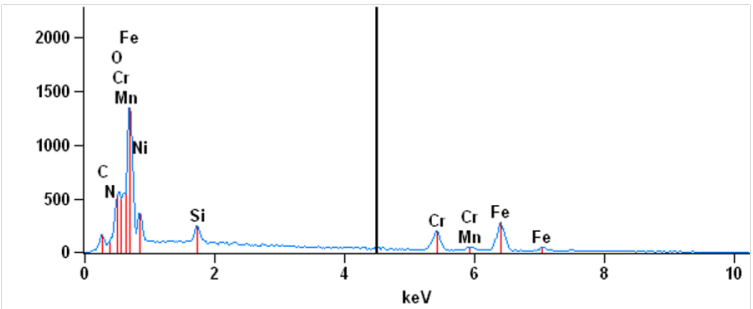

(d) Nitrogen - stainless steel point 2

Figure B.3: EDS spectra for all surveyed points for the stainless steel anode.

REFERENCES

[1] Crisp N H, Roberts P C, Livadiotti S, Oiko V T A, Edmondson S, Haigh S, Huyton C, Sinpetru L, Smith K, Worrall S *et al.* 2020 *Progress in Aerospace Sciences* 117 100619

[2] Andreussi T, Ferrato E, Piragino A, Cifali G, Rossodivita A and Andrenucci M 2018 Development and experimental validation of a hall effect thruster ram-ep concept *Space Propulsion Conference 2018*

[3] National Oceanic and Atmospheric Administration 2021 Penticton 10.7cm solar radio flux URL https://www.ngdc.noaa.gov/stp/space-weather/solar-data/solar-features/solar-radio/noontime-flux/penticton/penticton$_o bserved/$

[4] Analytical Graphics, Inc 2021 Systems tool kit (stk) URL https://www.agi.com/products/stk

[5] Schönherr T, Komurasaki K, Romano F, Massuti-Ballester B and Herdrich G 2015 *IEEE Transactions on Plasma Science* 43 287–294

[6] Lotz B 2013 *Plasma physical and material physical aspects of the application of atmospheric gases as a propellant for Ion-Thruster of the RIT-Type* Ph.D. thesis University of Giessen

[7] Busek Company 2012 Atmospheric breathing electric thruster for planetary exploration URL https://www.nasa.gov/pdf/636899main$_H ohman_P resentation.pdf$

[8] Busek Company 2023 Rf ion thrusters URL https://www.busek.com/rf-ion-thrusters

[9] Jackson S W 2017 *Design of an Air-Breathing Electric Thruster for CubeSat Applications* Dissertation University of Colorado, Boulder

[10] Crandall P and Wirz R E 2022 *Journal of Electric Propulsion* 1 12

[11] Kyoto University 2023 Geomagnetic data service URL https://wdc.kugi.kyoto-u.ac.jp/wdc/Sec3.html

[12] Godyak V, Piejak R and Alexandrovich B 1992 *Plasma Sources Sci. Technol* 1 36

[13] Chen F F 1992 *UCLA Report*

[14] Chabert P, Tsankov T V and Czarnetzki U 2021 *Plasma Sources Science and Technology* 30 024001

[15] Piskin T, Qian Y, Pribyl P, Gekelman W and Kushner M J 2023 *Journal of Applied Physics* 133

[16] Ottaviano A 2023 *Plasma Interactions and Electron Dynamics for Volumetrically Complex Materials* Ph.D. thesis University of California, Los Angeles

[17] Crandall P, Cretel C and Wirz R E 2024 Rf gridded ion thruster design for laboratory experiments *AIAA SCITECH 2024 Forum* p 1549

[18] Ariane Group 2023 Electric ion space propulsion systems and thrusters URL https://www.space-propulsion.com/spacecraft-propulsion/propulsion-systems/electric-propulsion/index.html

[19] Lewis H, Radtke J, Rossi A, Beck J, Oswald M, Anderson P, Virgili B and Krag H 2017 70

[20] Weeden B 2010 2007 chinese anti-satellite test fact sheet Tech. rep. Secure World Foundation Broomfield, CO URL https://swfound.org/media/9550/chinese$_a sat_f act_s heet_u pdated_2$012.*pdf*

[21] ANTONY J BLINKEN 2021 Russia conducts destructive anti-satellite missile test URL https://www.state.gov/russia-conducts-destructive-anti-satellite-missile-test/

[22] ESA Earth Observation Portal 2021 Goce (gravity field and steady-state ocean circulation explorer) URL https://directory.eoportal.org/web/eoportal/satellite-missions/g/goce

[23] Steiger C, Romanazzo M, Emanuelli P, Floberghagen R and Fehringer M 2014 The de-orbiting of esa's gravity mission goce - spacecraft operations in extreme drag conditions *13th International Conference on Space Operations*

[24] ESA Earth Observation Portal 2021 Slats (super low altitude test satellite) / tsubame URL https://directory.eoportal.org/web/eoportal/satellite-missions/s/slats

[25] Di Cara D, Del Amo J G, Santovincenzo A, Dominguez B C, Arcioni M, Caldwell A and Roma I 2007 Ram electric propulsion for low earth orbit operation: an esa study *30th International Electric Propulsion Conference*

[26] Hruby V, Hohman K and Szabo J 2022 Air breathing hall effect thruster design studies and experiments *37th International Electric Propulsion Conference, Boston, Massachusetts, IEPC-2022-446. https://www. electricrocket. org/index. php*

[27] Zheng P, JWu, Zhang Y and Wu B 2020 *International Journal of Aerospace Engineering* 2020

[28] Andreussi T, Ferrato E and Giannetti V 2022 *Journal of Electric Propulsion* 1 31

[29] Li Y, Chen X, Li D, Xiao Y, Dai P and Gong C 2015 *Vacuum* 120

[30] Underwood T 2022 Air breathing dual mode plasma thruster *37th International Electric Propulsion Conference, IEPC-2022-438*

[31] Raitses Y, Chopra N and Simmonds J 2022 Electron-beam generated e×b plasma for air-breathing propulsion *37th International Electric Propulsion Conference, IEPC-2022-443*

[32] Tisaev M, Ferrato E, Giannetti V, Paissoni C, Baresi N, Fabris A L and Andreussi T 2022 *Acta Astronautica* 191 374–393

[33] Cifali G, Misuri T, Rossetti P, Andrenucci M, Valentian D, Feili D and Lotz B 2011 Experimental characterization of het and rit with atmospheric propellants *32nd International Electric Propulsion Conference* 11-15 p 21

[34] Cifali G, Misuri T, Rossetti P, Andrenucci M, Valentian D and Feili D 2011 Preliminary characterization test of het and rit with nitrogen and oxygen *47th AIAA/ASME/SAE/ASEE Joint Propulsion Conference & Exhibit* p 6073

[35] Tirila V G, Demairé A and Ryan C N 2023 *Acta Astronautica*

[36] Tejeda J, Potrivitu G C, Azevedo E R, Moloney R and Knoll A 2024 *Acta Astronautica* 219 542–554

[37] Rovey J L, Lyne C T, Mundahl A J, Rasmont N, Glascock M S, Wainwright M J and Berg S P 2020 *Progress in Aerospace Sciences* 118 100627

[38] Fujita K 2005 *Journal of the Japan Society for Aeronautical and Space Sciences* 52

[39] Shabshelowitz A 2013 *Study of RF Plasma Technology Applied to Air-Breathing Electric Propulsion* Dissertation University of Michigan

[40] Parodi P 2019

[41] Singh L A 2014 *A Dissertation Presented to the Academic Faculty*

[42] Ferrato E, Giannetti V, Piragino A, Andrenucci M and Andreussi T 2019 Development roadmap of sitael's ram-ep system *36th International Electric Propulsion Conference, IEPC-2019-886*

[43] Young M, Muntz E and Wang J 2001 Maintaining continuous low orbit flight by using in-situ atmospheric gases for propellant *Rarefied Gas Dynamics: 22nd International Symposium*

[44] Vallado D A 2007 *Fundamentals of Astrodynamics and Applications* (Microcosm Press)

[45] National Oceanic and Atmospheric Administration, National Aeronautics and Space Administration, United States Air Force 1976 *U.S. Standard Atmosphere, 1976*

[46] Jacchia L G 1977 Thermospheric temperature, density, and composition: New models Tech. rep. National Aeronautics and Space Administration URL https://ntrs.nasa.gov/citations/19770016704

[47] Picone J M, Hedin A E and Drob D P 2002 *JOURNAL OF GEOPHYSICAL RESEARCH* 107

[48] Cefola P, Volkov I I and Suevalov V V 2008 Description of the Russian Upper Atmosphere Density Model GOST-2004 *37th COSPAR Scientific Assembly* vol 37 p 476

[49] MathWorks 2021 atmosnrlmsise00 URL https://www.mathworks.com/help/aerotbx/ug/atmosnrlmsi

[50] Walterscheid R L 1989 *Journal of Spacecraft and Rockets* 26

[51] Binder T, Boldini P C, Romano F, Herdrich G and Fasoulas S 2016 Transmission probabilities of rarefied flows in the application of atmosphere-breathing electric propulsion *AIP Conference Proceedings* vol 1786 (AIP Publishing)

[52] Romano F, Binder T, Herdrich G, Fasoulas S and Schönherr T 2015 Air-intake design investigation for an air-breathing electric propulsion system *34th International Electric Propulsion Conference, Hyogo-Kobe, Japan*

[53] Romano F, Espinosa-Orozco J, Pfeiffer M, Herdrich G, Crisp N, Roberts P, Holmes B, Edmondson S, Haigh S, Livadiotti S, Macario-Rojas A, Oiko V, Sinpetru L, Smith K, Becedas J, Sulliotti-Linner V, Bisgaard M, Christensen S, Hanessian V, Jensen T K, Nielsen J, Chan Y A, Fasoulas S, Traub C, García-Almiñana D, Rodríguez-Donaire S, Sureda M, Kataria D, Belkouchi B, Conte A, Seminari S and Villain R 2021 *Acta Astronautica* 187

[54] Zheng P, Wu J, Zhang Y and Zhao Y 2022 *Vacuum* 195

[55] Moe M M, Wallace S D and Moe K 1995 *Geophysical Monograph Series*

[56] Crisp N, Roberts P, Livadiotti S, Macario Rojas A, Oiko V, Edmondson S, Haigh S, Holmes B, Sinpetru L, Smith K, Becedas J, Domínguez R, Sulliotti-Linner V, Christensen S, Nielsen J, Bisgaard M, Chan Y A, Fasoulas S, Herdrich G, Romano F, Traub C, García-Almiñana D, Rodríguez-Donaire S, Sureda M, Kataria D, Belkouchi B, Conte A, Seminari S and Villain R 2021 *Acta Astronautica* 180 85–99 ISSN 0094-5765 URL https://www.sciencedirect.com/science/article/pii/S0094576520307591

[57] Ferrato E, Giannetti V, Tisaev M, Lucca Fabris A, Califano F and Andreussi T 2022 *Frontiers in Physics* 10

[58] Parodi P, Quang D L and Bariselli F 2019 Study of a collector-intake system for vleo air-breathing platforms *International Conference on Flight vehicles, Aerothermodynamics and Re-entry Missions and Engineering (FAR)*

[59] Clyde Space 2020 Solar panels photon URL https://www.aac-clyde.space/wp-content/uploads/2021/11/AAC$_{D}ataSheet_{P}hoton_{o}riginal.pdf$

[60] Panton R L 2013 *Incompressible Flow* (John Wiley & Sons)

[61] Prasanth P and Kakkassery J 2006 *J. Indian Inst. Sci.* 86 169–

[62] Storch J A 2002 Aerodynamic disturbances on spacecraft in free-molecular flow Tech. rep. Aerospace Corporation El Segundo, CA URL https://apps.dtic.mil/sti/citations/ADA410696

[63] Sentman L H 1961 Free molecule flow theory and its application to the determination of aerodynamic forces Tech. rep. LOCKHEED MISSILES AND SPACE CO INC SUNNYVALE, CA URL https://apps.dtic.mil/sti/citations/AD0265409

[64] Schamberg R 1959 Analytic representation of surface interaction for free molecule flow with application to drag of various bodies Tech. rep. RAND Corporation Santa Monica, CA

[65] Pilinski M D, Argrow B M and Palo S E 2010 *Journal of Spacecraft and Rockets* 47

[66] Pardini C, Anselmo L, Moe K and Moe M M 2009 *Advances in Space Research* 45

[67] Wertz J and Larson W 1999 *Space Mission Analysis and Design* Space Technology Library (Springer Netherlands) ISBN 9780792359012

[68] Chobotov V A 2002 *Orbital Mechanics* AIAA Education Series (American Institute of Aeronautics and Astronautics) ISBN 1-56347-537-5

[69] Busek Company 2021 Hall thrusters URL https://www.busek.com/hall-thrusters

[70] National Aeronautics and Space Administration 2021 Gridded ion thrusters (next-c) URL https://www1.grc.nasa.gov/space/sep/gridded-ion-thrusters-next-c/

[71] Samples S and Wirz R 2021 *Journal of Spacecraft and Rockets* 58

[72] Ibeos 2021 Standard products URL https://www.ibeos.com/standard-products

[73] American Institute of Aeronautics and Astronautics 2015 *American National Standard Mass Properties Control for Space Systems*

[74] Berger T, Dominique M, Lucas G, Pilinski M, Ray V, Sewell R, Sutton E, Thayer J and Thiemann E 2023 *Space Weather* 21 e2022SW003330

[75] Fang T W, Kubaryk A, Goldstein D, Li Z, Fuller-Rowell T, Millward G, Singer H J, Steenburgh R, Westerman S and Babcock E 2022 *Space weather* 20 e2022SW003193

[76] Dang T, Li X, Luo B, Li R, Zhang B, Pham K, Ren D, Chen X, Lei J and Wang Y 2022 *Space weather* 20 e2022SW003152

[77] Marchioni F and Cappelli M A 2021 *Journal of Applied Physics* 130

[78] National Oceanic and Atmopsheric Administration 2023 Noaa space weather scales URL https://www.swpc.noaa.gov/noaa-scales-explanation

[79] Andreussi T, Ferrato E, Paissoni C, Kitaeva A, Giannetti V, Piragino A, Schäff S, Katsonis K, Berenguer C, Kovacova Z *et al.* 2022 *CEAS Space Journal* 14 717–740

[80] Lakhina G S and Tsurutani B T 2016 *Geoscience Letters* 3 1–11

[81] National Oceanic and Atmopsheric Administration 2023 The disturbance storm time index URL https://www.ngdc.noaa.gov/stp/geomag/dst.html

[82] Cowley S 2000 *Magnetospheric Current Systems, Geophys. Monogr. Ser* 118 91–106

[83] Oliveira D, Zesta E, Schuck P and Sutton E 2017 *Journal of Geophysical Research: Space Physics* 122 10–762

[84] Bowman B, Tobiska W K, Marcos F, Huang C, Lin C and Burke W 2008 A new empirical thermospheric density model jb2008 using new solar and geomagnetic indices *AIAA/AAS astrodynamics specialist conference and exhibit* p 6438

[85] Mathworks 2023 Spacecraft dynamics URL https://www.mathworks.com/help/aeroblks/spacecraftdy mwa_osa_a

[86] Meysam Mahooti 2023 Jacchia-bowman atmospheric density model URL https://www.mathworks.com/matlabcentral/fileexchange/56163-jacchia-bowman-atmospheric-density-model

[87] Yermolaev Y I, Zelenyi L, Kuznetsov V, Chertok I, Panasyuk M, Myagkova I, Zhitnik I, Kuzin S, Eselevich V, Bogod V *et al.* 2008 *Journal of atmospheric and solar-terrestrial physics* 70 334–341

[88] Helmholtz Centre Potsdam GFZ German Research Centre for Geosciences 2023 Geomagnetic kp index URL https://www.gfz-potsdam.de/en/section/geomagnetism/data-products-services/geomagnetic-kp-index

[89] Feldman M and Spektor R 2022 Basic analysis of an air breathing electric propulsion concept *37th International Electric Propulsion Conference, Boston, Massachusetts, IEPC-2022-446. https://www. electricrocket. org/index. php*

[90] Koppenwallner G 2011 Satellite aerodynamics and determination of thermospheric density and wind *AIP Conference Proceedings* vol 1333 (American Institute of Physics) pp 1307–1312

[91] US Dept of Commerce, NOAA, Space Environment Center 2004 Hourly averaged real-time interplanetary magnetic field values URL https://sohoftp.nascom.nasa.gov/sdb/goes/ace/monthly/200411$_a ce_m ag_1 h.txt$

[92] US Dept of Commerce, NOAA, Space Environment Center 2022 3-day geomagneit forcast URL https://www.swpc.noaa.gov/products/3-day-geomagnetic-forecast

[93] Chakraborty S and Morley S K 2020 *Journal of Space Weather and Space Climate* 10 36

[94] Wang J, Luo B, Liu S and Shi L 2023 *Frontiers in Astronomy and Space Sciences* 10 1082737

[95] Löb H W, Schartner K H, Meyer B K, Feili D, Weis S and Kirmse D 2005 Forty years of giessen ep-activities and the recent rit-microthruster development *29 th International Electric Propulsion Conference, Princeton University, Princeton, USA* vol 31

[96] Tsay M, Hohman K and Olson L 2009

[97] Rafalskyi D, Martínez J M, Habl L, Zorzoli Rossi E, Proynov P, Boré A, Baret T, Poyet A, Lafleur T, Dudin S *et al.* 2021 *Nature* 599 411–415

[98] Loeb H W and Schartner K 2004 Development of rit-microtrhusters *55 th International Astronautical Congress*

[99] Leiter H, Altmann C, Kukies R, Kuhmann J, Porst J, Berger M and Rath M 2015 Evolution of the airbus ds gmbh radio frequency ion thruster family *Proceedings of the Joint Conference of 30th ISTS, 34th IEPC and 6th NSAT, Kobe-Hyogo, Japan* pp 4–10

[100] ThrustMe 2023 The npt30-i2 URL https://www.thrustme.fr/products/npt30-i2

[101] Lieberman M A and Lichtenberg A J 2005 *Principles of plasma discharges and materials processing* (John Wiley and Sons)

[102] Polk J 2006 The effect of reactive gases on hollow cathode operation *42nd AIAA/ASME/SAE/ASEE Joint Propulsion Conference & Exhibit* p 5153

[103] Sabiston G and Wirz R E 2024 Thrust densification of space electric propulsion systems via volumetrically complex materials *AIAA SCITECH 2024 Forum*

[104] Li G Z and Wirz R E 2021 *Physical Review Letters* 126 035001

[105] Godyak V, Piejak R and Alexandrovich B 1999 *Journal of applied physics* 85 703–712

[106] Godyak V and Alexandrovich B 2017 *Review of Scientific Instruments* 88

[107] Suzuki K, Konishi K, Nakamura K and Sugai H 2000 *Plasma Sources Science and Technology* 9 199

[108] Kortshagen U, Gibson N and Lawler J 1996 *Journal of Physics D: Applied Physics* 29 1224

[109] Caspers F 2012 *arXiv preprint arXiv:1201.4068*

[110] Fritz Dellsperger 2023 Smith v4.1 URL https://www.fritz.dellsperger.net/smith.html

[111] Mathworks 2023 Matching network designer URL https://www.mathworks.com/help/rf/ref/matchingnetworkdesigner-app.html

[112] Çankaya University 2023 The complex reflection coefficient URL https://ece358.cankaya.edu.tr/uploads/files/Ece358Exp5.pdf

[113] Mathworks 2023 gamma2z URL https://www.mathworks.com/help/rf/ref/gamma2z.html

[114] Meziani T, Colpo P and Rossi F 2006 *Journal of applied physics* 99

[115] Godyak V and Chung C W 2006 *Japanese journal of applied physics* 45 8035

[116] McLyman C W T 2004 *Transformer and inductor design handbook* (CRC press)

[117] Occupational Safety and Health Administration 2023 Radiofrequency and microwave radiation URL https://www.osha.gov/radiofrequency-and-microwave-radiation/standards

[118] Federal Communications Commission 2023 Section 1.1310 - radiofrequency radiation exposure limits. URL https://www.govinfo.gov/content/pkg/CFR-2011-title47-vol1/xml/CFR-2011-title47-vol1-sec1-1310.xml

[119] American Radio Relay League 2023 Section 1.1310 - rf exposure URL https://www.arrl.org/rf-exposure

[120] PATTERSON M and WILLIAMS JR G 1992 Krypton ion thruster performance *28th Joint Propulsion Conference and Exhibit* p 3144

[121] Scholze F, Pietag F, Adirim H, Kreil M, Kron M, Woyciechowski R, Bundesmann C and Spemann D 2022 *Journal of Electric Propulsion* 1 28

[122] Esteves B, Drag C, Bourdon A and Alvarez-Laguna A 2022 Experimental and numerical investigation of a gridded ion thruster running with different propellants (i2, xe, kr, ar) *International Electric Propulsion Conference, Massachusetts Institute o f Technology, Cambridge, MA, USA* p 416

[123] Samples S A and Wirz R E 2020 *Plasma Research Express* 2 025008

[124] Tsay M M T 2006 *Numerical modelling of a radio-frequency micro ion thruster* Ph.D. thesis Massachusetts Institute of Technology

[125] Patterson M J and Mohajeri K 1991 Neutralizer optimization *International Electric Propulsion Conference* NAS 1.15: 105578

[126] Clausing P 1932 *Annalen der Physik* 404 961–989

[127] Cole R 1977 *IMA Journal of Applied Mathematics* 20 107–115

[128] SpaceX 2023 Argon hall thruster tech specs URL https://x.com/SpaceX/status/1629948869239873538?lang=en

[129] Lopez-Uricoechea J, Lev D and Walker M L 2022 *Journal of Electric Propulsion* 1 11

[130] Crandall P, Piccone V, Asanuma T and Wirz R 2024 Geomagnetic storm risks to air-breathing electric propulsion missions pp 1–7

[131] Tejeda J and Knoll A 2023 *Acta Astronautica* 203 268–279

[132] Tisaev M, Karadag B, Ferrato E, Andreussi T and Fabris A L 2024 *Acta Astronautica* 214 722–736

[133] Wang J, Polk J, Brophy J and Katz I 2001 Three-dimensional particle simulations of nstar ion optics *27th International Electric Propulsion Conference, Pasadena, CA*

[134] Ko Y, Kim S, Moon G, Yi M, Park K, Kim Y and Jun E 2023 *Acta Astronautica* 212 198–212

[135] Godyak V 2013 *Journal of Physics D: Applied Physics* 46 283001

[136] Godyak V 2011 *Plasma Sources Science and Technology* 20 025004

[137] Kolobov V I and Godyak V A 2017 *Plasma Sources Science and Technology* 26 075013

[138] Kraus W, Briefi S, Fantz U, Gutmann P and Doerfler J 2014 *Review of Scientific Instruments* 85

[139] Felsteiner J, Slutsker Y Z and Vaisberg P 2005 *Journal of applied physics* 98

[140] Sukhinin G, Isupov M, Fedoseev A and Yudin I 2019 Development of a distributed ferromagnetic enhanced inductively coupled plasma source for plasma processing *Journal of Physics: Conference Series* vol 1243 (IOP Publishing) p 012004

[141] Aanesland A, Rafalskyi D, Bredin J, Grondein P, Oudini N, Chabert P, Levko D, Garrigues L and Hagelaar G 2014 *IEEE Transactions on Plasma Science* 43 321–326

[142] Schloeder N R, Liu T, Walker M L, Polzin K A, Dankanich J and Aanesland A 2014 Design and preliminary testing plan of electronegative ion thruster *50th AIAA/ASME/SAE/ASEE Joint Propulsion Conference* p 3425

[143] Godyak V, Raitses Y and Fisch N J 2007 Rf plasma cathode-neutralizer for space applications *30th International Electric Propulsion Conference, Florence, Italy*

[144] Lloyd S, Shaw D M, Watanabe M and Collins G J 1999 *Japanese journal of applied physics* 38 4275

[145] Dixon L H 2001 *Magnetics design handbook* (Unitrode Products from Texas Instruments)

[146] Thorsteinsson E and Gudmundsson J T 2009 *Plasma Sources Science and Technology* 18 045001

[147] Ashida S, Lee C and Lieberman M 1995 *Journal of Vacuum Science & Technology A: Vacuum, Surfaces, and Films* 13 2498–2507

[148] Chabert P, Arancibia Monreal J, Bredin J, Popelier L and Aanesland A 2012 *Physics of Plasmas* 19

[149] Gudmundsson J T 2005

[150] Farnell C C, Williams J D, Wilbur P J *et al.* 2007

[151] Baalrud S, Hegna C and Callen J 2009 *Physical review letters* 103 205002

[152] Riemann K U 1995 *IEEE Transactions on plasma science* 23 709–716

[153] Hatami M and Kourakis I 2022 *Scientific Reports* 12 6905

[154] Mathworks 2024 ode45 URL https://www.mathworks.com/help/matlab/ref/ode45.html